MATERIALS BY "DESIGN": RATIONAL DISCOVERY OF NEW TERNARY CHALCOGENIDES AND THEIR ELECTRONIC BEHAVIOR

by
BENJAMIN ALLEN TRUMP

A dissertation submitted to Johns Hopkins University in conformity with the requirements for the degree of Doctor of Philosophy

Baltimore, Maryland

June, 2016

Abstract

From the bronze age to the silicon age, the discovery of new materials has driven the technology of the future. Historically the discovery of new materials is an investigative process rather than a predictive one. Utilizing homologous series to guide the investigative process allows for rational designs to predict specific structures with desired properties. However, the desired products are not always achieved, and additional experiments are conducted to isolate new compounds and determine their properties. This exact process has led to the discovery of over four new compounds contained in this dissertation, as well as verified existing understanding of similar compounds.

Chapter 1 contains introductory topics to understand the enclosed works and the experimental tools utilized. Chapter 2 discusses the synthesis and physical properties of the new misfit compound $(BiSe)_{1.15}(TiSe_2)_2$, discovered using the homologous series $(MX)_{m(1+\delta)}(TX_2)_n$. Intercalation with copper, $Cu_x(BiSe)_{1.15}(TiSe_2)_2$, $(0 \leq x \leq 0.10)$ is also reported, but unlike Cu_xTiSe_2, no superconductivity is observed down to $T = 0.05$ K, though this effective approach elucidates the impact of dimensionality on charge density wave formation and superconductivity.

Chapters 3 and 4 are the result of expanding the homologous series $(MX)_{m(1+\delta)}(TX_2)_n$ to include iridium, of interest due to strong spin-orbit coupling.

Though no misfit compounds were observed, three Ir-Sn-Se compounds and an Ir-Pb-Se compound were observed. Chapter 3 describes the synthesis and physical properties of $IrSn_{0.45}Se_{1.55}$, a pyrite phase, $Ir_2Sn_3Se_3$, a skutterudite phase, and Ir_2SnSe_5, which is layered, distorted β-MnO_2 (pyrolusite) structure. All three compounds display varying degrees of anion-anion bonding and electronic structure calculations on $Ir_2Sn_3Se_3$ suggest that it is topologically non-trivial under tensile strain, due to inversion of Ir-*d* and Se-*p* states.

Chapter 4 describes the synthesis and physical properties of the distorted-Hollandite $PbIr_4Se_8$. Characterization measurements demonstrate disorder on the Pb site, due to the combination of lone-pair effects and the large size of the one-dimensional channels. Comparisons are made to known Hollandite and pseudo-Hollandite structures, which demonstrates that the anion-anion bonding in $PbIr_4Se_8$ distorts its structure, to accommodate the Ir^{3+} state.

Dissertation committee

Advisor *- Professor Tyrel M. McQueen*

Professor Kit H. Bowen

Professor Rebekka Klausen

Acknowledgements

Without the support and guidance of many individuals the following work would not be possible. First and foremost, the tutelage of Prof. Tyrel M. McQueen has been invaluable. His passion for the sciences and knowledge base is truly inspiring, and is only surpassed by his genuine interest in the wellbeing of his students. I could not have asked for a better advisor to introduce me to the world of solid state chemistry and the rigors of graduate school. I would also particularly like to acknowledge Prof. Jamie Neilson, whose patience, mentoring, and advice was essential in developing the foundation of my graduate experience and understanding.

I extend my gratitude to my various graduate committee members, Profs. Kit Bowen, Rebekka Klausen, Jerry Meyer, Todd Hufnagel, and Nina Markovic, for their help and advice over the years. I would also like to thank my various professors throughout the years, particularly Profs. Harris Silverstone, Art Bragg, Douglas Poland, Peter Armitage, and David Yarkony, whose engaging lectures and demanding coursework laid the foundation for my graduate studies. In addition, I would be amiss if I did not acknowledge the unwavering support of the staff of the departments of Chemistry and Physics and Astronomy, especially Boris Steinberg, Brian Shriver, Rosalie Elder, Jean Goodwin, Dave Brewster, Joe Russel, Olga Shchepina, John Kidwell, Wanda Carter, and Thomas Rhatigan.

I would also like to thank the members of the Institute for Quantum Matter, especially Prof. Collin Broholm, Dr. Seyed Koohpayeh, Dr. Natalia Drichko, Guy G. Marcus, Wes Fuhrman, Allen Scheie, Shan Wu, Dr. Kemp Plumb, Dr. Jonas Kindervater,

Dr. Jiajia Wen, Dr. Sunxiang Huang, Nicholas Laurita, Dr. J.T. Mlack, and Dr. Tyler Morgan-Wall. Without their help and patience for a simple chemist I surely would have taken several more years to graduate and would only have half the knowledge I do today.

Special thanks is due to all of the members of the McQueen Lab, for the patience of postdocs Dr. Adam Phelan and Dr. Ally Fry despite my incessant inquiries, and for the camaraderie and support of Dr. John Sheckelton, Dr. Patrick Cottingham, Dr. David Wallace, Kathryn Arpino, Zachary Kelly, Jake Tutmaher, Jessica Panella, Jennifer Morey, and many talented undergraduates. I was fortunate to have such a passionate and intellectually stimulating group of individuals to enhance my graduate experience. I wish you all the best of luck in your future endeavors.

Last but not least, I would like to thank the support of my friends and family. Without the support of Evan Collins and Sara Marquez I surely would not have stayed sane throughout my graduate career. Thanks to Jonathan Trump and Lindsay Butler for their advice from their experiences as well. Lastly, a special thanks to Jack and Sally Trump, and to Jackie, for their unshakable love and encouragement, and for putting up with me for all these years despite myself.

Table of Contents

List of Figures

List of Tables

1. Introduction

Throughout history, the advent of new technologies often accompanies the advent of new materials. The role of new materials has varied from alloying techniques, such as bronze or steel, to the discovery of novel physical phenomena, such as superconductivity - leading to cellular communications, more efficient generators, and MRIs. Paradoxically, these discoveries are often unexpected, such as the discovery of superconductivity or fiberoptic cables. This means that the emergence of new materials is a discovery driven process, rather than a predictive one, though rational investigation and optimization is also integral.

The discovery process begins by targeting a material based off of desired properties, systematically attempting to synthesize the material, characterizing it for both properties and structure, and finally figuring how to correct the experiment to achieve the desired product. This does not mean that the targeted material is always made, it is equally likely that an alternative new material is obtained, which must then be fully characterized to determine its usefulness. Figure 1.1 demonstrates the feedback loop for designing experiments to create new materials with desired properties. Following this loop involves the fields of physical chemistry, condensed matter physics, material science, and crystallography. The interplay between all of these fields is what gives birth to solid state chemistry, which is the focus of this dissertation.

My research focuses specifically on the processes on the right in Figure 1.1, from identifying and attempting to target new materials, to characterizing them (both structure and physical properties), understanding their properties, and designing new targets to either make the materials more pure, or to enhance certain properties. However, before delving fully into several case studies, we will first introduce several topics. For more information there are many excellent textbooks that go into much greater detail.[1-6]

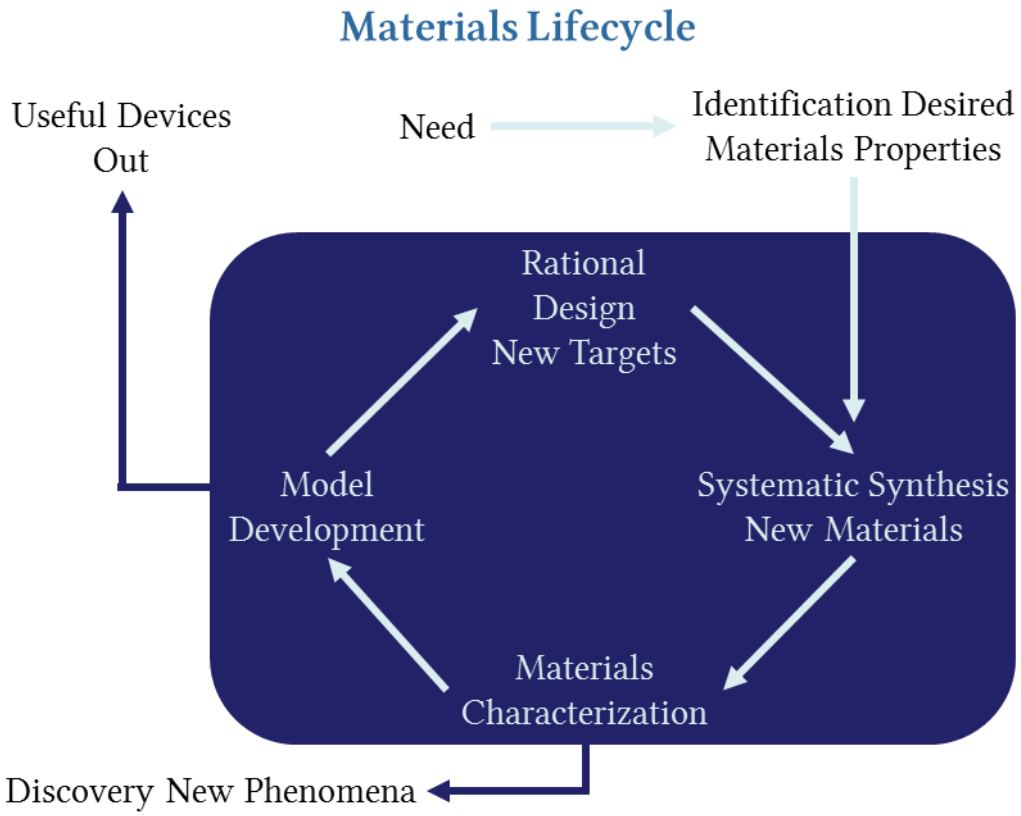

Figure 1.1: Feedback look for the discovery of new materials, courtesy of T.M.M.[7]

1.1 Background

1.1.1 Homologous Series and Predictive Experiments

The first step in the materials lifecycle is identifying the desired material properties and then designing an experiment to create a material with those properties. In order to predict both the desired properties and structure, homologous series are used. Homologous series contains the same structural units even with varied atom types or varied atomic ratios. An example is the misfit series $(MX)_{m(1+\delta)}(TX_2)_n$ (M = Sb, Bi, Pb, Sn; X = S; Se; T = Ti, V, Cr, Ta, Nb, and m and n are integers). Here the MX layer is a rock-salt type layer where the TX_2 layer consists of edge-sharing polyhedra. These compounds are known as misfits because the lattice parameters, or dimensions, of each layer type are incommensurate with one another. This mis-match is represented by the δ parameter.

Changing the atomic ratios (i.e. changing m and n) leads to various ratios of each layer type, demonstrated by Figure 1.2. Changing the types of elements also allows for different properties to be predicted. For instance, compounds with $NbSe_2$ or $TaSe_2$ are known to superconduct., and compounds with VX_2 layers commonly have charge density wave behavior. More information on how alternate elements can affect the properties of these series can be found in an excellent review by Wiegers.[8] Alternatively, materials which contain heavy atoms, such as Bi or Pb could host exotic quantum behavior, as explained later.

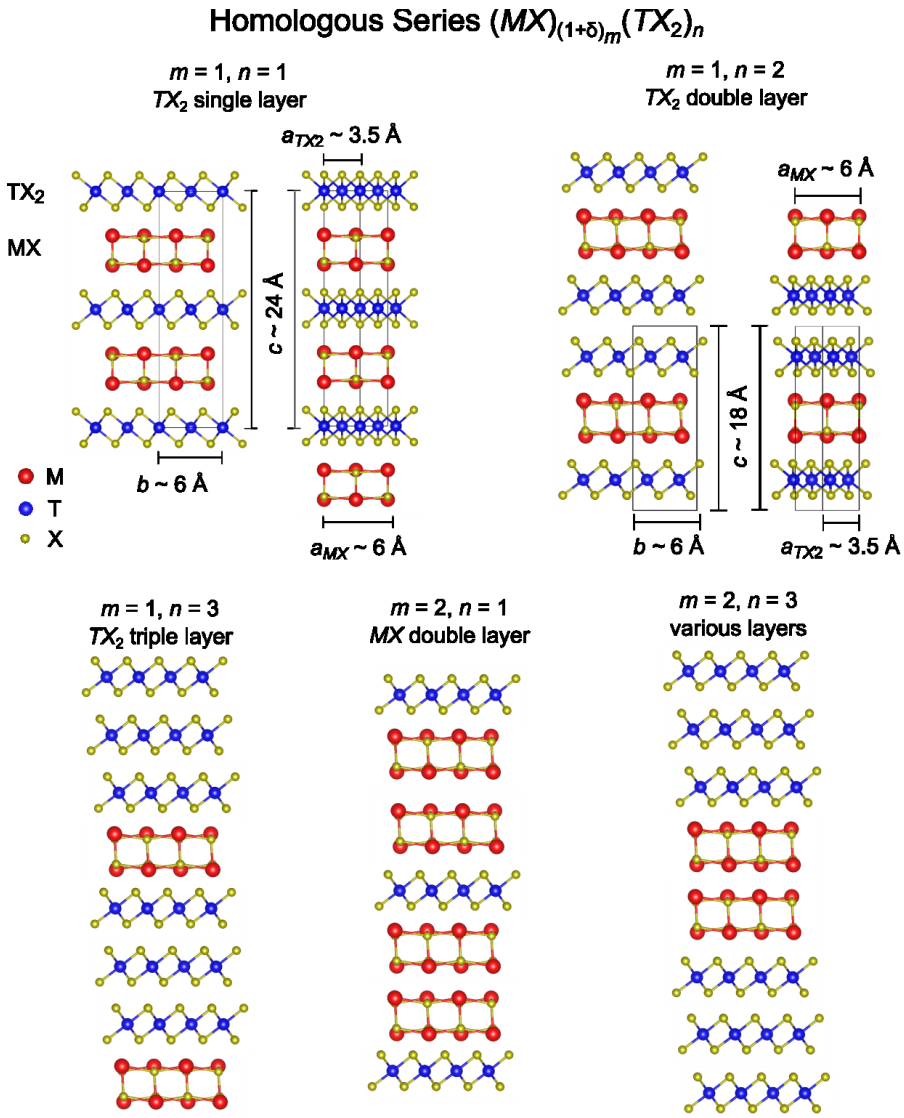

Figure 1.2: An example homologous series (MX)(1+δ)m(TX2)n, with several structures for various m and n values. The top row demonstrates the origin of the δ parameter as the a lattice parameters between the MX and TX2 layers does not match. The bottom row demonstrates several alternate m:n ratios which lead to various amount of MX and TX2 layers respectively.

The work presented herein expands this homologous series, using elements outside the typical range, but based off of similar structure types. The first work used the misfit compounds $Cu_x(BiSe)_{1+\delta}(TiSe_2)_n$ (n = 1, 2) with various concentrations of x, in order to tune the properties of these compounds. The other two works attempted to expand this series to include Ir, as the $IrTe_2$

structure is analogous to $TiSe_2$. Though homologous series offer a promising route for the design of materials to predict both properties and structures of new materials, but this is merely the first step in this process. Once initial experiments are conducted, the resulting materials must be characterized (structurally and properties) to see if the predictions were met, and then further experiments can be conducted. Before we can explain these other steps, we must first explain why solid materials, especially with heavier atoms, make for useful materials.

1.1.2 Quantum Mechanical Considerations

Our knowledge of materials (and paradoxically, lack of knowledge) and their properties has especially increased over the course of the last hundred years, with the discovering of quantum mechanics. This discovery has provided profound insight into understanding the most microscopic identities, namely electrons. Solutions to quantum mechanical problems can be found for simple systems with a single electron, or a single valence electron. Real materials are much more complex, where nucleus-nucleus interactions and electron-electron interactions must be considered. This is modeled using Eq. (1):[4]

$$\widehat{H} = -\sum_i \frac{p_i^2}{2m_e} + \sum_{i,j} \frac{e^2}{|r_i - r_j|} - \sum_n \frac{p_n^2}{2m_n} + \sum_{m,n} \frac{Z_m Z_n e^2}{|R_m - R_n|} - \sum_{m,i} \frac{Z_m e^2}{|R_m - r_i|} \qquad (1)$$

Eq. (1) shows the Hamiltonian for every fundamental interaction in a solid, as the terms model the electron kinetic energy, electron-electron repulsion, nucleus kinetic energy, nucleus-nucleus repulsion, and nucleus-electron

attraction respectively.[4] Here p is momentum, m_e is the mass of an electron, m_n is the mass of a neutron, R and r are the radial distance from the origin of each neutron and electron species, and Z is the atomic number. This Hamiltonian seeks to describe then energy of a system, through the Schrodinger equation, $\hat{H}\psi = E\psi$, with a wavefunction ψ. Using a hyrodgen atom (one electron, one proton nucleus), a series of wavefunction solutions, or orbitals can be derived, shown in Figure 1.3.[4] It is important to note that these are for a one electron system, for systems with many electrons, these hybridize leading to more non-trivial orbital shapes. Here we will also introduce the idea of parity, which describes the ability of an orbital to overlap with itself when the parity operator is applied (x, y, z -> -x, -y, -z).[4] If the orbital is unchanged under this symmetry operation then is classified as even, while if the location of the positive and negative (red and blue) lobes swap then it is classified as odd. Figure 1.3 demonstrates that *s* and *d* orbitals have even parity while the *p* orbitals have odd parity.

Accounting for all of the interactions in Eq. (1) leads to no direct analytical solution, hence most models which accurately describe systems need to involve the use of approximations, making electron-electron and neutron-neutron repulsion negligible. The types of assumptions tend to only describe loosely packed, light atoms, with few electrons, such as gases or most liquids.

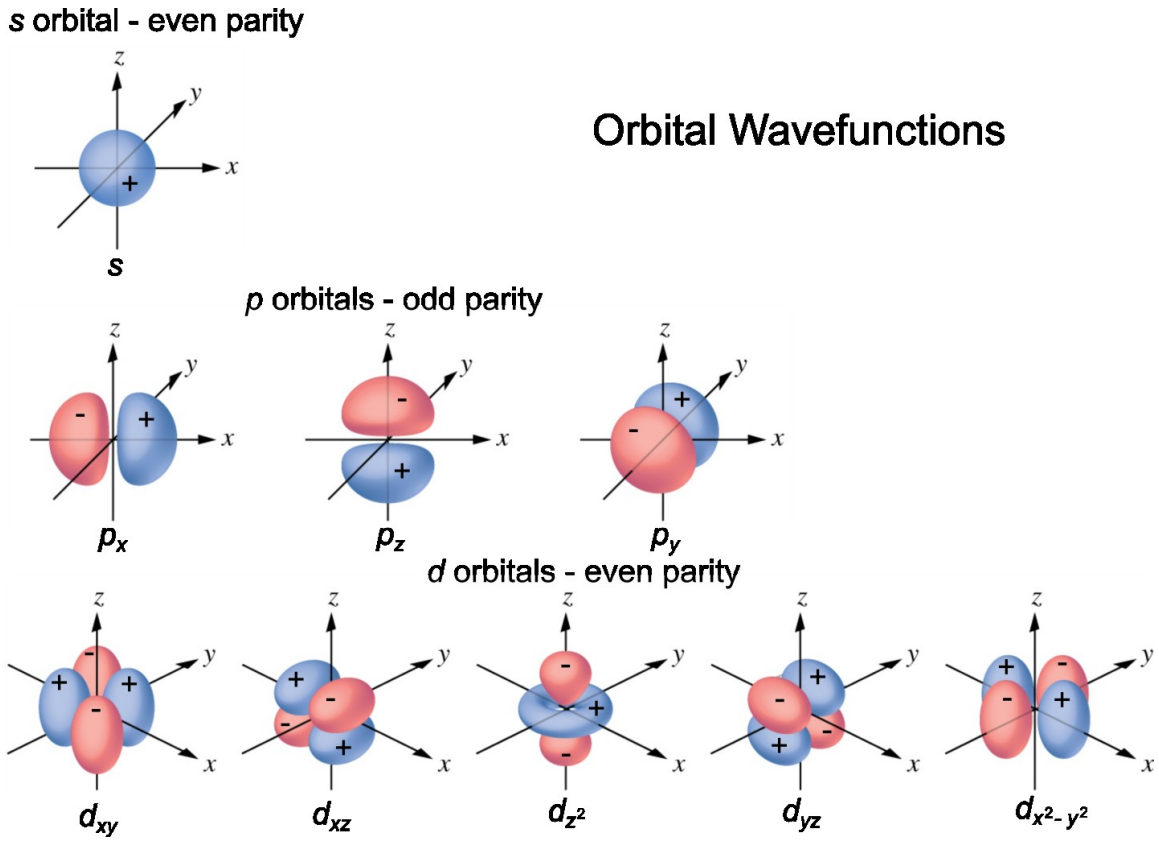

Figure 1.3: Orbital solutions for the hydrogen atom, shaded blue and red for positive and negative areas respectively. Note that the s and d orbitals have even parity, meaning they are unchanged when applying the parity operator (x, y, z -> -x, -y, -z), while the p orbital is not, hence it has odd parity.

The field of solid state chemistry deals with a similar amount of atoms, but in a volume a fraction of the size. This makes interactions, particularly electron-electron interactions, very strong in solid materials, and these interactions are no longer negligible. It is in these strongly interacting systems that novel phenomena, such as phonons, or the celebrated superconductivity arise. Anderson explained this emergence in his seminal paper entitle "More is Different".[9] The expectation is that understanding the most fundamental microstructure of a system results in a complete understanding of the

macrostructure. For tightly packed, strongly correlated electron systems, this is not the case. Instead it is seen that "more" leads to "different", novel behavior. This is similar to a group of animals, from a herd of gazelle, a school of fish, or a gaggle of geese; the group leads to new patterns and behavior where the results are greater than the sum of the individuals.

1.1.3 Band Theory

Describing the molecular orbitals of a system which is composed of many atoms (~10^{23}) is different than describing a system with only a few atoms. Molecular orbital theory is constructed for systems which only contain two or only a few atoms, giving rise to bonding and anti-bonding orbitals. Figure 1.4 demonstrates that including more atoms leads to many discrete energy levels over a small area. The collection of discrete energy levels can also be described by a band of continuous energy levels. This description is much more convenient, as systems with ~10^{23} atoms require drawing more orbitals than is reasonable. The density of states (DOS) can also be achieved by integrating over the band, noting that the Fermi level (denoted by the Fermi energy, E_f), also called the chemical potential, represents the highest occupied state.

Figure 1.4 only describes a single band and only for a single orbital. As more orbitals are introduced, the system has more bands. Each band can also be described as a function of anti-bonding character, shown in Figure 1.5, which displays a one-dimensional chain of atoms, with two limits - fully bonding and

fully anti-bonding, with a discrete amount of anti-bonding/bonding character in-between. For the fully anti-bonding case $k = \pi/a$, where a is the interatomic spacing, and $k = 0$ for the fully bonding case, with the energy of the band changing as a function of k. Finally, a similar DOS image is shown as for Figure 1.4, however the DOS has the correct shape after integrating over the band.

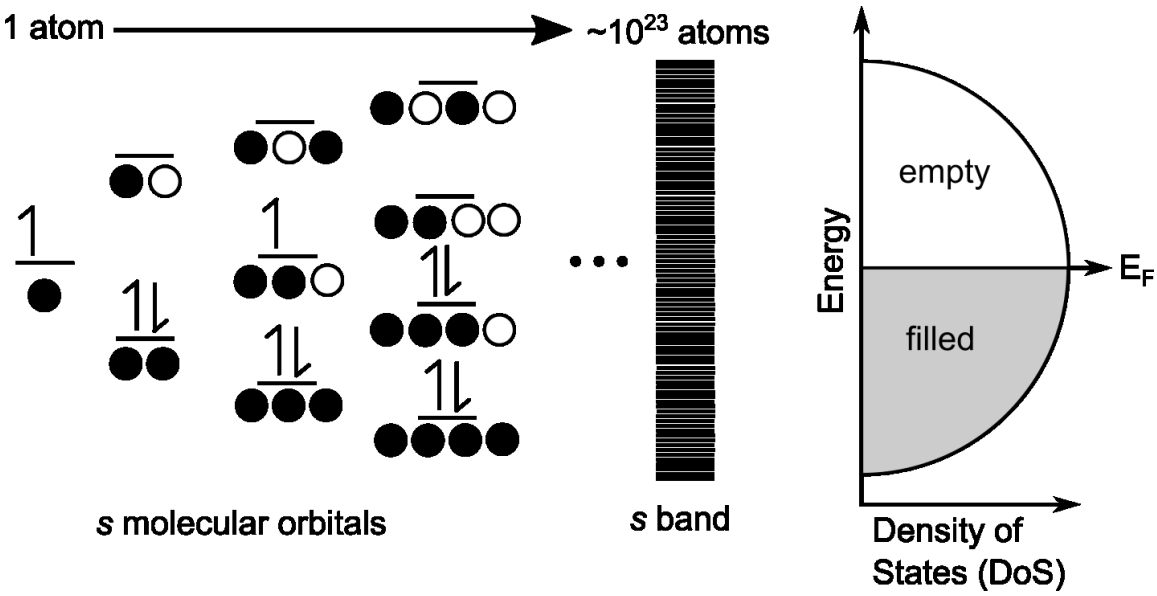

Figure 1.4: As more atoms are in a system, more discrete energy levels are needed to describe the bonding and antibonding orbitals. Solids contain ~10^{23} atoms, which are instead described as a continuum of discrete energy levels, known as a band. The DoS describes the density of these discrete energy levels as a function of energy, with the band filled up to the Fermi level, designated as E_F.

The electronic band structure of a material is incredibly important, and can give insight into exotic behavior in a system. Understanding how bands change as a function of k can indicate the type of bands they are, and hence their parity as well. The above example also only presents a one-dimensional case, and in reality band structures must describe a three dimensional system instead, with various labels to represent π/a points in different directions.

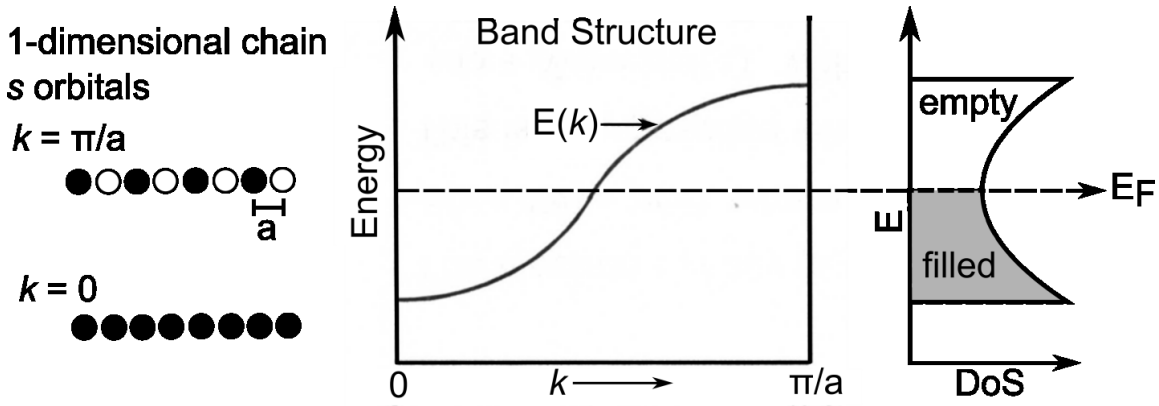

Figure 1.5: A 1-dimensional chain of *s* orbitals, with the extremes of fully bonding ($k = 0$) and fully antibonding ($k = \pi/a$) shown. A continuum of k, crystal momenta, is displayed in the band structure, with the energy given as a function of k. Finally the density of states (DoS) is also shown, where the amount of states is given be the slope of the band structure, giving the DoS a distinct shape.

1.1.4 Superconductivity

The most common and well known exotic behavior that arises in materials due to non-negligible electron-electron interactions is superconductivity. This phenomena is described by a drop from a finite value to zero resistance in a material as a function of temperature. This was first observed upon cooling Hg to 4.19 K, when Onnes and Clay were investigating the reduction of resistance at lower temperatures.[10] To their surprise the resistance dropped much more significantly than expected upon cooling from 4.2 to 4.19 K, and this discovery led to a Nobel prize, decades worth of theoretical work, and countless technological breakthroughs.

The theoretical description, pioneered by Barden, Cooper, and Schrieffer, explains superconductivity as two electrons pairing into "Cooper pairs", with their pairing mediated by phonons (cooperative vibrations through solid

materials).[11] This origin of this description arises from considering these Cooper pairs to be a new ground state in the material, due to strong electron-electron interactions.

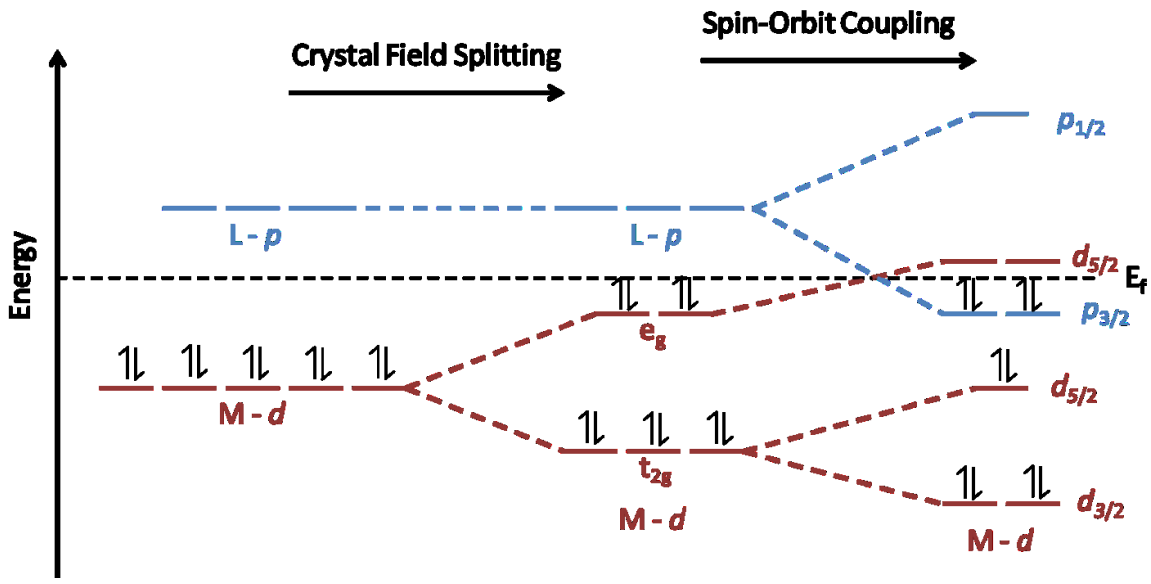

Figure 1.6: Diagram of how spin-orbit coupling (SOC), along with other effects and cause non-trivial orbital behavior around the Fermi level. Here M represents an octahedral bound transition metal center with L anions. The combination of crystal field splitting and SOC leads to an inversion of orbital parity around the Fermi level, where *p* has odd parity and *d* has even parity.

1.1.5 Spin-Orbit Coupling

Another type of interaction in solids, which causes non-trivial phenomena, is spin-orbit coupling (SOC). For lighter, smaller atoms the spin and orbital angular momenta can be assumed to be independent of each other. As atoms become larger, their nuclear charge increases, as well as their electron's orbital velocity. The increase in orbital velocity gives rise to a significant magnetic field which interacts with its spin, and splits orbital energy levels according to the spin of their electrons. Figure 1.6 demonstrates how SOC can split and energetically

reorder atomic orbitals. When combined with other strong effects, such as crystal field splitting, this can cause non-trivial orbital splitting, causing orbitals of opposite symmetry to overlap and re-order, as shown in Figure 1.6.

1.1.6 Topological Insulators

It is this type of strong behavior which leads to topological insulating behavior. Topological insulators are materials which are insulating in the bulk, yet contain electronic states on the surface. This effect arises from swapping the symmetry of wavefunctions around the Fermi level. Due to this inversion of symmetry, when a topological insulator is in contact with a normal insulator (with opposite parity), states with similar symmetry are connected in order to preserve orbital momentum, as shown in Figure 1.7. The connection of these states, with the inversion of orbital parity in a topological insulator. leads to electronic states at the interface between trivial and topological insulators. More notably, the electrons on the surface of topological insulators are spin-momentum locked, meaning they can only travel certain directions based off of their spin. This eliminates backscattering due to defects in a material, and makes this surface a better conductor than most metals, at room temperature, unlike superconductors which require extremely low temperatures in order to conduct electrons with no resistance. This makes topological insulators extremely useful for practical applications.

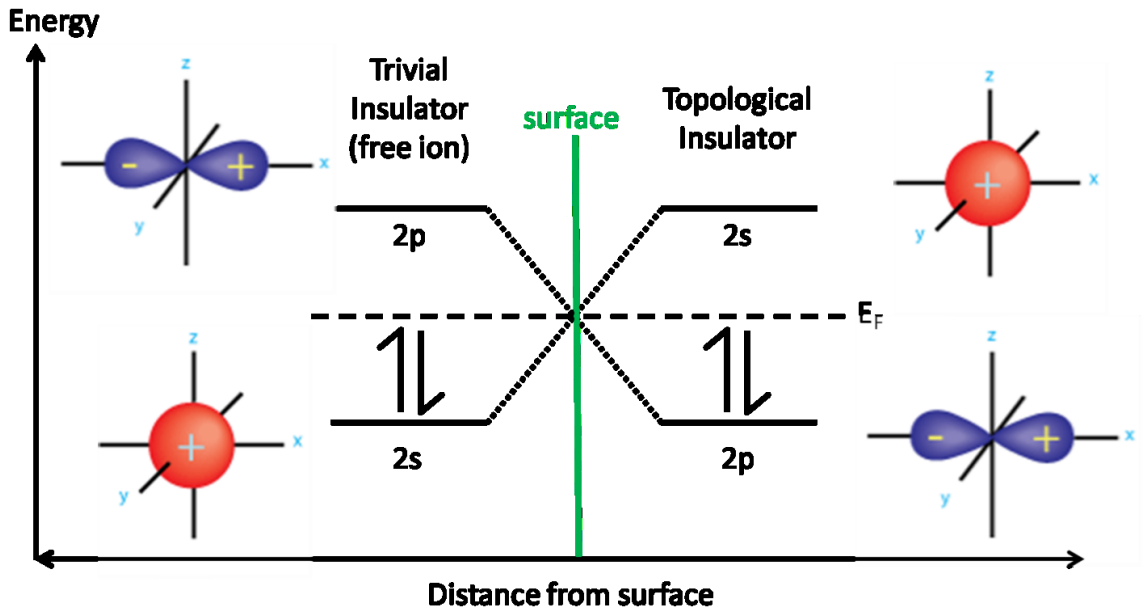

Figure 1.7: A topological insulator has an inversion of parity around the Fermi level (E_F) due to strong spin-orbit coupling. When in contact with a substance with normal parity, in order to preserve orbital momentum, states with similar parity are connected, leading to conductive states at the surface of a topological insulator, but none in the bulk topological insulator.

1.1.7 Synthesis

In solid state chemistry typical synthesis methods involve heating materials to elevated temperatures in order to get them to react. This is important as it allows for reactions to overcome large energy barriers. To better understand, consider the Gibbs free energy equation:

$$\Delta G = \Delta H - T\Delta S \tag{2}$$

where ΔH is the change in enthalpy (internal energy), ΔS is the change in entropy (disorder), and ΔG is the Gibbs free energy. For a particular set of reactants, a reaction is thought to be spontaneous when ΔG is negative - and when the reaction pathway creates the largest negative value of ΔG possible, then the

product is the thermodynamic product. The most important variable however is the activation energy (E_a) between the reactants and products, as shown in Figure 1.8. Just because ΔG is negative does not mean that a reaction is spontaneous, as there may be a large activation barrier that must be overcome.

Standard solid-state synthesis reactions typically begin with stoichiometric mixtures of elements, and though the desired products may be more energetically stable, considerable energy must be put in to get them to react. To get the element to mix at the atomic level, namely diffuse, they must either be in a liquid or gas phase to react, and mechanical mixing is often required as well. Hence temperatures anywhere from 100-1500 °C, or even higher, are required for reactions, depending on the materials. Intermittent grindings are also required in order to overcome lack of diffusion for solids as well. In fact, it is energetically more favorable to defects (such as lack of diffusion) to occur, due to the Gibbs free energy equation, as shown in Figure 1.9. As more defects are incorporated, the entropy becomes larger, and the change in free energy becomes more negative, giving rise to a minimum in the free energy that contains some number of defects. Hence, considerable energy must be put into a system to make sure that it is entirely defect free.

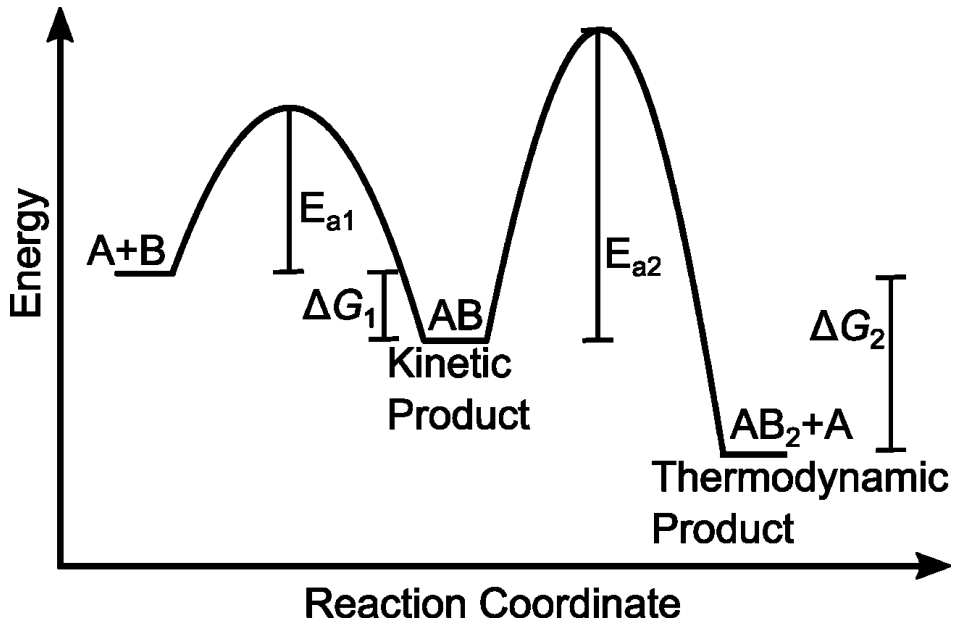

Figure 1.8: A typical solid state reaction may contain multiple transitions, where both kinetic and thermodynamic product exist. If a reaction is done closer to room temperature it may achieve the kinetic product AB, as this is thermodynamically favorable ($\Delta G < 0$) and has a small activation energy (E_{a1}). Solid state reactions are typically done at very high temperatures, which overcome even higher energy barriers (E_{a2}), leading to a thermodynamic product, which is the most thermodynamically stable product with the most negative ΔG.

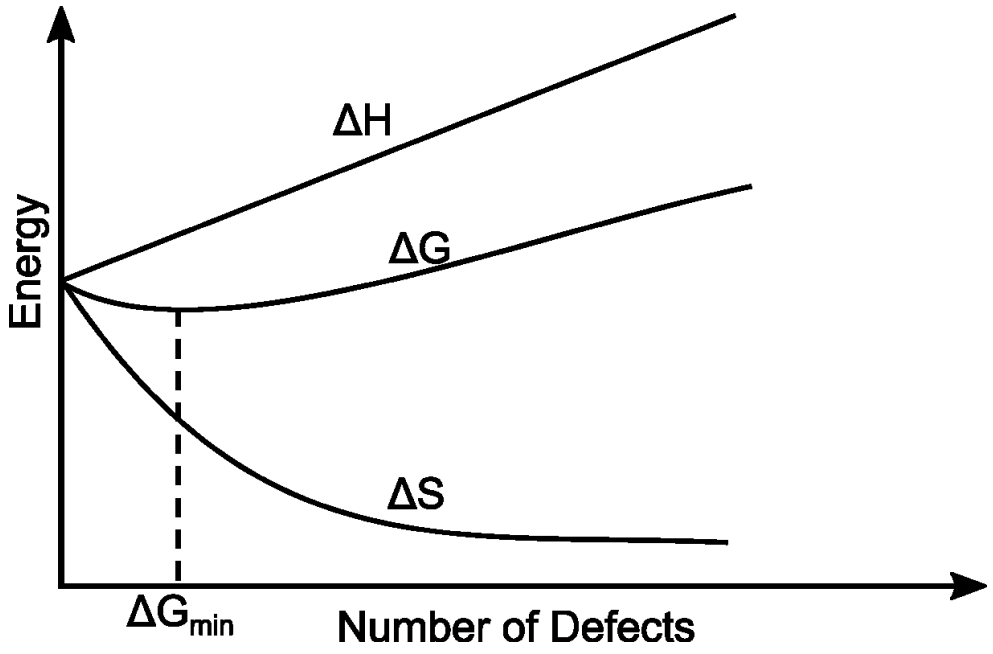

Figure 1.9: Due to the combined effects of enthalpy (ΔH) and entropy (ΔS) it is more energetically favorable for some number of defects to occur due to a minimum of the Gibbs free energy (ΔG) occurring at a non-zero value.

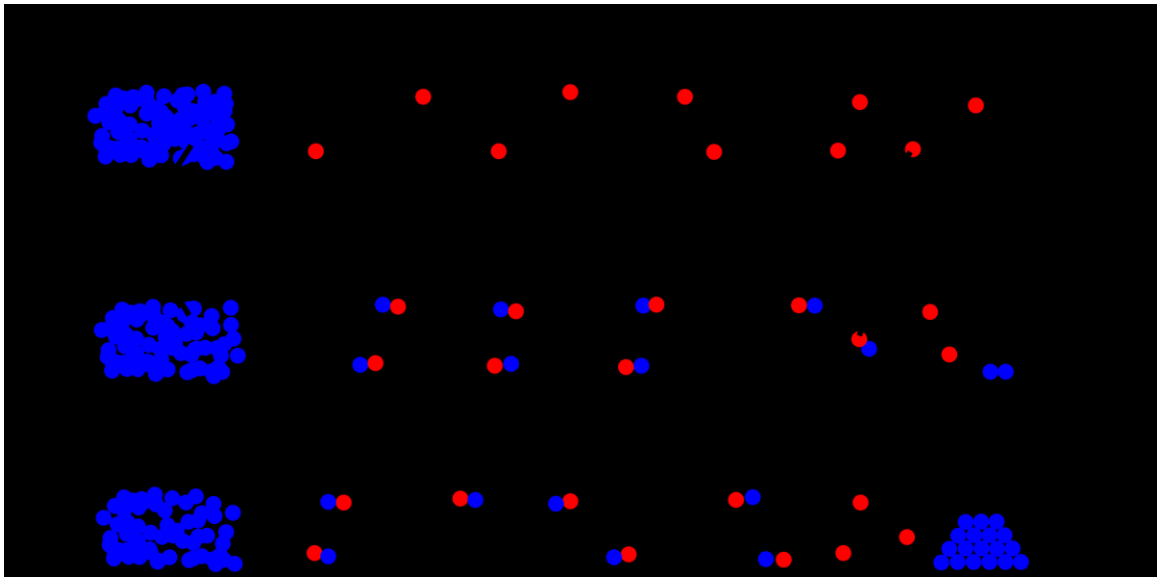

Figure 1.10: Schematic for chemical vapor transport reactions. a) First the tube is heated and a temperature gradient is introduced. This decomposes the transport agent (here NH_4Cl) into a gas phase. b) The gas phase transport agent begins to transport the powder material, as it goes into "solution" (sol.). c) Powder slowly comes out of the gas phase on the cold end of the tube, in a well ordered (crystalline) structure.

Typical standard solid state synthesis also involves sealing elements under vacuum (or a specific atmosphere) in a quartz tube, to avoid reactions with air. Alternatively, a transport agent can also be added, along with a temperature gradient. A transport agent is a material which decomposes into a gas phase at higher temperatures, such as $TeCl_4$, which decomposes into Te and $2Cl_2$ gas. This gas phase helps the diffusion process, as elements go into "solution" on the hot side, and come out of "solution" on the cold end. The exact process for materials to go into "solution" in the gas phase is often complicated and not well understand. The result however, is that as the powder is slowly

transported, it becomes crystalline on the other side of the tube (shown in Figure 1.10). Despite using a gas phase to combat diffusion, these materials are also not defect free, and often contain defects (such as the inclusion of the transport agent into the crystal) similar to standard solid state synthesis techniques.

1.1.8 Crystallography

Once materials are reacted, one must see what phases exist. In order to identify atomic structure non-ionizing radiation is used, particularly X-rays or neutrons. X-rays scatter off of the electron cloud, while neutrons scatter off of the nucleus. Theoretically this means that the form factor describes X-ray scattering, while the scattering cross section describes neutron scattering. The form factor is based off of the amount of electrons for an atom (Z), hence heavier atoms scatter more strongly than lighter ones. This also means that it is often hard to see light atoms when heavier atoms are present when using X-rays. Alternatively, the scattering cross section for neutrons does not follow a specific trend - hence lighter and heavier atoms are both seen when using neutron diffraction.

The particular diffraction pattern of a material depends upon the structure of a material, namely the unit cell and atomic positions. Neutrons and X-rays are useful because they interact on the same length scale of ordered solids and because they have wave-like properties, namely they constructively or deconstructively interfere with each other. The diffraction pattern also depends

upon the incident vector of radiation, as shown in Figure 1.11, described by Bragg's law:

$$n\lambda = 2d \sin\theta \tag{3}$$

where n is any integer, λ is the incident wavelength, d is the spacing between planes, and θ is the scattering angle. Figure 1.11 displays that incident radiation constructively interferes when $n\lambda/2$ is equal to the spacing between planes, which only occurs at certain angles. This leads to peaks, or reflections, at certain angles, only when these conditions are met. Since X-rays scatter off of electron clouds, the form factor also dies off at higher angles, while the peak intensity for neutrons remains constant at higher angles. To observe many reflections, or planes, requires sampling over large angles and crystal orientations. However, if a crystal is finely ground, then it ideally represents all orientations at once, especially if the sample is rotated while collected. This is the advantage of powder diffraction over single crystal diffraction - it allows to collect over a larger range of orientations (planes) all at once.

There are also many additional consideration to consider when examining a powder diffraction pattern. The peak positions are due to the size of the unit cell, and depending on the symmetry of the atomic positions, certain reflections may be systematically absent, meaning that constructive interference is unable to happen in those planes. Peaks sharpness is mainly due to crystallite size, larger crystals have more narrow, more intense reflections and vice versa. Strain can

also effect the peak sharpness, though they have different θ dependencies, shown by Eq. (4) for size and Eq. (5) for strain.

$$\beta_L = \frac{K\,\lambda}{L\,\cos\theta} \tag{4}$$

$$\beta_E = C\,\varepsilon\,\tan\theta \tag{5}$$

where β is the full-width half maximum of the peaks, K is a constant close to unity, C is a constant from 2-4, L is the crystallite size, and ε is the apparent strain. It is important to note that these factors do not change the overall intensity of a reflection, rather they broaden the peak to appear less intense.

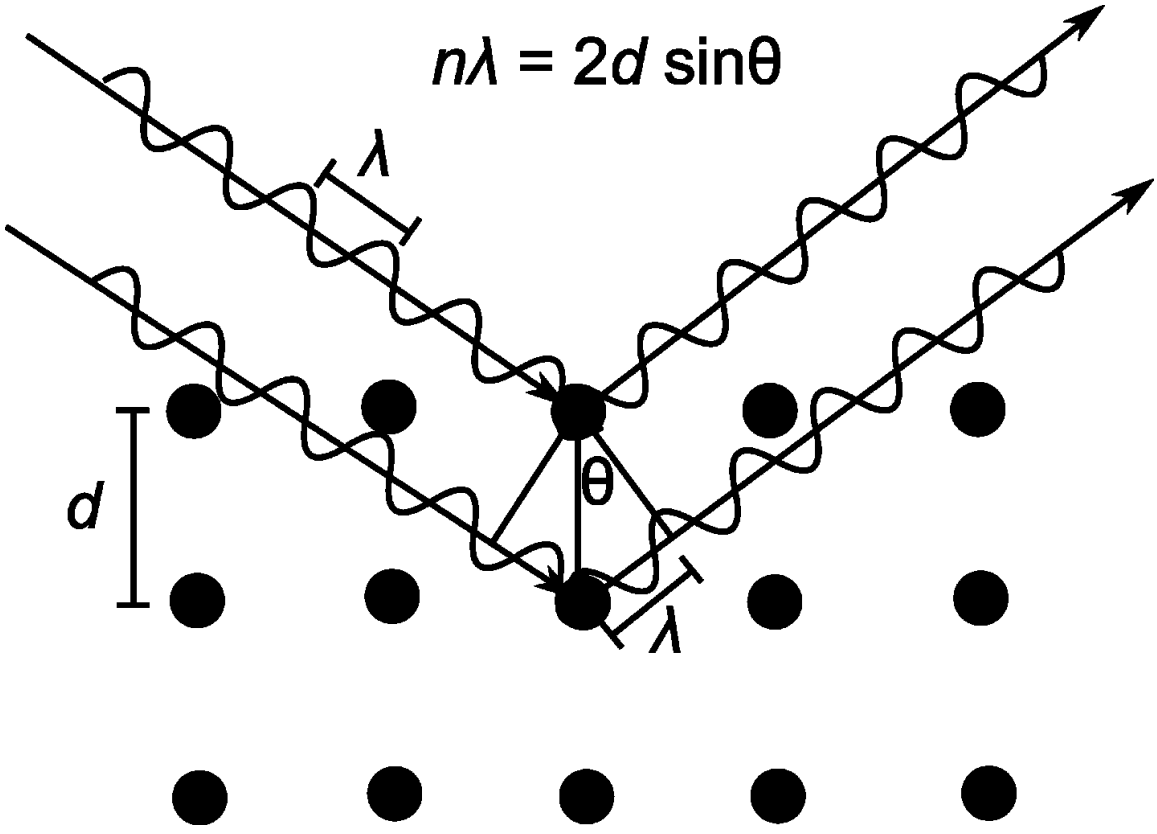

Figure 1.11: For an ordered crystalline material, the diffracted waves will constructively interfere with each other when Bragg's law, $n\lambda = 2d\sin\theta$, is met.

The relationship between incident wavelength and diffraction angle is clearly seen in the diagram.

The actually intensity of the peak is then solely due to the form factor or cross section, depending on the type of incident radiation. In other words, this means that the intensity is due to the atoms which reside in each plane, giving a unique diffraction pattern (or "fingerprint") for each type of material. There are other effects as well though, such as preferred orientation or stacking faults, which can also effect a pattern. In both cases this means that certain peaks may appear more or less intense depending on the ordering of certain orientations.

1.1.9 Pair Distribution Analysis

As an alternative to diffraction, pair distribution analysis (PDF) can also be conducted. Both powder and single crystal diffraction give crystallographic information on length scales ~10-100 nm. PDF can give crystallographic information of smaller lengths scales (~1-10 Å) and also indicates if the same atomic order exists on both long and short length scales.

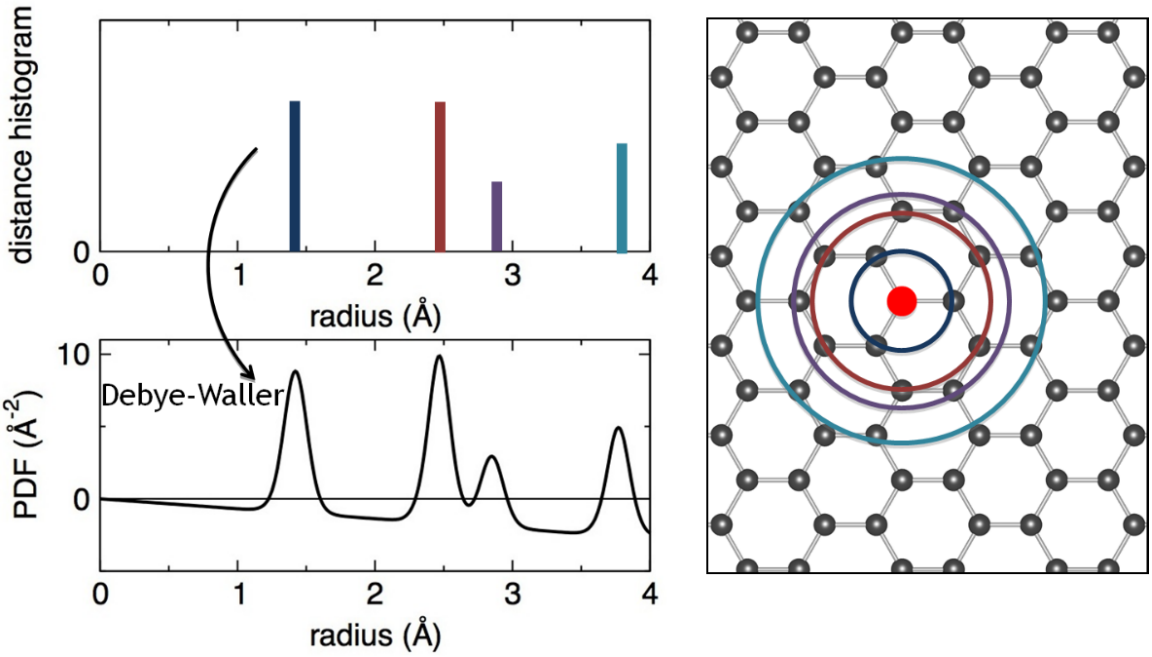

Figure 1.12. Pair distribution analysis gives atom-atom histogram of atomic distances in a material, and the peaks are broadened by temperature (Debye-Waller factor). Figure courtesy of J.R. Neilson.

Figure 1.12 demonstrates the effectiveness of PDF, as it presents an atom-atom histogram of atomic distances in a material. The upper left corner of Figure 1.12 displays such a histogram, based on the crystallographic structure on the right of Figure 1.12. Lastly, the bottom left corner of Figure 1.12 exhibits an example experimental PDF data. The experimental data is broadened due to thermal motion, which is described by the Debye-Waller factor.

1.1.10 Crystallographic Significance Tests

When conducting refinements, one is often left with the quandary of how "good" a certain type of fit might be. As I mentioned, there are many factors which can make model fit more poorly to the data than it should, but it is also possible that a poor fit is due to an incorrect model. In order to test the likelihood of

alternative models (i.e. alternate spacegroups, anisotropic thermal broadening, static displacements, etc.) a Hamilton R-ratio test[12] or a χ^2 ratio test[13] are used. The formula the Hamilton R-ratio and χ^2 ratio tests are shown in Eq. (6) and (7) respectively.

$$\mathbb{R}_{b,n-m,\alpha} = \left[\frac{b}{n-m} * F_{b,n-m,\alpha} + 1\right]^{\frac{1}{2}} \quad (6)$$

$$T_{b,n-m,\alpha} = \frac{\chi_1^2}{n-m-b} \Big/ \frac{\chi_2^2}{n-m} \quad (7)$$

where b is the dimensional of the hypothesis (difference between number of variables), n is the number of observations, m is the number of variables, α is the statistical significance level, and $F_{b,n-m,\alpha}$ is the relevant value F distribution value given b, n-m (degrees of freedom), and α. Both $\mathbb{R}_{b,n-m,\alpha}$ and $T_{b,n-m,\alpha}$ typically compute a value close to one.

For Hamilton R-ratio tests, the value of $\mathbb{R}_{b,n-m,\alpha}$ is then compared to a ratio of R_{wp} (weighted sums of residuals between the model and data) values, and if the values of R_{wp1}/R_{wp2} is greater than $\mathbb{R}_{b,n-m,\alpha}$ then it is statistically significant at the level of α used.

For χ^2 ratio tests the value of $T_{b,n-m,\alpha}$ is compared to F distribution values using n-m-b and n-m instead of b and n-m for the two variable degrees of freedom. This also uses crystallographic χ^2 refinement values, rather than R_{wp}, to

determine the ratio. If the value of $T_{b,n-m,\alpha}$ is outside the $F_{n-m-b,n-m,\alpha}$ value then it is considered statistically significant at the α limit chosen.

Care should be taken when doing these statistical tests, as the Hamilton R-ratio test is often misused and statistical significance can be shown even when it is not valid. This is why it is often best to use both tests rather than just one. Additionally, the Hamilton R-ratio test is only meant to be used to be compare two models where one is a subset of the other.[14] Likewise, care should be taken when choosing the correct n value, as there is considerable debate whether the number of observations should include the number of reflections or the number of data points collected. It can be argued that it is technically more correct to use the number of data points, as the absence of a peak should equally contribute to the validity of a model.[14] Due to this debate I find that it is best to calculate using multiple values and ensure that the statistical significance holds up for both choices of n and for both Hamilton R-ratio and χ^2 ratio tests.

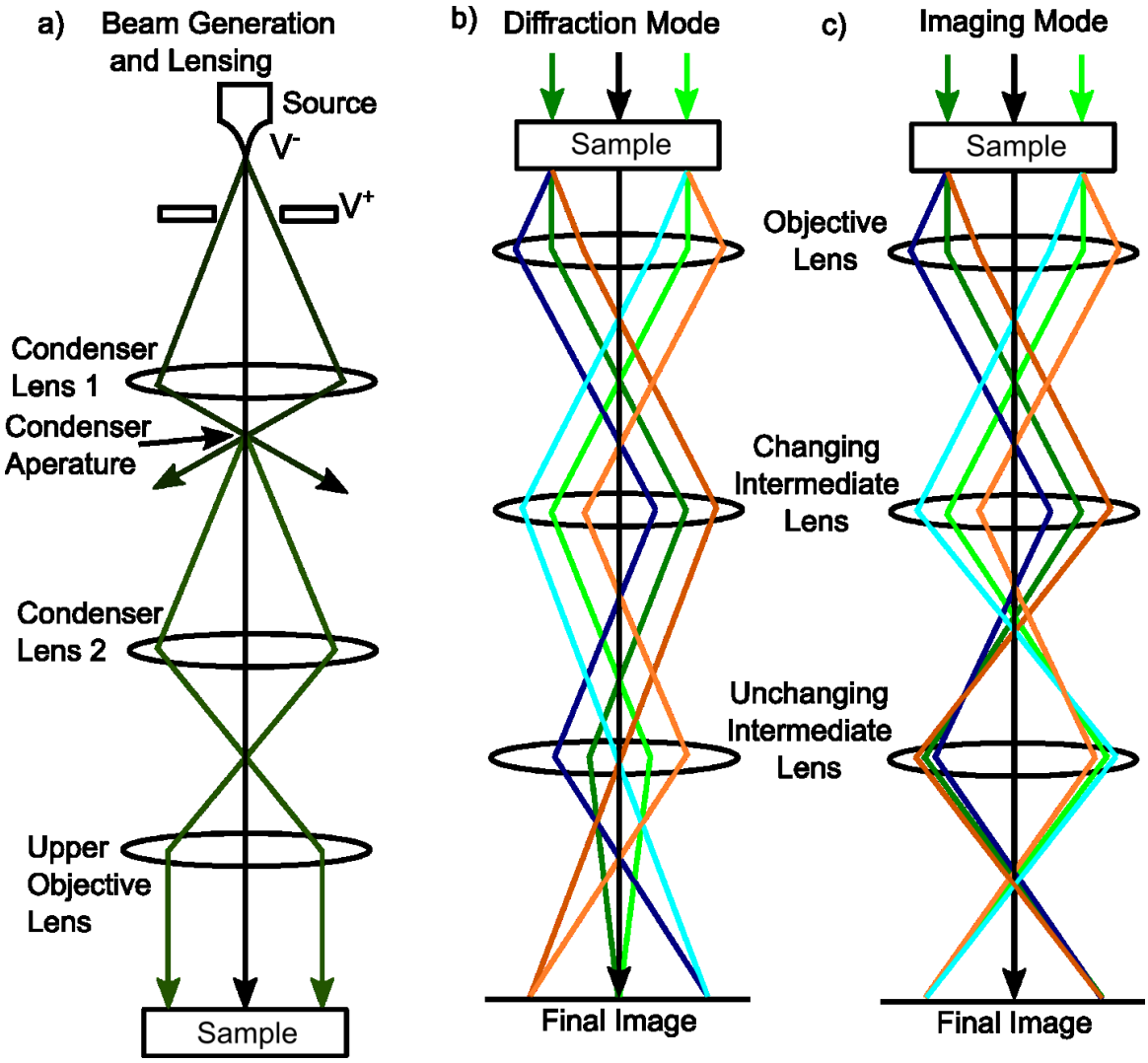

Figure 1.13: a) Transmission electron microscope beam generation and lensing. A small bias voltage extracts electrons from the source and magnetic lenses are used to condense and guide the beam to the sample. When electrons hit the sample they diffract and transmit, and depending on the strength of the lens either **b)** diffracted or **c)** transmitted electrons are visualized in the final image.

1.1.11 Transmission electron microscopy

An alternate type of radiation for examining atomic structure is electrons. Electrons scatter more strongly than X-rays and neutrons though they can also transmit through a thin sample if accelerated enough. This requires extremely thin samples, as the ability for electrons to penetrate a material diminishes

exponentially the thicker a sample is. Using electrons in this way is known as transmission electron microscopy (TEM), and is an extremely informative technique.[6]

Figure 1.13a demonstrates the basic set up of a TEM. A filament with an atomically thin tip is used to create the electron beam. Then a small extraction voltage is used to extract electrons off of the tip, followed by a series of lenses to focus and accelerate the electron beam. Focusing a charged beam can be accomplished by either a voltage or magnetic field, though for TEM a magnetic field is used because the final electron current of 100-300 keV, would require extremely dangerous voltages of several orders of magnitude larger. Using a magnetic field to accelerate a charge beam however creates helicity in the beam as it focuses it, which creates other interesting effects.

Since electrons also scatter on similar length scales as X-rays and neutrons, they are also used to observe diffraction. However electron transmission requires small sample sizes and only one certain orientation, or plane, at a time. This diffraction pattern looks very different than a powder diffraction pattern, as a powder pattern is essentially a one dimensional average of all of the possible diffraction spots, while an electron diffraction pattern is a cut of the Ewald sphere, which is a three-dimensional pattern of diffraction spots. This technique is incredibly powerful as looking at the right crystal direction can provide direct experimental evidence of the lattice parameter and symmetry inherent of a

structure. This information can be lost in averaging over all orientations for a powder diffraction pattern. In addition, because electrons scatter strongly with materials, additional disorder can be observed, seen as diffuse scattering. This makes electron diffraction an extremely important complimentary tool to verify or directly observe information related to the structural model.

Alternatively, by changing the settings of the magnetic lenses, TEM can observe atomic structure, seen in Figure 1.13c. However, due to the strongly scattering nature of electrons, and the amount of lensing required to focus the beam, great care must be taken to get reliable high-resolution TEM data, as the beam must be aligned and stigmated properly, both before and after going through the sample.

1.1.12 Ternary Phase Diagrams

Once initial experiments have been conducted, and the proper radiation has been used to identify what materials are present, further experiments are conducted to identify the stoichiometry of new phases. For instance, consider the ternary phase diagrams in Figure 1.14. To understand ternary phase diagrams, we only need understand that each corner represents 100% of each element and each edge is a binary phase diagram. Ternary phases are identified by looking at a percentage of each element of the total, and only two are needed to identify the location of a phase.

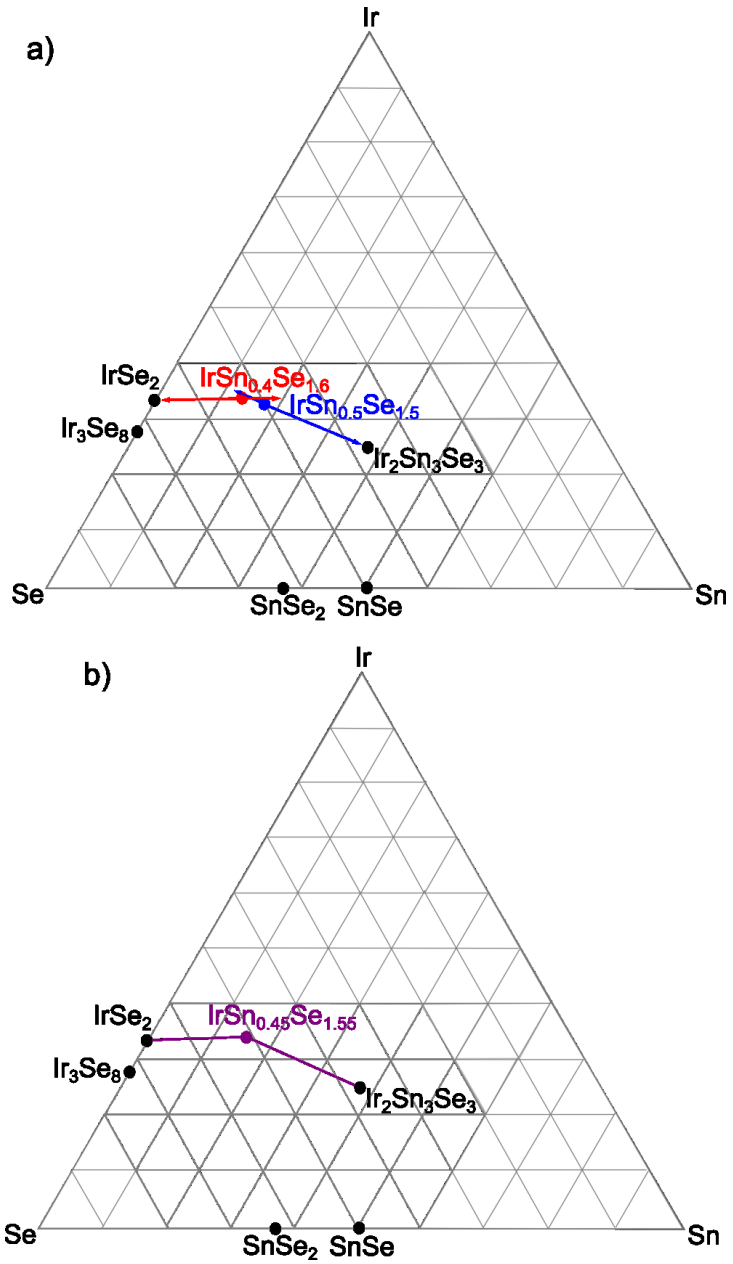

Figure 1.14: Ternary phase diagrams. **a)** Initial investigations targeting $IrSn_{0.5}Se_{1.5}$ and $IrSn_{0.4}Se_{1.6}$ led to an unknown phase and $Ir_2Sn_3Se_3$ and $IrSe_2$ impurities respectively. The impurities point to the mystery phase being in the opposite direction. **b)** Final phase diagram, showing tie lines between the compounds.

Figure 1.14a displays the phases $IrSn_{0.5}Se_{1.5}$ and $IrSn_{0.4}Se_{1.6}$. Targeting either compound leads to a single unknown phase and known impurities; targeting $IrSn_{0.5}Se_{1.5}$ yields $Ir_2Sn_3Se_3$ impurities, while targeting $IrSn_{0.4}Se_{1.6}$ yields

$IrSe_2$ impurities. This means that the impurity phase's stoichiometry must match a $IrSe_2$ deficient $IrSn_{0.5}Se_{1.5}$ and a $Ir_2Sn_3Se_3$ deficient $IrSn_{0.4}Se_{1.6}$, hence the unknown phase exists in the opposite direction of the impurity phases. This points to the identity of a $IrSn_{0.45}Se_{1.55}$ phase. This standard process that can be followed in order to determine the correct stoichiometry of an unknown phase to ultimately obtain phase pure materials.

1.1.13 Simulated Annealing

Once a new material is determined to be phase pure, the structure of this phase must be determined. Initial tools, such as electron diffraction, or peak searching algorithms on powder diffraction patterns, can be used to get an initial unit cell and symmetry. This verifies where peak positions reside, however determining where the atoms are within a unit cell is much more challenging. In recent years, due to more powerful computer processors, this process has become much easier.

Though one could systematically test all of the different atomic positions for each predicted atom type, this process would be too time consuming to be useful. Instead, fitting software can randomize the position of atoms, see how well it fits, and randomize it again. This heuristic approach, over long enough time scales, can lead to acceptable solutions. However, even this approach may not lead to a global minimum.

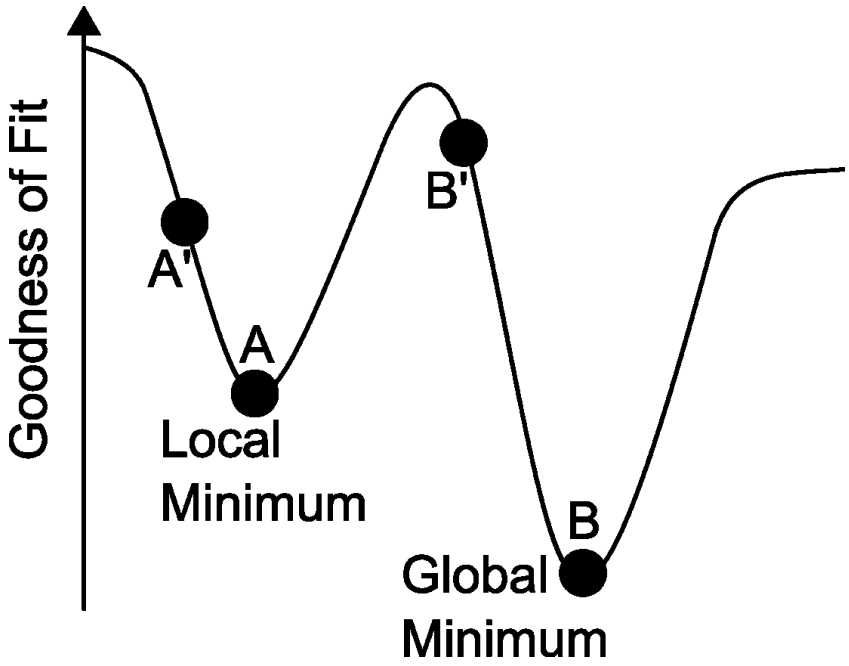

Figure 1.15: When refining an initial experiment (A') one will often end up at a local minimum (A) rather than a global minimum, meaning the incorrect solution. By perturbing the system through simulated annealing the refinement can overcome maximum and start refining again (B'), allowing access to the global minimum (B).

The penultimate goal of any refinement is to end up at the global minimum, it is easy to get stuck at a local minimum. When a refinement is stuck at a local minimum it means that the refinement procedure cannot overcome a local maximum to continue the refinement process. This is displayed by Figure 1.15. Randomizing the atomic positions overcomes local maximum, though an alternative approach, simulated annealing, uses a more sophisticated process to reach the same goal. Instead of randomizing the atoms in a material, it uses temperature as a variable. Just as heating a material creates thermal energy, or atomic vibrations, here an annealing step is used to delocalizes the atoms, and then as the temperature is decreased, the atoms rest into some final position. This

iterative process is run until the global minimum is found, and is more powerful than simply randomizing the atomic positions.

This is not to say that simulated annealing alone will entirely solve a structure. Often initial unit cells, symmetries, or even formulas can be wrong, as this is only a heuristic approach. Additional effects, such as stacking faults or preferred orientation can also make solving unknown structures much more difficult. When possible, an equivalent phase is used to begin this process, as starting the process from scratch is often incredibly challenging.

1.2 Physical Properties

Once a new material is phase pure, and the structure is known, it's properties can be characterized to determine its usefulness. It is important to know that a material is phase pure, as a small amount of impurities can often lead to extremely different properties. Likewise, the amount of defects in a material can have a significant impact on its properties.

1.2.1 Resistivity

The electrical resistance of a material is easily measured, and the trend of the response versus temperature can give insightful information about a material. In fact, the response versus temperature can also give information about the band structure. Figure 1.16 shows three different DOSs and three different resistivity

versus temperature trends, all of which rely on where the Fermi level (E_F) lies and the gap between the valence and conduction bands.

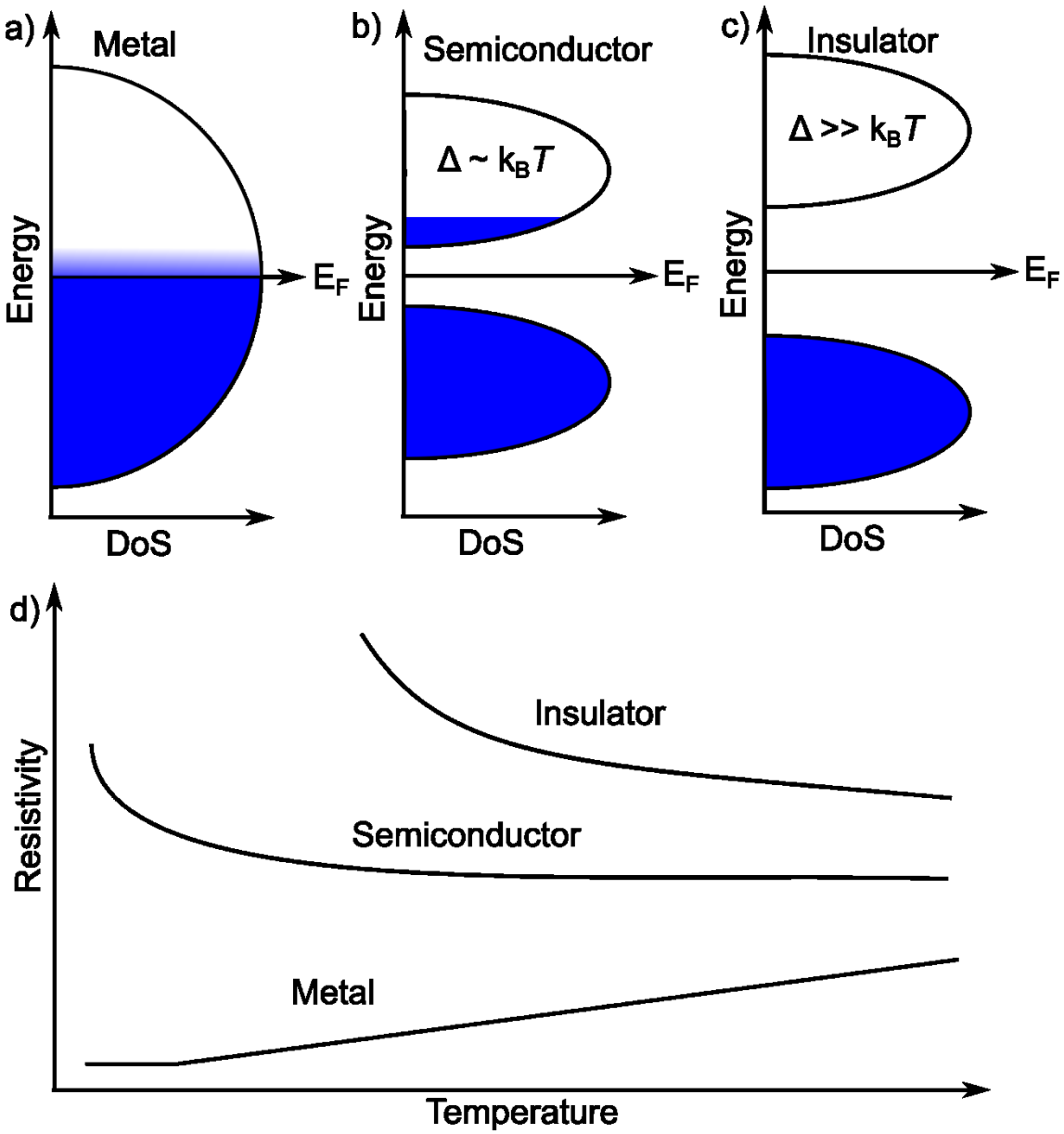

Figure 1.16: Trends of electrical resistivity. **a)** A material with no gap (Δ) is a metal. **b)** For a semiconductor, thermal excitations excite electrons across a small gap into the conduction band. **c)** In an insulator the gap is too large for electrons to be thermally excited. **d)** The shape of a resistivity versus temperature curve is indicative of the electronic behavior.

If the Fermi level sits in the middle of a band, then the material is a conductive and a metal, as it requires little energy to promote an electron above the Fermi level. This means that little to no energy is required in order to create conduction electrons. As thermal energy, denoted $k_B T$, increases, thermal atomic motion (vibrations) increases and conduction electrons are scattered more strongly, meaning metals are more resistive at higher temperatures. At lower temperatures the resistivity of a metal decreases to a finite value, related to the density of electrons at the Fermi level.

In contrast, if the Fermi level sits between two bands, then the material is insulating or semiconducting, depending on the size of the gap between the valence and conduction bands, Δ. If the gap is on the order of thermal fluctuations, $k_B T$, then the material is considered semiconducting. If the gap is much larger than $k_B T$ then thermal fluctuations cannot excite carriers above the Fermi level and the material is insulating. In both cases thermal energy helps the conduction process, and these materials becomes more insulating as temperature is decreased.

Experimentally this is easy to measure, using either a two or four probe measurement, shown in Figure 1.17a. The material specific Resistance (R), or the resistivity (ρ), can then be determined using $\rho = R\frac{A}{L}$. Measuring the exact dimensions can be extremely challenging, hence residual resistivity ratios are used to evaluate trends, rather than determine the exact material specific

resistivity. Even with these ratios, if a band gap exists it can be determined using the Arrhenius equation, $\rho = \rho_0 e^{\Delta/k_B T}$, where ρ_0 is a normalization factor and Δ is the band gap of the material.

1.2.2 Resistivity under Fields

Resistivity can also be measured as a function of field, though the response can vary depending upon the experimental configuration. Figures 1.17a and 1.17b demonstrate two alternative setups, which measure slightly different properties. When $\rho = \rho_{yy}$ (=ρ_{xx}) is measured as a function of field, then the response is magnetoresistance. When $\rho = \rho_{xy}$, is measured as a function of field, then the response instead gives the Hall resistance.

A typical magnetoresistance response is shown in Figure 1.17c. This is a positive response, symmetric around the origin. The dependence of this resistivity as a function of field can be defined by Kohler's law, meaning $\rho_{xx} = 1 + (\mu H)^2$, where H is the applied field and μ is the mobility of the carriers.[15] If the response is not positive, then there are likely several different types of conduction species (electrons or holes). There also are many reasons why the magnetoresistance does not follow Kohler's law, from defects, to anisotropic conduction, to more exotic effects which could lead to colossal magnetoresistance.[1]

Figure 1.17: a) Typical four probe resistivity setup. **b)** Typical experimental setup for measuring the Hall resistance. **c)** Symmetric magnetoresistance response. **d)** Typical antisymmetric Hall response.

A typical Hall resistance is shown in Figure 1.17d. Hall resistivity is linear with field, and antisymmetric around the origin. This response need not have a positive slope, rather the sign and magnitude of the slope indicate the type and amount of carriers in the material. If the slope is negative then the carriers are electrons, while the slope is positive for holes. The Hall resistance can also be described as $R_H = {}^{-1}/_{ne}$ for electrons, where e is the fundamental charge and n is the carrier concentration. Much like for magnetoresistance, if multiple carrier types exists in a material then the Hall resistance measures an average of all carrier types, where holes and electrons effectively cancel each other out. This is why it is important to measure the resistivity as a function of field at several temperatures, rather than at a single temperature. This allows for monitoring both thermally excited carriers, as a function of temperature, and extrinsic carriers from defects.

Obtaining a quality Hall resistivity response (perfectly linear) can be a challenging endeavor, as the leads must be set up perfectly perpendicular, as in Figure 1.17b, to obtain a perfect ρ_{xy} response. Experimentally, both magnetoresistance and Hall resistance responses are often seen at the same time. However, because each response follows different symmetry around the origin, the two responses can be separated by symmeterizing the data. This means that a single measurement of field versus resistivity can lead to both magnetoresistance and Hall resistance data. The absolute magnitude of the response may not be entirely correct, but the trends are intrinsic to a material.

1.2.3 Heat Capacity

The specific heat of a material describes a materials ability to change its internal energy as a function change in temperature. Thermodynamically, it is described at constant volume or pressure, given by: $C_p = \left(\frac{\partial Q}{\partial T}\right)_p$ or $C_v = \left(\frac{\partial Q}{\partial T}\right)_v$, where Q is internal energy. The difference between these two at higher temperatures is the molar gas constant, R, though at lower temperatures they are roughly equivalent. If measuring heat capacity as a function of temperature, it is experimentally easier to measure at constant pressure than constant volume. Heat capacity is also related to the amount of disorder, or entropy, of a system as $C_p = T\left(\frac{\partial S}{\partial T}\right)_p$.

To understand the relationship of heat capacity versus temperature, we must first understand the contributions to the energy of a system, namely

conduction electrons and lattice vibrations (phonons). Eq. (8) presents a basic equation for understanding the energy of a system as a function of temperature. This equation sums over all states, where $P(\varepsilon_F)$ is the probability distribution of states around the Fermi energy, $\eta(w_i)$ is a number density of states, and $\hbar w_i$ is the energy of each state i. Depending on whether we are counting bosons (phonons) or fermions (electrons) the probability distribution is described by Eq. (9) or Eq. (10), known as the Bose-Einstein and Fermi-Dirac distributions respectively.[5]

$$E = \sum_i P(\varepsilon_F) \;\; \eta(w_i) \;\; \hbar w_i \tag{8}$$

$$P(\varepsilon_F)_{BE} = {}^{1}/_{(e^{(\varepsilon_i - \varepsilon_F/k_B T)} - 1)} \tag{9}$$

$$P(\varepsilon_F)_{FD} = {}^{1}/_{(e^{(\varepsilon_i - \varepsilon_F/k_B T)} + 1)} \tag{10}$$

Once we have the proper distribution, after integrating $(C_p = \left(\frac{\partial E}{\partial T}\right)_p)$, three equations are obtained, shown below. Eq. (11) displays the heat capacity for conduction electrons, where $\eta(\varepsilon_F)$ is a number density of states at the Fermi level, or rather the number of conduction electrons. Eq. (12) and (13) model Einstein and Debye phonon heat capacity contributions. These models optic and acoustic modes, which are lattice vibrations with small and large dispersions in frequency respectively. Here $\theta = \hbar w_i / k_B$ where $\hbar$ is the reduced Planck constant and w_i is the associated frequency of each type of vibration. The oscillator strength, *s*, is also important, as the total number of oscillators add up to the total

number of atoms per formula unit, N, just as the total heat capacity at higher temperatures is equivalent to the Delong-Petit limit, $3NR$. More details into the derivation of these equations can be found in Ref. 2.

$$C_{el} = \frac{1}{3}\pi^2 k_B^2 \eta(\varepsilon_F) T = \gamma T \tag{11}$$

$$C_{Eins} = 3sR\left(\frac{\theta_E}{T}\right)^2 \frac{\exp(\theta_E/T)}{[\exp(\theta_E/T)-1]^2} \tag{12}$$

$$C_{Debye} = 9sR\left(\frac{T}{\theta_D}\right)^3 \int_0^{\theta_D/T} \frac{(\theta/\mathrm{T})^4 \exp(\theta/T)}{[\exp(\theta/T)-1]^2} d\frac{\theta}{T} \tag{13}$$

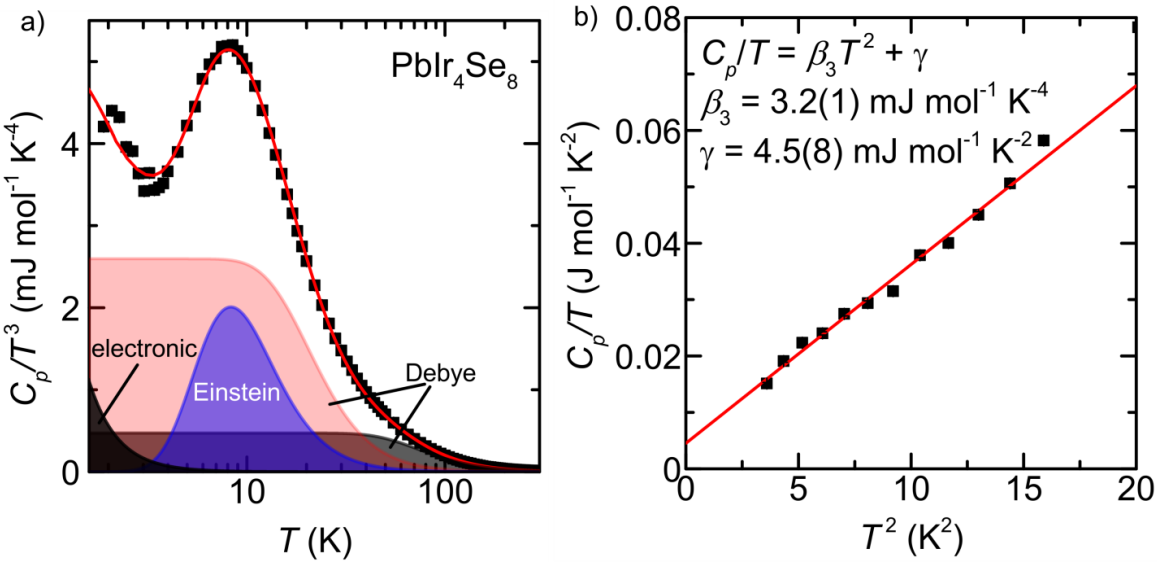

Figure 1.18: a) C_p/T^3 vs T plots differentiate between Einstein, Debye, and electronic contributions. Here Einstein specific heat contributions are seen as a peak, Debye contributions are constant at low temperature, and electronic contributions exponentially increase at low temperatures. **b)** C/T vs. T^2 plots at low temperatures linearize the electronic (γ) and phonon (β_3) contributions. This allows for accurate determination of the electronic specific heat and a good starting point for determining the phonon contribution.

Fits to heat capacity data, using these contributions, is shown in Figure 1.18a, where different contributions are be visualized plotting as C_p/T^3 vs. T,

Presented this way, the magnitude of Debye modes increase until becoming constant at low temperatures, Einstein modes appear as a broad feature, and the electronic contribution has an exponential increase at low temperatures. Alternatively, this approach can be simplified by using a Taylor series to represent the phonon contribution to specific heat shown in Eq. (14). At low temperatures, when $T \ll {}^{\theta_D}/_{50}$, higher order terms are negligible and can be ignored.[2] Plotting this as C_p/T vs. T^2 linearizes this equation so it can be fit to retrieve accurate γ values, shown in Figure 1.18b.

$$C_p = \gamma T + \beta_3 T^3 + \beta_5 T^5 + \beta_7 T^7 \approx \gamma T + \beta_3 T^3 \quad (14)$$

Once both of these types of fits are completed the types of lattice vibrations, how conductive the material is, and even types of disorder can be determined. Heat capacity is the definitive measurement to be done on any material, especially because the measurement is a bulk technique and is related to the entropy for a material.

1.2.4 Magnetization

Another important physical property for understanding materials is magnetization. When a magnetic field, *H*, is applied, the material's response is given by its magnetic susceptibility, χ_M, and the magnetization of the sample, *M*. When the magnetization of the sample is the same in all directions, or isotropic, this is approximated as $M = \chi_M H$. The magnetic response of a material depends

on the amount of unpaired electrons in a material and how they order with one another.

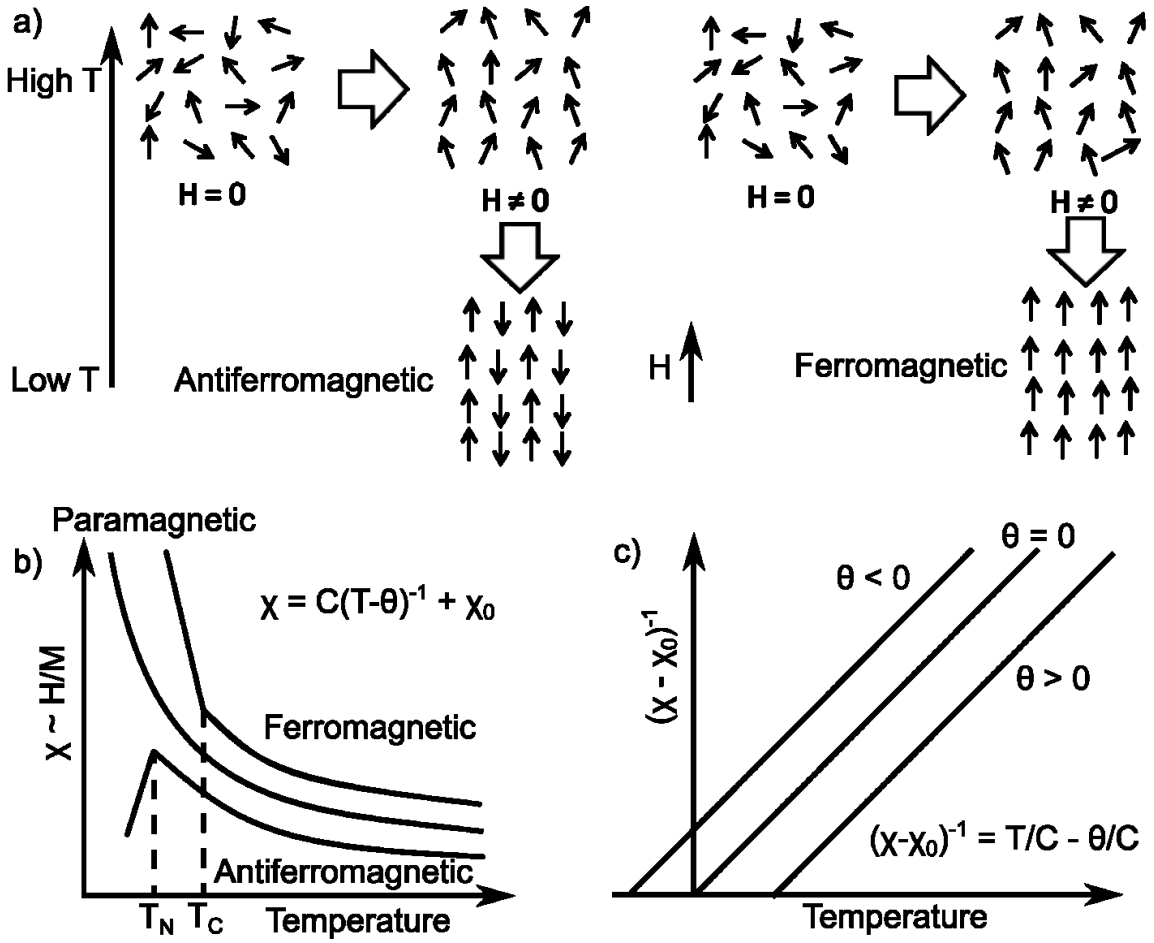

Figure 1.19: a) A paramagnetic material contains unpaired electrons which can oppose (Antiferromagnetic) or align with (Ferromagnetic) an applied field (H). **b)** The magnetic susceptibility trends are shown for these three types of magnetism. Ferromagnetic order occurs at the Curie temperature (T_C) and antiferromagnetic ordering occurs at the Neel temperature (T_N). c) Linearizing the Curie-Weis law allows for determining the interaction strength magnitude and sign (θ).

The first type of magnetic response is diamagnetism, this is a weak, negative response, for a material that is purely insulating, i.e. has no unpaired spins. This is a negative response as the material seeks to shield full orbitals from the effects of the magnetic field, opposing the field. The second type of response

is paramagnetism, due to some amount of unpaired spins. At higher temperatures the unpaired electrons will all partially align with the field, as their ordering competes with thermal fluctuations. If this effect is due to conduction electrons, then it is known as Pauli paramagnetism, and is temperature independent. At lower temperatures, as thermal fluctuations decrease, unpaired electrons can order in a variety of ways as shown in Figure 1.19a.

If unpaired electrons align anti-parallel with one another, then the negative response is antiferromagnetism. If the unpaired electrons order parallel with one another, then the positive response is ferromagnetism. Alternatively, these responses can be described by Eq. (15):

$$\chi_M - \chi_0 = \frac{C}{T-\theta} \tag{15}$$

$$1/(\chi_M - \chi_0) = \frac{1}{C}\,T - \frac{\theta}{C} \tag{16}$$

where χ_M is the magnetic molar susceptibility, χ_0 is a temperature independent diamagnetic response, C is the Curie constant, and θ is the Weiss temperature which measures the magnetic interaction strength. Though C is a constant, it is related to the effective magnetic moment per ion as $p_{eff} = \sqrt{8C}$, meaning its value changes per element and charge of the ion. By rearanging Eq. (12) into Eq. (13), this not only linearizes the equation, but also displays the type of magnetism based off of the intercept (θ/C), shown in Figure 1.19b. Here C is constant, so the sign of the intercept is based off of θ alone. When θ is positive

the material is antiferromagnetic, when θ is negative then the material is ferromagnetic.

There are also several complications which can also arise, such as partial magnetic ordering, or multiple degenerate magnetic ground states, but for the purpose of this dissertation they are not relevant.

1.2.5 Thermal Transport

The last material property discussed herein is the ability of a material to transport heat. More importantly, this property relates to a material's usefulness as a thermoelectric, where it is desired for a material to conduct electricity but not conduct heat. The usefulness of a material that can conduct electricity but not heat is incredibly widespread, as it creates an alternative energy device that can be attached to any generator or motor that has significant heat loss.

This ability to conduct electricity but not heat relates to the Seebeck coefficient, where when two metals are put in contact in a loop, with a temperature difference across them, then a voltage is created. This relates to the Seebeck coefficient, in Eq. (14) where h is Planck's constant, m^* is the enhanced mass, and n is the carrier density in a material. Thus this describes the ability of charges (holes or electrons) to create a voltage difference as a function of temperature.[3]

$$S = \frac{8\pi k_B^2}{3eh^2} m^* T \left(\frac{\pi}{3n}\right)^{2/3} \propto m^* n^{-2/3} T \tag{17}$$

In order to understand how "good" of a thermoelectric a material is, the figure of merit, ZT, is used:[3]

$$ZT = S^2\sigma T/\kappa \quad (18)$$

where σ is the electrical conductivity and κ is the thermal conductivity, and a higher value represents a more useful thermoelectric. If a material has a large electrical conductivity but a small thermal conductivity, this gives a large ZT. Unfortunately, these two properties are directly related to each other, and values of ZT are not known to be significantly high to be considered extremely useful. Disorder actually plays a significant role in good thermoelectrics, as defects would disrupt the lattice (thermal conductivity), and may not disrupt the electrical conductivity as much. Additionally most "good" thermoelectrics decompose at the temperatures where they might be considered useful.

1.3 Conclusions

Using the knowledge built from the introduction, the following chapters describe several new compounds. The first, $(BiSe)_{1.15}(TiSe_2)_2$, was discovered using the homologous series $(MX)_{1+\delta}(TX_2)_n$, and the relevant structural and physical property characterization is presented. As Cu_xTiSe_2 is a superconductor,[16] studies were also conducted to see if the double $TiSe_2$ layer in $(BiSe)_{1.15}(TiSe_2)_2$ superconducts when doped with Cu. Though we were able to dope the misfit

compound with Cu it did not become superconducting. This was not surprising and our results further indicate that the three dimensional charge density wave in $TiSe_2$ mediates its superconductivity.

The next two chapters are a result of attempts to expand the $(MX)_{1+\delta}(TX_2)_n$ series to include Ir, as $IrTe_2$ is isostructural to $TiSe_2$, and has much stronger spin-orbit coupling. However, because solid state synthesis yields thermodynamic products, the compounds Ir_2SnSe_5, $IrSn_{0.45}Se_{1.55}$, and $PbIr_4Se_8$ were discovered instead. Chapter 3 focuses on the characterization of the tin iridium selenides, while Chapter 4 describes the characterization of the lead iridium selenide. Due to the strong spin-orbit coupling of iridium, band structures are investigated to look for exotic electronic behavior. Similarly all of these iridium compounds host anion-anion bonding, which appears to be a hallmark of Ir^{3+} chalcogenides.

2 The New Misfit Compound $(BiSe)_{1.15}(TiSe_2)_2$ and the Role of Dimensionality in the $Cu_x(BiSe)_{1+\delta}(TiSe_2)_n$ Series

This work was co-written with the following authors and is published under the following citation:

Journal of Solid State Chemistry **209**, 6-12 (2014)

http://dx.doi.org/10.1016/j.jssc.2013.10.014

Benjamin A. Trump,[a,b] Kenneth J.T. Livi,[c] and Tyrel M. McQueen[a,b]

[a]Department of Chemistry, Johns Hopkins University, Baltimore, Maryland 21218, United States

[b]Department of Physics and Astronomy, Institute for Quantum Matter, Johns Hopkins University, Baltimore, Maryland 21218, United States

[c]HRAEM Facility, Department of Earth and Planetary Sciences, Johns Hopkins University, Baltimore, Maryland 21218, United States

2.1 Introduction

Homologous series offer a systematic method of tuning both the structures and properties of new materials[17]. The series $(MX)_{1+\delta}(TX_2)_n$ is one such example, where M = Sn, Sb, Pb, Bi, or lanthanides, T = Ti, V, Cr, Nb, or Ta, X = S or Se, and δ is a small number between 0 and 0.28.[8] The MX layers are of a rock-salt type, while the TX_2 layers consist of edge-sharing polyhedra.[8] The significance of this series is not only the myriad of possible elements, but also the ability to systematically vary n, the number of TX_2 layers in the structure. Compounds of small values of n are of great interest due to their low thermal conductivities.[8,18,19] For larger n, the influence of dimensionality on the electronic properties of transition metal dichalcogenides can be explored. For example, many transition metal dichalcogenides exhibit a charge density wave (CDW) transition in the bulk that is not present in compounds of the series where n = 1.[20–23] This implies that an intermediate n should exist where a crossover to a CDW state occurs.

When the periodicity of the MX and TX_2 units does not match ($\delta \neq 0$) the compound is known as a misfit. Most in-depth studies of misfits have been done for T = Nb and Ta, such as $(PbSe)_{1.14}(NbSe_2)_n$ (n = 1, 2, 3),[24] $(LaSe)_{1.14}(NbSe_2)_2$,[25] $(PbS)_{1.13}(TaS_2)$ and $(BiS)_{1.07}(TaS_2)$,[26] due to their superconducting properties. These TX_2 layers are of the "2H" type, which are edge-sharing trigonal prisms. For T = Ti, V, or Cr the layers are of the "1T" type, which are edge-sharing

octahedra. Of these, several exist for n > 1 for only $TiSe_2$, including $(LaSe)_{1.20}(TiSe_2)_2$ [27] and $(PbSe)_{1.16}(TiSe_2)_2$ [28].

$TiSe_2$ has a well known CDW at T = 202 K, with a three dimensional commensurate wavevector k = (1/2,1/2,1/2) [29–32] with chiral attributes [33,34]. Although the CDW in 1T-$TiSe_2$ has been studied for several decades, its origins are still contested, with theories ranging from an excitonic insulator[32,35–37] to some type of Jahn-Teller effect[38–41]. Bulk 1T-$TiSe_2$ is also a known superconductor when intercalated with Cu[16] or Pd[42]. The homologous series $Cu_x(BiSe)_{1+\delta}(TiSe_2)_n$ thus offers a route for systematically increasing the number of $TiSe_2$ layers to probe the importance of dimensionality on CDW formation and superconductivity.

Most misfit compounds are synthesized using chemical vapor transport.[8,24–28] Recent work demonstrates that electron beam evaporation can be used to create members of the series $(MX)_{(1+\delta)}(TX_2)_n$ for $n \geq 4$.[43,44] However, these compounds often have local disorder and are, thus, described as "ferecrystals".[45,46]

Here we report the synthesis, structure, and physical properties of single crystals of the compounds $(BiSe)_{1+\delta}(TiSe_2)$ and $(BiSe)_{1+\delta}(TiSe_2)_2$. $(BiSe)_{1+\delta}(TiSe_2)$ is previously reported as $BiTiSe_3$, though only resistivity[47] and *c*-parameter are known[48], while $(BiSe)_{1+\delta}(TiSe_2)_2$ has not previously been reported. We find that both exhibit metallic and diamagnetic behavior, with no sign of CDW formation

above T = 1.8 K. Further, intercalation with copper, $Cu_x(BiSe)_{1.15}(TiSe_2)_2$, ($0 \leq x \leq 0.10$) is also reported, but unlike the parent compound Cu_xTiSe_2,[16] no superconductivity is observed down to T = 50 mK.

2.2 Experimental

2.2.1 Preparation

Phase pure, single crystals of $(BiSe)_{1.15}(TiSe_2)_2$ and $(BiSe)_{1.13}(TiSe_2)$ were grown by vapor transport with $TeCl_4$ as a transport agent. Bi (Alfa Aesar 99.998%), Ti (Alfa Aesar 99.5%), and Se (Alfa Aesar 99.999%) in the molar ratio of 1:1:3 were sealed in an evacuated, fused-silica tube. The tube was first heated to 500°C and then heated further to 900°C at a rate of 50°C per hour. The temperature was maintained for 12 hours. Then, the temperature was immediately reduced to 680°C and maintained for two days. Finally, the sample was furnace-cooled to room temperature. The resulting boule was pulverized, pressed into a pellet, and resealed for a second heat treatment at 680°C for two days. This resulted in a multi-phase mixture of $(BiSe)_{1.13}(TiSe_2)$, $TiSe_2$, and Bi_2Se_3. A ~300 mg charge of this powder was then placed in the hot end of an evacuated quartz tube with $TeCl_4$ (~20 mg, STREM 99.9%) for chemical vapor transport with a temperature gradient of 750°C-680°C. After one week, shiny, plate-like crystals (2x4x0.01 mm^3) were obtained from the cold end. There were two kinds of

crystals, both with a metallic luster: silver $(BiSe)_{1.13}(TiSe_2)$ and slightly red/purple $(BiSe)_{1.15}(TiSe_2)_2$.

$Cu_x(BiSe)_{1.15}(TiSe_2)_2$ samples were prepared in a similar way, using high-purity stoichiometric amounts of Bi, Ti, Se, and Cu (STREM 99.9%) where $0 \leq x \leq 0.12$. These samples were heated using the same procedure, with the resulting boule after the second heat treatment being $Cu_x(BiSe)_{1.15}(TiSe_2)_2$ with 1-5% $TiSe_2$ impurities determined from powder X-ray diffraction (PXRD). For $x > 0.10$, a solid solution limit was hit and secondary phases appeared. The final x values presented are nominal compositions.

2.2.2. Characterization

Laboratory powder X-ray diffraction (PXRD) patterns were collected using Cu Kα radiation (λ_{avg} = 1.5418 Å) on a Bruker D8 Focus diffractometer with a LynxEye detector. Lebail refinements were used to determine lattice parameters from the PXRD data using TOPAS (Bruker AXS), calibrated internally with Si (a = 5.4310 Å)[49]. To obtain more insight into the structure and lattice parameters, transmission electron microscopy (TEM) was utilized, using a Phillips CM300 atomic resolution TEM, equipped with a Field Emission Gun with an accelerating voltage of 300 kV. Initial a and b lattice parameters were determined using selected area electron diffraction (SAED) collected on film (Kodak SO 163). Additional stacking information was determined using high resolution TEM

(HRTEM) with a CCD camera (Gatan Image Filter 200). Structures were visualized using VESTA.[50]

Physical properties of $(BiSe)_{1.15}(TiSe_2)_2$ and $(BiSe)_{1.13}(TiSe_2)$ (electrical, heat capacity, magnetization) were measured using single crystals in a Physical Properties Measurement System (PPMS, Quantum Design, Inc.). All measurements were conducted from T = 1.8 K to T = 300 K. Heat capacities were measured using the semi-adiabatic pulse technique, with three repetitions at each temperature, waiting for three time constants per measurement. Magnetic susceptibilities were measured with a $\mu_0 H$ = 0.1 T. Resistivity was measured using standard four-probe geometry. Heat capacity measurements on $Cu_{0.06}(BiSe)_{1.15}(TiSe_2)_2$ were conducted on a PPMS equipped with a dilution refrigerator for measurements of 0.05 K < T < 4 K.

2.3 Results and Discussion

2.3.1 Structure of $(BiSe)_{1.13}(TiSe_2)$ and $(BiSe)_{1.15}(TiSe_2)_2$

High resolution transmission electron microscopy (HRTEM) data for $(BiSe)_{1.15}(TiSe_2)_2$ oriented in the *bc* plane is shown in Figure 2.1(a). The image contains double rows of light spots separated by darker regions. The vertical repeat distance is 17.8 Å, in the range expected for such a double layer misfit. The *c* axis spacings are consistent with the double rows corresponding to $(TiSe_2)_2$ bilayers, and the darker regions BiSe layers (a simulation could determine

whether the light or dark regions are atoms, but this is not necessary to determine which layer type is which). A corresponding selected area electron diffraction (SAED) pattern oriented perpendicular to c^* is shown in Figure 2.1(b). All observed reflections in the SAED pattern are indexable by a combination of a triclinic (pseudo-cubic) BiSe cell and a hexagonal $TiSe_2$ cell (as is commonly done for misfits[8,24–28,51,52]). The more commonly used triclinic misfit cell for $TiSe_2$, which shares a common b and c axis with the BiSe cell, is also shown. In other words, describing the SAED data requires four, rather than the usual three, basis vectors (one, c*, is oriented out of plane). This is similar to what is found, for example, in the known $TiSe_2$ double layer misfit $(PbSe)_{1.16}(TiSe_2)_2$[28]. A corresponding powder x-ray diffraction pattern (PXRD) is shown in Figure 2.1(c), with Si as an internal standard. While (0 0 *l*) reflections are clearly visible, *h* or *k* reflections appear low in intensity and broad, as is typical for misfit-type compounds. This makes determination of the *c*-axis straightforward, but introduces difficulties in obtaining *a* and *b* lattice parameters with PXRD alone. As such, initial values of the *a* and *b*-axis lattice parameters for a Lebail fit were determined from the SAED data. Triclinic unit cells with *C*-1 symmetry were used for each layer type. The unit cells were constructed using $(LaSe)_{1.20}(TiSe_2)_2$ as a model, given the formulaic similarity and similar pattern of systematic absences in the data.[27] The Lebail fit was done using commensurate *b* and *c* lattice parameters with an incommensurate *a* lattice parameter for each layer type. The results are given in Table 2.1 with comparison to similar structure

types. Although Lebail refinements gave values with less than 0.02% error, several values fit equally well within the same range as the SAED errors. Further, the cell angles α, β, and γ, were allowed to vary by space group symmetry, though they refined to 90° within <0.7% error, and thus were fixed at that value. The errors reported in Table 2.1 represent our estimated total contributions of all of these factors. The values we determined fall within the range of similar Bi misfit compounds.[8] Figure 2.1(d) shows the proposed structure of $(BiSe)_{1.15}(TiSe_2)_2$, highlighting the incommensurate nature of the layers, as evidenced by differing *a*-axis lattice parameters seen in the SAED pattern (Figure 2.1(b)).

Table 2.1: Lattice parameters for $(BiSe)_{1.15}(TiSe_2)_2$ and $(BiSe)_{1.13}(TiSe_2)$ compared to known literature misfit compounds. Initial values were taken from representative SAED patterns, and then refined using Lebail fits to powder X-ray diffraction data. *a* and *b*-parameters were averaged over several possible values which fit equally well.

Compound	*Layers*	*a* (Å)	*b* (Å)	*c* (Å)	*S.G.*	*Ref*
Single layer-type						
$(BiSe)_{1.13}(TiSe_2)$	BiSe	6.2(2)	6.2(3)	23.7481(7)	*C*-1	This work
	$TiSe_2$	3.5(1)	6.2(3)	23.7481(7)	*C*-1	This work
$(PbS)_{1.18}(TiS_2)$	PbS	5.800(2)	5.881(1)	11.759(2)	*C*2/*m*	[35]
	TS_2	3.409(1)	5.881(1)	11.759(2)	$C2_1/m$	[35]
$(PbS)_{1.12}(VS_2)$	PbS	5.789	5.728	23.939	*C*2	[36]
	VS_2	3.256	5.728	23.939	*C*2	[36]
BiTiSe [$(BiSe)(TiSe_2)$]				11.84 (x2 = 23.68)		[32]
Double layer-type						
$(BiSe)_{1.15}(TiSe_2)_2$	BiSe	6.17(3)	6.23(4)	17.8103(1)	*C*-1	This work
	$TiSe_2$	3.56(3)	6.23(4)	17.8103(1)	*C*-1	This work

$(PbSe)_{1.16}(TiSe_2)_2$	PbSe:	6.14(2)	6.14(2)	18.247(2)	*Fm*-3*m*	[13]
	$TiSe_2$	3.553(1)	3.553(1)	18.247(2)	*P*-3*m*1	[13]
$(LaSe)_{1.20}(TiSe_2)_2$	LaSe	5.969(2)	6.118(2)	17.876(10)	*C*-1	[12]
	$TiSe_2$	3.556(2)	6.120(2)	17.859(9)	*C*-1	[12]
Infinite layer-type						
$TiSe_2$		3.535(4)	3.535(4)	6.011(5)	*P*-3*m*1	[37]

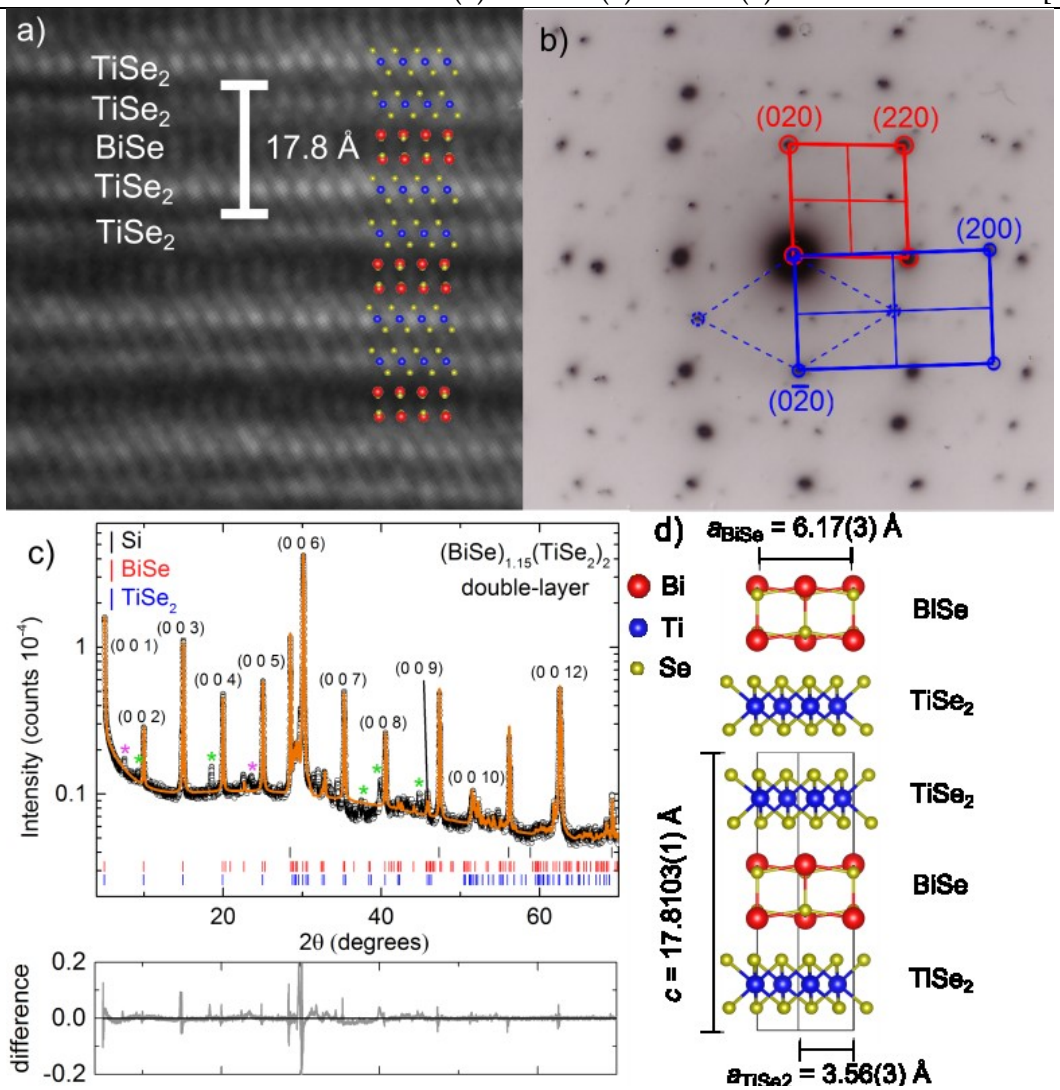

Figure 2.1: Structure of the double layer misfit compound $(BiSe)_{1.15}(TiSe_2)_2$. **a)** High resolution transmission electron microscopy (HRTEM) image oriented in the *a*-direction, demonstrating the stacking in the *c*-direction. The image is consistent with a double layer misfit in which double layers of $TiSe_2$ (blue and yellow atoms) are separated by BiSe (red and yellow) units (we are not assigning light or dark spots to specific atoms). **b)** Representative selected area electron diffraction (SAED) image with the unit cells of the two components illustrated. The triclinic unit cell for BiSe is shown in red while $TiSe_2$ is shown in blue. The standard hexagonal cell is shown as dashed blue lines, while the triclinic cell with two commensurate lattice parameters is shown as solid blue lines. **c)**

Powder X-ray diffraction (PXRD) pattern of ground single crystals, with Si as an internal standard. Major reflections [(0 0 *l*) peaks] are labeled. Fit line is shown in orange with the difference shown in grey below. Asterisks denote impurity phases Bi_2Se_3 (light green) and $(BiSe)_{1.13}(TiSe_2)$ (light magenta), present in trace amounts. **d)** Proposed structure viewed along the *b*-direction highlighting the incommensurate nature of the two layers.

A SAED pattern for the single layer $(BiSe)_{1.13}(TiSe_2)$, oriented along c*, is shown in Figure 2.2(a). As with the double layer compound, all observed reflections in the SAED pattern are indexable by a combination of a triclinic (pseudo-cubic) BiSe and a hexagonal $TiSe_2$ cell (the more commonly used triclinic misfit cell for $TiSe_2$ is also shown). A corresponding PXRD pattern is shown in Figure 2.2(b), with Si as an internal standard. Again (0 0 *l*) reflections are clearly visible, with the *h* or *k* reflections low in intensity and broad, as was seen for $(BiSe)_{1.15}(TiSe_2)_2$. Thus final *a* and *b* lattice parameters were determined using the same approach as for $(BiSe)_{1.15}(TiSe_2)_2$. Initially triclinic unit cells with *C*-1 symmetry were constructed using $(PbS)_{1.18}(TiS_2)$ [51] as a model (due to formulaic similarity). However, $(PbS)_{1.18}(TiS_2)$ has half the value of the *c*-axis lattice parameter, thus it was modified to be similar to $(PbS)_{1.12}(VS_2)$ [52]. The resulting lattice parameters are shown in Table 2.1 as compared to model misfit compounds. As with the double layer misfit, the cell angles α, *β*, and γ, although allowed to vary by space group symmetry, refined to 90° within <0.7% error, and thus were fixed at that value. A compound with nominal formula $BiTiSe_3$ was previously reported to have a *c*-axis lattice parameter of 11.84 Å.[48] The *c*-axis lattice parameter we find for $(BiSe)_{1.13}(TiSe_2)$ is twice this value, within 0.3%. This

good agreement suggests that "$BiTiSe_3$"[47,48] is in fact the single-layer misfit $(BiSe)_{1.13}(TiSe_2)$.

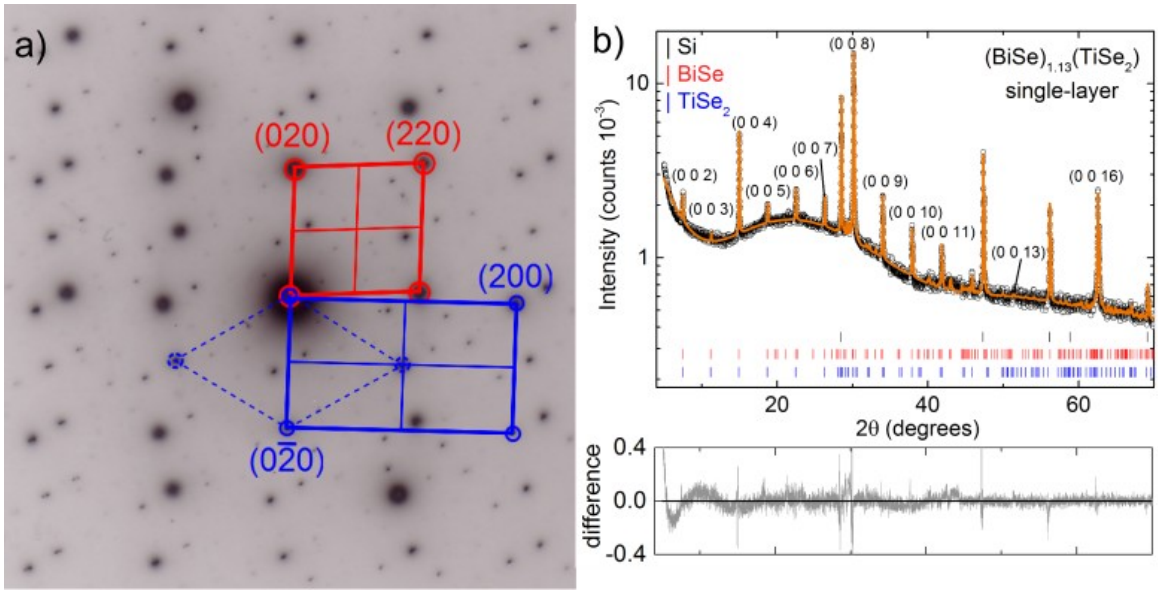

Figure 2.2: Structure of the single layer misfit compound $(BiSe)_{1.13}(TiSe_2)$. **a)** Representative selected image electron diffraction (SAED) image with the unit cells of the two components illustrated. The triclinic unit cell for BiSe is shown in red. The standard hexagonal $TiSe_2$ cell is shown as dashed blue lines, while the triclinic $TiSe_2$ cell with two commensurate lattice parameters is shown as solid blue lines. **b)** Powder X-ray diffraction (PXRD) pattern of ground single crystals, with Si as an internal standard. Major reflections [(0 0 *l*) peaks] are labeled. Fit line is shown in orange with the difference shown in grey below.

The two *a* lattice parameters determine the value of δ in $(MX)_{1+\delta}(TX_2)_n$ by the relation $\delta = (4/2)\ (a_2/a_1) - 1$.[8] Here a_1 is the *a*-axis for the MX layer and a_2 is the *a*-axis for the TX_2 layer. The values of δ calculated in this fashion are δ = 0.126(3) and δ = 0.154(7) for $(BiSe)_{1.13}(TiSe_2)$ and $(BiSe)_{1.15}(TiSe_2)_2$, respectively. These values are well within the range of 0.08-0.28 expected for misfit compounds[8].

The proposed structures for $(BiSe)_{1.13}(TiSe_2)$ and $(BiSe)_{1.15}(TiSe_2)_2$ are shown in Figure 2.3(a) and 3(b), respectively. Both consist of rock-salt type BiSe layers and hexagonal $TiSe_2$ layers separated by a Van der Waals gap, common to misfits[8]. The $TiSe_2$ layer has the same basic structure as one layer of bulk 1T-$TiSe_2$ which is the CdI_2 structure type (Figure 2.3(c)).[53] $(BiSe)_{1.13}(TiSe_2)$ has a BiSe:$TiSe_2$ ratio of 1.13:1 of each layer type while $(BiSe)_{1.15}(TiSe_2)_2$ has a $TiSe_2$ double layer with a ratio of 1.15:2 of each layer type. SAED patterns of the double layer compare well with that of $(PbSe)_{1.16}(TiSe_2)_2$ [28] as both observe only $h + k = 2n$ reflections. These systematic absences and similar lattice parameters suggests the two misfits, $(BiSe)_{1.15}(TiSe_2)_2$ and $(PbSe)_{1.16}(TiSe_2)_2$, are isomorphic. The lattice parameters vary slightly, but this is expected due to differing atomic radii. $(BiSe)_{1.15}(TiSe_2)_2$ is also likely isomorphic to $(LaSe)_{1.20}(TiSe_2)_2$ given the similar stoichiometry and lattice parameters. Similarly, the single layer is likely isomorphic with $(PbS)_{1.12}(VS_2)$ due to similar stoichiometry, lattice parameters, and systematic absences in the SAED data[52]. One distinction between our results and previous studies on $(PbS)_{1.12}(VS_2)$ [52] and $(LaSe)_{1.20}(TiSe_2)_2$[27] is that we find none of the angles (instead of one and two respectively by >1%) of the triclinic cell deviates from 90°, within <0.7% error. This suggests that the actual symmetry is higher than *C*-1, although our data is not sufficient to unambiguously resolve this detail.

2.3.2 Physical Properties

Temperature-dependent resistivity for $(BiSe)_{1.13}(TiSe_2)$ (ρ_{300} = 0.5609(6) mΩ*cm), $(BiSe)_{1.15}(TiSe_2)_2$ (ρ_{300} = 3.07(3) mΩ*cm), and 1T-$TiSe_2$ (ρ_{300} = 15.63(2) mΩ*cm) are shown in Figure 2.4. $(BiSe)_{1.13}(TiSe_2)$ and $(BiSe)_{1.15}(TiSe_2)_2$ exhibit metallic behavior over the entire temperature range 1.8 < T < 300 K. A broad feature is seen in the resistivity of 1T-$TiSe_2$ due to the onset of a charge density wave (CDW)[18–21] as previously reported[29–32]. This feature is not observed in either misfit, suggesting that a CDW is not present in single or double layer misfit $TiSe_2$. Further evidence for the lack of a CDW transition in $(BiSe)_{1.15}(TiSe_2)_2$ is that there are no anomalies in the magnetic susceptibility from 1.8 to 300 K (not shown).

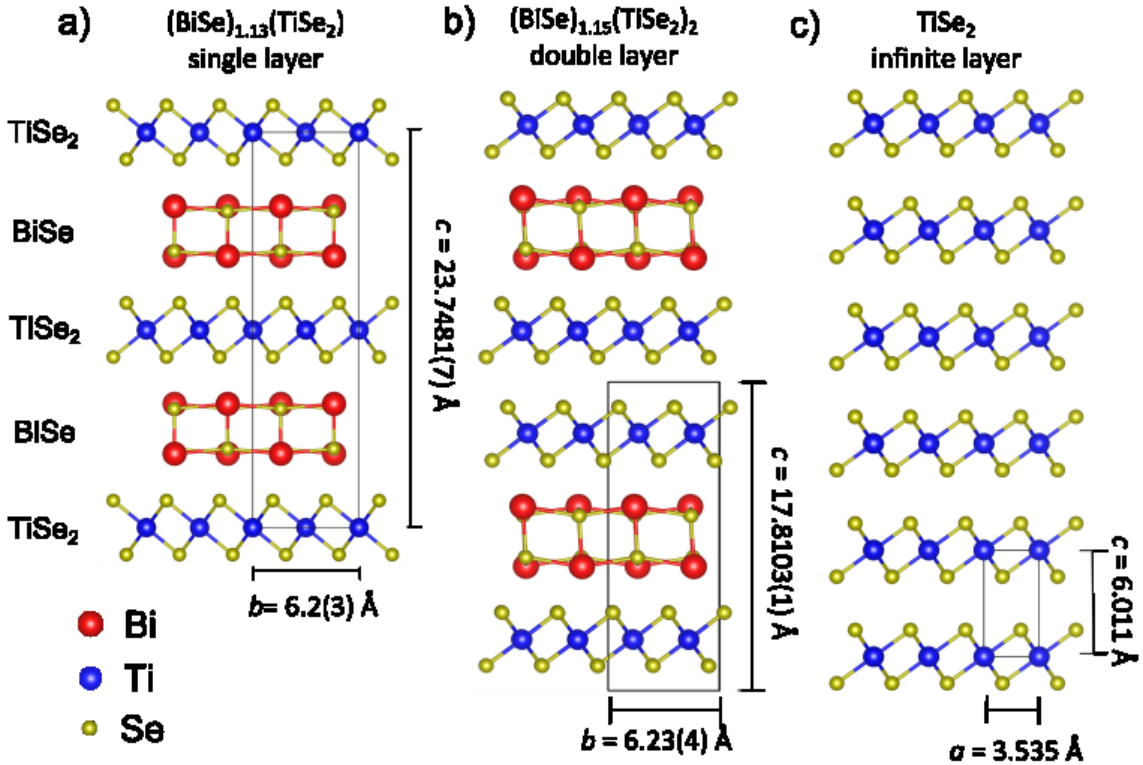

Figure 2.3: a) Proposed structure for single layer misfit $(BiSe)_{1.13}(TiSe_2)$ in the *a*-direction. The triclinic unit cell with two commensurate lattice parameters is

shown. **b)** Proposed structure for the double layer misfit $(BiSe)_{1.15}(TiSe_2)_2$ in the *a*-direction. The triclinic unit cell with two commensurate lattice parameters is shown. **c)** Known structure for 1T-$TiSe_2$,[54] shown as the end member of the series $(MSe)_{1+\delta}(TiSe_2)_n$ with n = infinity.

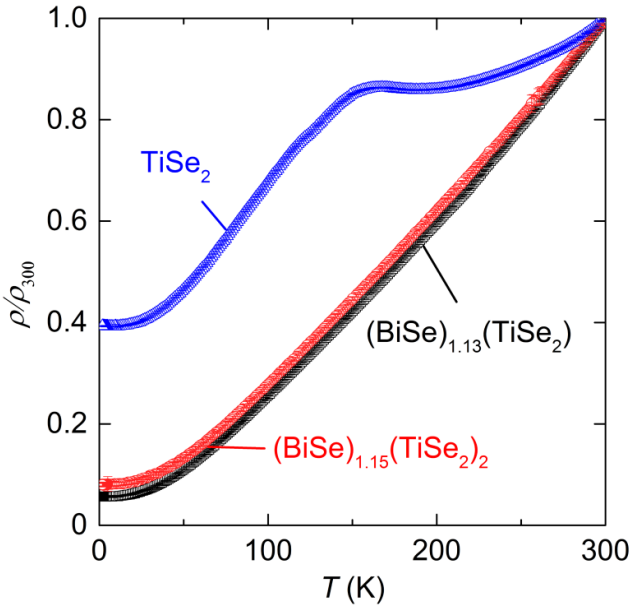

Figure 2.4: Temperature-dependent resistivity for $(BiSe)_{1.13}(TiSe_2)$ (black), $(BiSe)_{1.15}(TiSe_2)_2$ (red), and bulk 1T-$TiSe_2$ (blue) measured on single crystals with current applied in the *ab* plane. The broad feature around 160 K in 1T-$TiSe_2$ is due to the formation of the CDW,[29–32] which is absent in both misfit compounds.

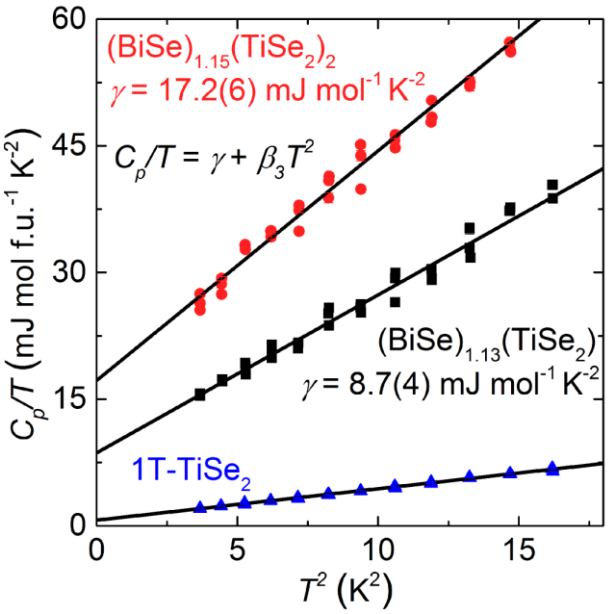

Figure 2.5: Specific heat for $(BiSe)_{1.13}(TiSe_2)$ (squares), $(BiSe)_{1.15}(TiSe_2)_2$ (circles), and bulk 1T-$TiSe_2$ (triangles) measured on single crystals. Fits to the equation $C_p/T = \gamma + \beta_3 T^2$ are shown demonstrating the electronic (γ) and lattice (β_3)

contributions to specific heat. The electronic contribution doubles when the number of $TiSe_2$ layers doubles from $(BiSe)_{1.13}(TiSe_2)$ to $(BiSe)_{1.15}(TiSe_2)_2$ indicating that the $TiSe_2$ layers are electronically active in these misfit compounds.

Heat capacity measurements are consistent with the observed resistivity. Figure 2.5 shows the low temperature portion of the heat capacity for $(BiSe)_{1.13}(TiSe_2)$, $(BiSe)_{1.15}(TiSe_2)_2$, and $TiSe_2$ plotted as C_p/T vs T^2. This isolates the electronic (γ, Sommerfeld coefficient) and lattice (β_3) contributions to specific heat, as $C_p/T = \gamma + \beta_3 T^2$ at sufficiently low temperatures.[2] The electronic contribution doubles as the number of $TiSe_2$ layers doubles, from $(BiSe)_{1.13}(TiSe_2)$ (γ = 8.7(4) mJ mol^{-1} K^{-2}) to $(BiSe)_{1.15}(TiSe_2)_2$ (γ = 17.2(6) mJ mol^{-1} K^{-2}). This implies that the $TiSe_2$ layers are electronically active, rather than the BiSe layer. This is consistent with previous assumptions in the literature, as misfits with single or double TiS_2 layers show metallic behavior.[8,55] These results also provide further evidence that there is no CDW in either the single or double layer misfit above T = 1.8 K: in contrast to the misfits studied here, bulk 1T-$TiSe_2$ has a near zero Sommerfeld coefficient due to the almost complete gapping out of electronic states by the CDW.

At the same time, the doubling of the electronic contribution to the specific heat upon doubling the number of $TiSe_2$ layers is unexpected from an electron count perspective. Based on known normal oxidation states, the formal total oxidation state of the BiSe layer should be $[BiSe]^{1+}$ in both the single and double-layer misfit, whereas the $TiSe_2$ layers would have formal charges of

$[TiSe_2]^{1-}$ (single layer) and $[TiSe_2]^{0.5-}$ (double layer). While the charge per $TiSe_2$ layer changes, the total charge transferred to the $TiSe_2$ layer(s) per formula unit should be the same in both the single and double layer compound. If one assumes no substantial change in effective mass of the charge carriers, this would give rise to nearly identical electronic specific heat contributions, far from the doubling that is actually observed. The most probable explanation of our data is that the effective carrier mass doubles when the band filling per $TiSe_2$ layer is reduced from $1e^-/TiSe_2$ to $0.5e^-/TiSe_2$. DFT LDA calculations on 1T-$TiSe_2$ do predict an increase in effective mass, but the magnitude of the predicted change yields a ratio of Sommerfeld coefficients of only 1.2(1) for $[(TiSe_2)_2]^{1-}/[TiSe_2]^{1-}$.[56] This 20% increase is significantly less than the doubling observed, which may indicate the importance of electron-electron correlations not included at the LDA level in DFT. However, other explanations, such as a change in the degree of charge transfer between the two layer types or a different number of defects of some kind (e.g. Se vacancies), cannot be ruled out.

The lattice contributions to the specific heat are explored in a plot of C_p/T^3 vs T shown in Figure 2.6, normalized per $TiSe_2$ layer. Such a plot is useful because at sufficiently low temperatures Debye modes plateau at a constant value, while Einstein modes follow a peaked, exponential behavior.[2] Einstein modes account for non-dispersing phonon modes while Debye contributions better describe strongly dispersing modes. Their characteristic temperatures are

given as $\theta_x = \hbar\omega_x/k_B$ where $\hbar$ is Planck's constant, k_B is the Boltzmann constant, and ω_x is the characteristic frequency (X = D or E for Debye or Einstein).[2] The best fits are obtained using a combination of two Debye modes and a single Einstein mode. The upturns at $T < 5$ K in all data sets are attributed to the electronic contributions. The most prominent difference between the data sets is a significantly larger lattice contribution at $T \leq 50$ K in both misfit compounds. The BiSe layers are responsible for a portion of this added lattice specific heat, but there is also a significant additional contribution from the $TiSe_2$ layers. In particular, the Einstein mode at $\theta_E \sim 45$ K (in all three compounds) likely originates in the $TiSe_2$ layers as it is present in bulk 1T-$TiSe_2$. Further, normalizing per $TiSe_2$ layer, the single and double layer compounds are seen to have the same oscillator strength (representative of the same number of atoms). The fact that the total phonon contribution increases as the amount of BiSe increases is due to the total contribution scaling per amount of atoms. If the Einstein mode arose from the BiSe layers it would be expected to have half the oscillator strength in the double layer compound when normalized per $TiSe_2$ layer. Instead the oscillator strength of the Einstein mode remains constant as the amount of BiSe increases, and the oscillator strengths of the Debye modes increases (not shown) to account for the increasing total phonon contribution. The oscillator strength of the $\theta_E \sim 45$ K mode is also significantly suppressed in 1T-$TiSe_2$. This implies that it is low energy excitation of $TiSe_2$ when the CDW is not present. We thus tentatively assign this Einstein mode to the optic phonon

that softens in bulk 1T-$TiSe_2$ when the CDW forms.[41,43,57,58] Put another way, our results show that when the CDW state is not the ground state in $TiSe_2$, it is instead a low energy excited state.

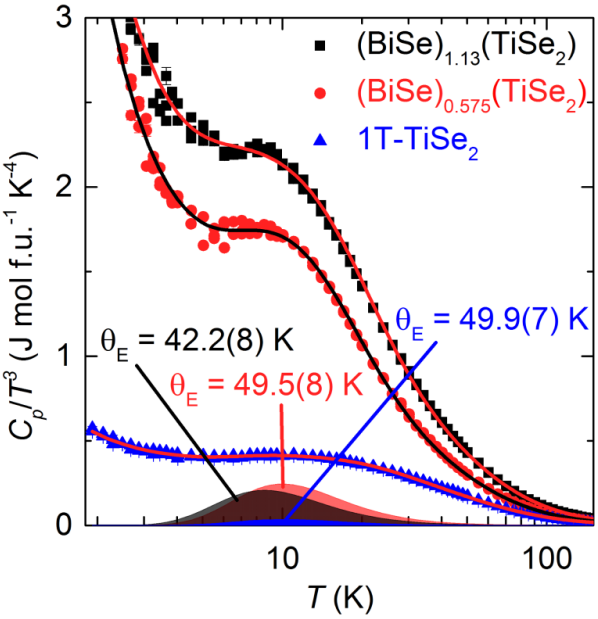

Figure 2.6: Specific heat for $(BiSe)_{1.13}(TiSe_2)$, $(BiSe)_{1.15}(TiSe_2)_2$ [$(BiSe)_{0.575}(TiSe_2)$], and bulk 1T-$TiSe_2$ plotted as C_p/T^3 vs T to isolate various phonon contributions, and normalized per $TiSe_2$ layer. The fit lines (red and black) are shown with two Debye modes, one Einstein ($\theta_E = \hbar\omega_x/k_BT$) mode, and an electronic contribution. Plot is scaled per formula unit (f.u.) with $(BiSe)_{1.15}(TiSe_2)_2$ scaled by half for direct comparison of the Einstein modes. Though the characteristic Einstein temperature is similar for each compound, the spectral weight significantly decreases for bulk 1T-$TiSe_2$.

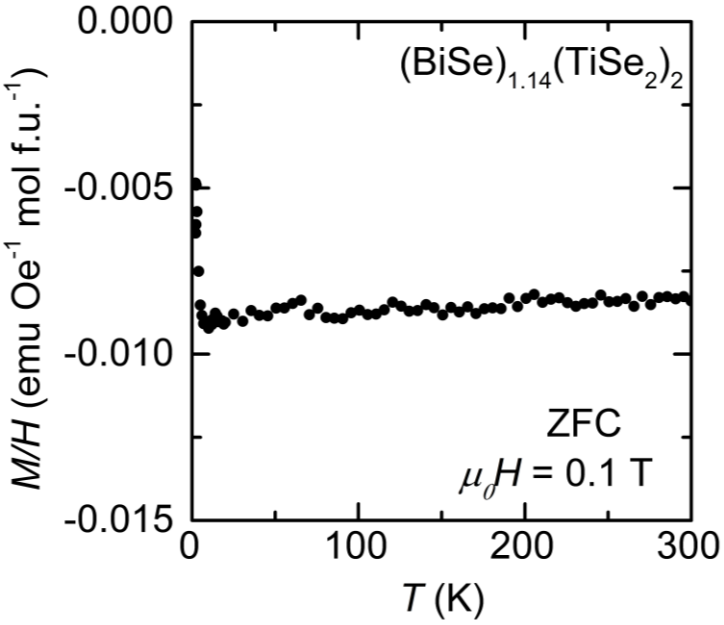

Figure 2.7: Magnetization of $(BiSe)_{1.14}(TiSe_2)_2$ with an applied field of 0.1 T. A Curie tail is seen at $T < 10$ K.

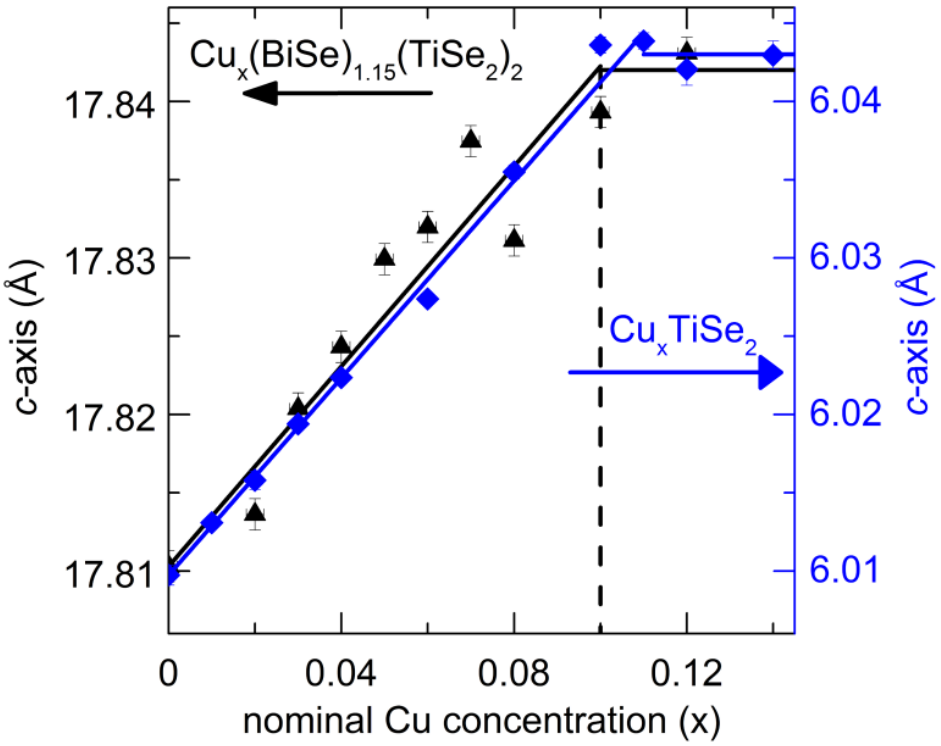

Figure 2.8: Change in *c*-axis as $(BiSe)_{1.15}(TiSe_2)_2$ is intercalated with Cu (triangles), compared to the same data for Cu_xTiSe_2 from Ref. [16] (diamonds). Upon intercalation past x = 0.10, additional phases were present in $Cu_x(BiSe)_{1.15}(TiSe_2)_2$,

indicative of a solid solubility limit shown as a dashed line. Solid lines are guides to the eye.

Magnetization measurements on $(BiSe)_{1.14}(TiSe_2)_2$, shown in Figure 2.7, demonstrate purely diamagnetic behavior. The negative response is constant until T ~ 10 K where a Curie tail appears. The diamagnetic response confirms insulating behavior in this material. The Curie tail is due to impurities in the material, either from other phases, such as Bi_2Se_3 or $TiSe_2$, or from Se vacancies in $(BiSe)_{1.14}(TiSe_2)_2$.

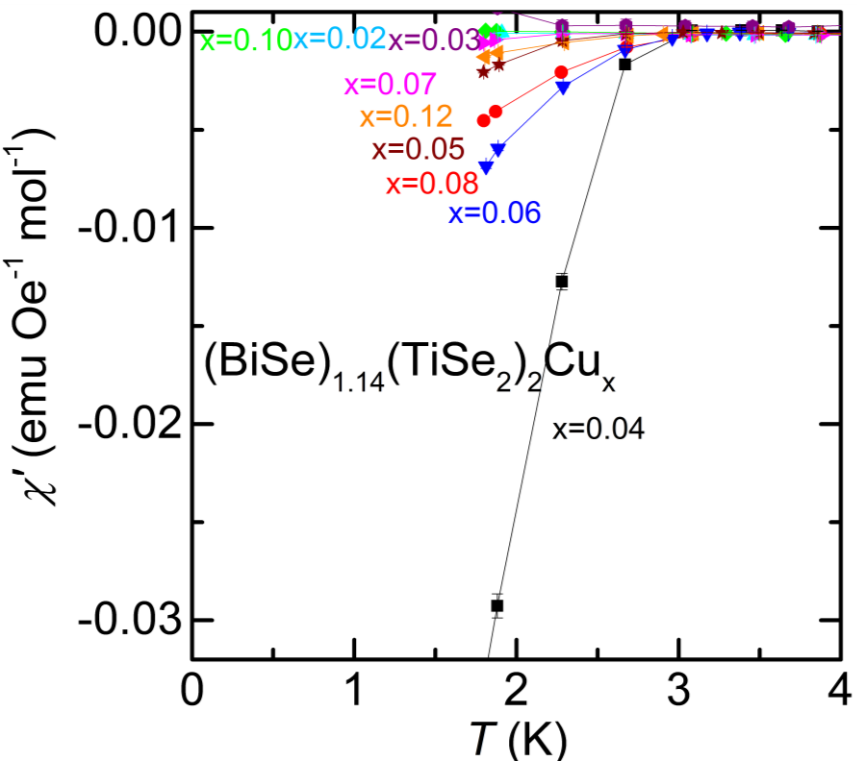

Figure 2.9: AC magnetization on $(BiSe)_{1.14}(TiSe_2)_2Cu_x$ for x = 0.02, 0.03, 0.04, 0.05, 0.06, 0.07, 0.08, 0.10, and 0.12 shown as cyan triangles, purple pentagons, black squares, burgundy stars, upside-down blue triangles, right-facing pink triangles, red circles, green diamonds, and left-facing orange triangles respectively. All samples were measured with an applied field of $\mu_0 H$ = 0.001 T. χ' represents the in-plane magnetization of the sample.

2.3.3. The Effect of Intercalation: $Cu_x(BiSe)_{1.15}(TiSe_2)_2$

There is a systematic change in *c*-axis lattice parameter for $(BiSe)_{1.15}(TiSe_2)_2$ on intercalation with Cu ($Cu_x(BiSe)_{1.15}(TiSe_2)_2$), shown in Figure 2.8. (reported values for x are the nominal compositions.) The solid solution limit is x = 0.10, as evidenced by an increase in the quantity of impurity phases, and the leveling off of the *c*-axis lattice parameter, at that concentration. The magnitude of the *c*-axis increase matches very well the expansion observed in Cu_xTiSe_2. This suggests that Cu is going in the Van der Waals gap between layers, rather than substituting for another element in each layer. Further evidence that Cu is between the $TiSe_2$ double layers in $(BiSe)_{1.15}(TiSe_2)_2$ is that the addition of Cu to a melt leads to significantly more double layer misfit. This is the case whether targeting $(BiSe)_{1.13}(TiSe_2)$ or $(BiSe)_{1.15}(TiSe_2)_2$, indicating that Cu assists in the formation of a double $TiSe_2$ layer. This demonstrates that Cu indeed sits in the Van der Waals gap between $TiSe_2$ layers as in bulk Cu_xTiSe_2[16].

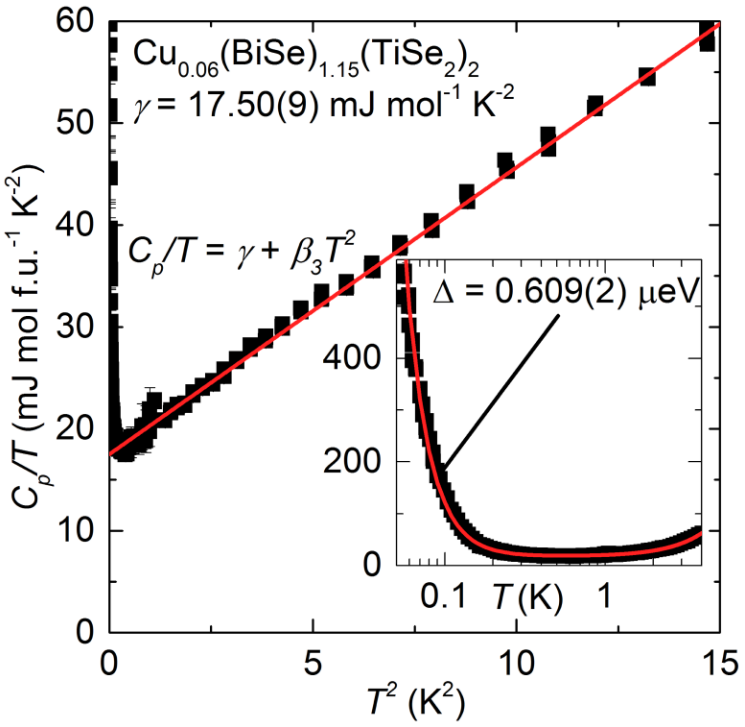

Figure 2.10: Low temperature specific heat of $Cu_{0.06}(BiSe)_{1.15}(TiSe_2)_2$. The fit line (red) includes electronic (γ) and lattice (β_3) contributions. No lambda anomaly is seen down to T = 50 mK. The inset highlights the high temperature tail of a Schottky anomaly with a gap of Δ = 0.609(2) μeV, corresponding to ordering of Bi nuclear spins.[59] The fit values of the heat capacity are in good agreement with the data collected separately above 1.8 K (Figure 2.5).

All intercalation levels were tested for superconductivity using magnetization. A variety of $Cu_x(BiSe)_{1.15}(TiSe_2)_2$ compounds had a diamagnetic response around x = 0.06, with an onset of T ~ 3 K. However, AC magnetization shows that the magnitude was at most 5% of that expected for a bulk superconductor (Figure 2.9). Likewise the magnetic response appears too gradual to be from the bulk. To better confirm that the response was due to small amounts of Cu_xTiSe_2 impurities rather than the intercalated misfit, heat capacity measurements of x = 0.06, were performed down to T = 50 mK. The data is shown in Figure 2.10. No lambda anomaly is seen, indicating that

$Cu_x(BiSe)_{1.15}(TiSe_2)_2$ is not a superconductor down to T = 50 mK. The small feature at T = 1 K is due to superfluid ^{4}He increasing the wire thermal conductivity to the sample stage. The inset highlights a nuclear Schottky anomaly, seen at lower temperatures with a gap of Δ = 0.609(2) μeV. This likely arises from RKKY exchange interactions of the Bi nuclei and the conduction electrons, as is well-known to occur.[59] The plot of C_p/T vs. T^2 for $Cu_{0.06}(BiSe)_{1.15}(TiSe_2)_2$ also provides a check of the electronic and lattice contributions of specific heat, as the addition of $Cu_{0.06}$ should only have a small contribution. Hence these contributions are expected to be close to that of $(BiSe)_{1.15}(TiSe_2)_2$, which is indeed the case here.

2.4 Conclusion

The basic structures of the misfit compounds $(BiSe)_{1.13}(TiSe_2)$ and $(BiSe)_{1.15}(TiSe_2)_2$ are reported. The *c*-axis parameter for $(BiSe)_{1.13}(TiSe_2)$ is within 0.3% of twice the value previously reported for $BiTiSe_3$[48] suggesting that $(BiSe)_{1.13}(TiSe_2)$ is the actual formula of "$BiTiSe_3$".

Structurally, $(BiSe)_{1.13}(TiSe_2)$ and $(BiSe)_{1.15}(TiSe_2)_2$ appear isomorphic to $(PbS)_{1.12}(VS_2)$ and $(LaSe)_{1.20}(TiSe_2)_2$ respectively. Atomic positions within the unit cell and absolute space group assignments (including whether or not the triclinic angles are in fact 90°) require single crystals of sufficient quality for higher dimensional crystallography.

Unlike bulk 1T-$TiSe_2$, no CDW formation is observed above T = 1.8 K for either misfit. This likely reflects a combination of the reduced dimensionality, as the CDW in 1T-$TiSe_2$ has a three dimensional wavevector (k = (1/2,1/2,1/2)) which might be chiral[29–34], and changes in the charge transferred to the $TiSe_2$ motifs. It is hypothesized that the emergence of a CDW can still be seen by further increasing n in $(BiSe)_{1+\delta}(TiSe_2)_n$. This claim is reinforced by the Einstein mode, shown to be directly related to $TiSe_2$ in the misfit compounds, which has the same characteristic temperature of 1T-$TiSe_2$. At some value of n the oscillator strength or characteristic temperature of this mode should begin to decrease, as it does for bulk 1T-$TiSe_2$, representing the onset of the CDW.

Intercalation with Cu was not sufficient to induce superconductivity above T = 50 mK in $(BiSe)_{1.15}(TiSe_2)_2$ unlike in the parent compound 1T-$TiSe_2$. This is not surprising if proximity to a CDW is a necessary ingredient for superconductivity in Cu_xTiSe_2, as previously hypothesized[16]. This may alternately reflect the total quantity of formal charge transferred to the $TiSe_2$ layers, as the structurally similar double layer compound $(PbSe)_{1.16}(TiSe_2)_2$ is known to superconduct at T_c = 2.3 K[28].

More generally, our results highlight how systematic control of layering 'inert' and 'active' layers can be used to elucidate the origins and mechanism of a variety of useful physical phenomena.

2.5 Acknowledgements

This work was supported by Johns Hopkins University Startup funds and by NSF, Division of Materials Research (DMR), Solid State Chemistry (SSMC), CAREER grant under Award DMR-1253562. Use of Dilution Refrigerator funded by National Science Foundation Major Research Instrumentation Program under NSF DMR-0821005. B.A.T. also acknowledges useful discussions with J.R. Neilson.

3. Anion-Anion Bonding and Topology in Ternary Iridium Seleno-Stannides

This work was co-written with the following authors and is published under the following citation:

Inorganic Chemistry **54**, 11993-12001 (2015)

http://dx.doi.org/10.1021/acs.inorgchem.5b02387

Benjamin A. Trump*[,a,b] Jake A. Tutmaher,[b,c] Tyrel M. McQueen[a,b,c,d]

[a]Department of Chemistry, Johns Hopkins University, Baltimore, Maryland 21218, United States

[b]Institute for Quantum Matter, Johns Hopkins University, Baltimore, Maryland 21218, United States

[c]Department of Physics and Astronomy, Johns Hopkins University, Baltimore, Maryland 21218, United States

[d]Department of Material Science, Johns Hopkins University, Baltimore, Maryland 21218, United States

3.1 Introduction

Homologous series offer a promising opportunity for growth and design of new materials.[17] The series M_xTCh is one such example, where M is a late transition metal (Fe, Co, Ni, Ru, Pd, Ir, or Pt), T is a later Group 14 or 15 element (Ge, Sn, Pb, As, Sb, or Bi), Ch = S, Se, or Te, and $x = 3/2$, 1, or 2/3. This series is noteworthy due to the large variety of structures that exist depending on the value of x and the elements involved. These structures consist of a variety of corner- or edge-sharing MT_3Ch_3 octahedra (such as FeS_2 - pyrite) though the space groups vary wildly due to the ordering (or lack thereof) for T and Ch. Recent studies predict a possibility of more than eight different space groups for the simple case of $x = 1$.[60,61] When $x = 2/3$ the skutterudite structures are commonly formed, which are of interest as promising thermoelectric materials due to their low thermal conductivity.[62,63] When $x = 3/2$ another competing phase, half antiperovskites, are formed.[64] The structure of M_xTCh depends on temperature, pressure, stoichiometry, and most notably - the transition metal itself.

Though such compounds of all of the various transition metals are structurally interesting due to anion-anion bonding, 5*d* transition metals have recently attracted significant interest due to strong relativistic effects (spin-orbit coupling) which could lead to non-trivial behavior.[65] These relativistic effects have comparable energy scales with crystal field stabilization and electron

correlations, which could lead to magnetic frustration or possible spin liquid behavior.[66–68]

Iridium in particular has been heavily studied for these reasons, with a majority of works focusing on oxides.[69–74] Additionally, several studies were conducted on iridium chalcogenides, namely Ir_xCh_2 (*Ch* = S, Se, or Te). Initial reports focused on structural details, as all of these compounds contain anion-anion bonding, and IrS_2, $IrSe_2$, and $IrTe_2$ can form three different structure types.[75–78] More recent investigations have been on superconductivity in both the pyrite-type Ir_xTe_2 (x = 0.75)[79] and doped CdI_2-type $Ir_{1-x}M_xTe_2$ (M = Pd or Pt)[80–83]. Though these studies are comprehensive, none have yet thoroughly looked at the possible stoichiometries of ternary iridium chalcogenides.

Here we report the synthesis, structure, and physical properties of the pyrite phase $IrSn_{0.45}Se_{1.55}$, the skutterudite phase $Ir_2Sn_3Se_3$, and the structurally distinct Ir_2SnSe_5. $Ir_2Sn_3Se_3$ has been previously reported[62,84], though we expand the physical properties. To the authors' knowledge, neither $IrSn_{0.45}Se_{1.55}$ or Ir_2SnSe_5 have been previously reported. We find that all three exhibit insulating and diamagnetic behavior, indicative of low spin $5d^6$ Ir^{3+}. Each compound also displays a variation of Sn-Se bonding, as $IrSn_{0.45}Se_{1.55}$ contains Sn-Se dimers, $Ir_2Sn_3Se_3$ contains $(Sn\text{-}Se)_2$ tetramers, and Ir_2SnSe_5 contains $(Sn\text{-}Se)_n$ polymeric chains. Further, band structure calculations demonstrate that $Ir_2Sn_3Se_3$ is a single-

band *p*-type semiconductor and imply that it becomes topologically non-trivial under tensile strain due to an inversion of Se-*p* and Ir-*d* states.

3.2 Experimental

3.2.1 Materials

Powders were grown by placing Ir (Alfa Aesar 99.95%), Sn (Noah Technologies 99.9%), and Se (Alfa Aesar 99.999%), in stoichiometric ratios, in a fused silica tube. All tubes were filled with 1/3 atm of Ar to minimize vaporization of Sn and Se. Each tube was heated quickly to 500°C, followed by a 50°C per hour ramp to an annealing temperature at which the samples were held for four days, before being furnace cooled. The resulting boule was pulverized, pressed into a pellet, and heated at the same annealing temperature for four days, and furnace cooled again. Each resulted in a ~300 mg gray, sintered pellet which was used for all physical property and characterization methods. $Ir_2Sn_3Se_3$ was annealed at 750°C, while Ir_2SnSe_5 was annealed at 780°C. Later inspection indicated the presence of ~1.75 wt% $IrSe_2$ in Ir_2SnSe_5.

$IrSn_{0.45}Se_{1.55}$ was annealed at 950°C, and was quenched in water after each heat treatment. Targeting a 0.05 change in molar ratio resulted in significant impurities (> 10 wt%) of $IrSe_2$ or $Ir_2Sn_3Se_3$. After the second heating an Ir metal impurity around 0.15 wt% was seen which increased upon further heat

treatments. The resulting pellet from $IrSn_{0.45}Se_{1.55}$ was cold-pressed rather than sintered.

3.2.2 Characterization Methods

Laboratory powder X-ray diffraction (PXRD) patterns were collected using Cu K_α (λ_{avg} = 1.5418 Å) on a Bruker D8 Focus diffractometer with LynxEye detector. Lebail refinements were used for phase identification and starting lattice parameters in TOPAS (Bruker AXS). Simulated annealing was then used for initial atomic positions, with Rietveld refinements for final atomic positions and lattice parameters, both in TOPAS. Synchrotron PXRD was collected on the high resolution 11-BM-B diffractometer at the Advanced Photon Source, Argonne National Laboratory, with an incident wavelength of λ = 0.41385 Å for $Ir_2Sn_3Se_3$ and λ = 0.41388 Å for Ir_2SnSe_5. Silicon was used as an internal standard for both laboratory and synchrotron PXRD; additionally 50 wt% amorphous SiO_2 was added to synchrotron samples to minimize absorption effects. To verify choice of lattice parameters and space group, transmission electron microscopy (TEM) was used, with a Phillips CM300 atomic resolution TEM, equipped with a Field Emission Gun with an accelerating voltage of 300 kV. For $Ir_2Sn_3Se_3$ selected area electron diffraction (SAED), collected on film (Kodak SO 163), was used to check for additional ordering. For Ir_2SnSe_5 SAED, collected both on film and with a CCD camera (bottom mounted Orius camera), was used to initially determine the unit cell. Structures were visualized using VESTA.[50]

Physical properties (electronic, heat capacity, thermal transport, and magnetization) data were collected on pellets in a Physical Properties Measurement System (PPMS, Quantum Design). All measurements were conducted from T = 1.8 K to T = 300 K. Resistivity of $Ir_2Sn_3Se_3$ was also measured down to T = 70 mK on a PPMS equipped with a dilution refrigerator. All resistivity measurements used standard four-probe geometry. Heat capacities were measured using the semi-adiabatic pulse technique, with three repetitions at each temperature. Magnetic susceptibilities were measured with a $\mu_0 H$ = 1 T.

3.2.3 Calculation Methods

Electronic and band structure calculations were performed on $Ir_2Sn_3Se_3$, using density functional theory (DFT) with the local density approximation (LDA) utilizing the ELK all electron full-potential linearized augmented-plane wave plus local orbitals (FP-LAPW+LO) code.[85] Calculations were conducted both with and without spin-orbit coupling (SOC) using a 4 x 4 x 4 k-mesh, with the experimental unit cell. Parity analysis on the time-reversal invariant momentum (TRIM) points for Z_2 values[86] were conducted by fitting the eigenvectors computed from ELK to a set of maximally-localized Wannier functions (MLWF, using Wannier90 software package[87]). The calculation on $Ir_2Sn_3Se_3$ under tensile strain was conducted using spin-orbit coupling and a unit cell increased uniformly by 0.6 Å. The band structures were independently verified using the Vienna Ab Initio Simulation Package (VASP)[88–90], and the topological indices

were alternatively calculated using MLWFs generated by Wannier90 in tandem with the Z2Pack software[91,92].

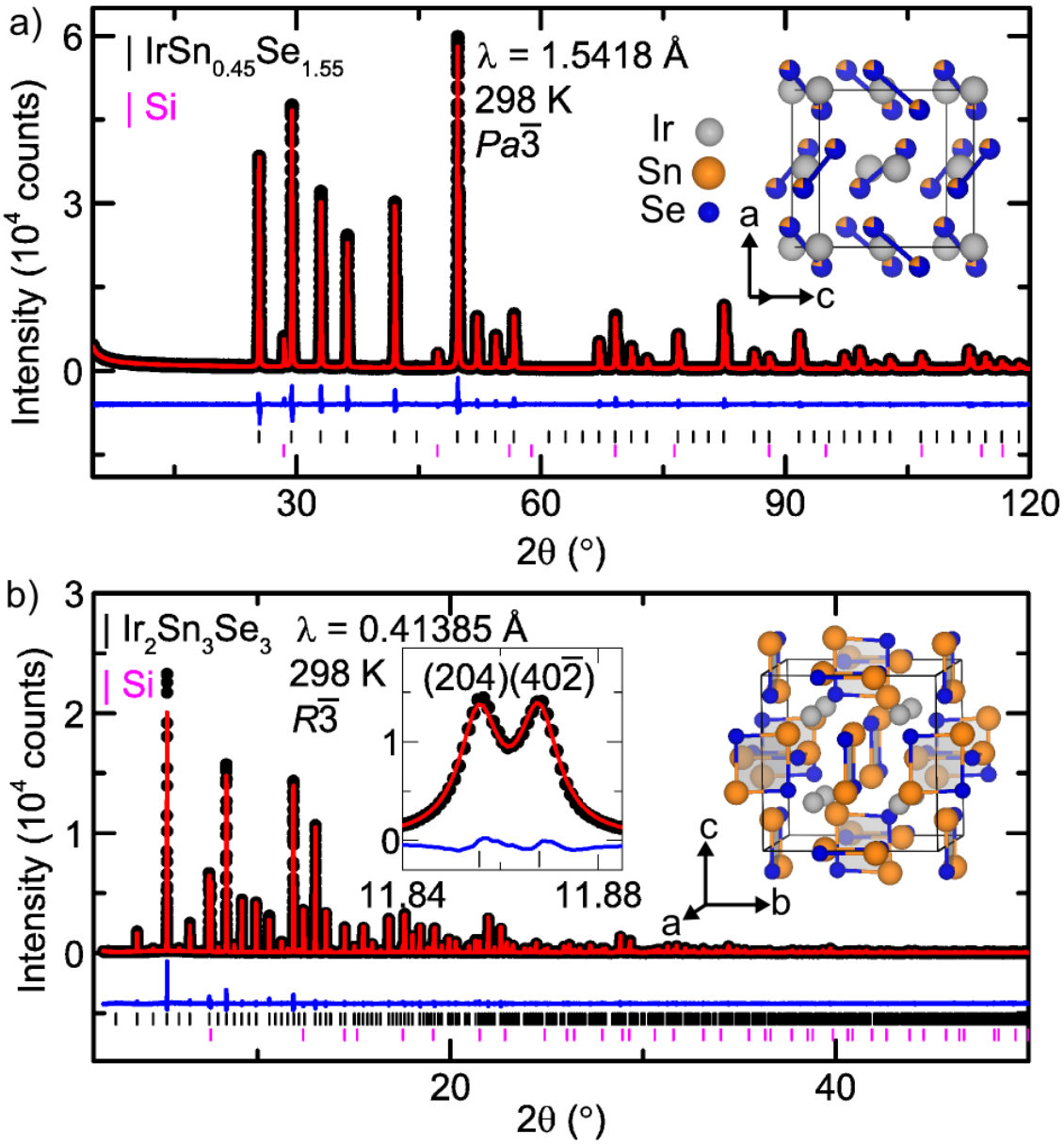

Figure 3.1: a) Rietveld refinement of laboratory powder X-ray data for IrSn0.45Se1.55 with internal Si standard. Structure is shown in the inset, which models Sn (orange slices) randomly mixed on the Se sites. **b)** Rietveld refinement of synchrotron powder X-ray data for $Ir_2Sn_3Se_3$ with internal Si standard. Insets show (left) subtle splitting of peaks and (right) $Ir_2Sn_3Se_3$ shown as Sn_2Se_2 tetramers. Experimental data shown as black circles, fit is in red, with the difference in blue. Ir is shown in grey, Sn in orange, and Se in blue.

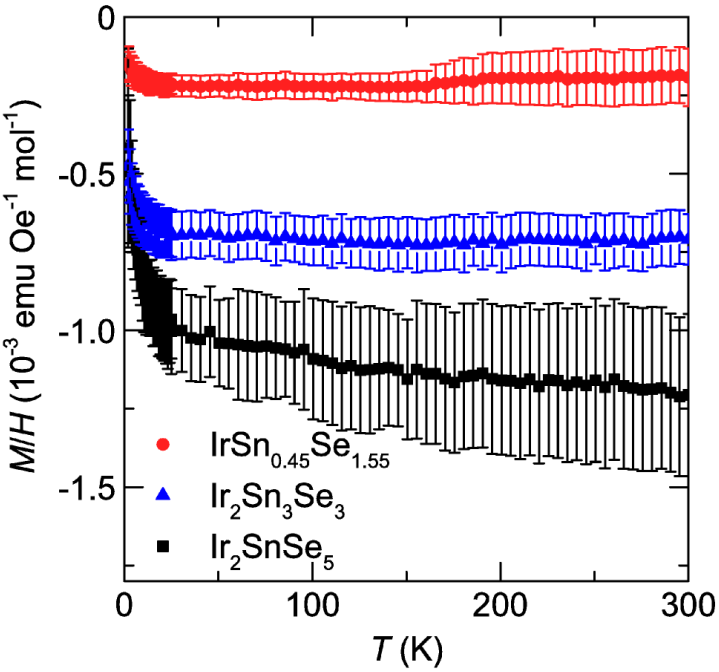

Figure 3.2: Magnetization versus temperature for $IrSn_{0.45}Se_{1.55}$ (red circles), $Ir_2Sn_3Se_3$ (blue triangles), and Ir_2SnSe_5 (black squares).

3.3 Results and Discussion

3.3.1 Structure of $IrSn_{0.45}Se_{1.55}$.

Room temperature laboratory PXRD data for $IrSn_{0.45}Se_{1.55}$ is shown in Figure 3.1a. Refinements were conducted with space group $Pa\bar{3}$, the model structure is shown in the inset of Figure 3.1a. Crystallographic parameters are in Table 3.1. The structure type is identical to the pyrite FeS_2[93], with tilted, corner-sharing IrX_6 octahedra, and Se-Se dimers on each corner, with Sn randomly distributed over the Se sites. Similar compounds such as cobaltite CoAsS[94] or ullmannite NiSbS[95] show anion ordering leading to a lower symmetries of $Pca2_1$ and $P2_13$ respectively. Ordering in these compounds is justified due to the observation of the (010) reflection for ullmannite and additionally the (110) reflection for

cobaltite.[94] However, PXRD for $IrSn_{0.45}Se_{1.55}$ does not show the evidence of either of these reflections despite as much as 55,000 counts for peaks, and a strip detector with a high signal to noise ratio. This defends the choice of space group $P\bar{a}3$. Furthermore, attempts to refine occupancies led to values within 1% of nominal stoichiometry for $IrSn_{0.45}Se_{1.55}$.

Table 3.1: Crystallographic parameters for $IrSn_{0.45}Se_{1.55}$ using $Pa\bar{3}$ (205) obtained from Rietveld refinements to laboratory powder diffraction data at room temperature. Atomic positions are restricted by symmetry as Ir: 4*a* (0, 0, 0) and Sn/Se: 8*c* (*x*, *x*, *x*). Occupancies were fixed at nominal values and errors reported are from statistical uncertainties.

	λ (Å)	1.5418
	a=*b*=*c* (Å)	6.074419(4)
	V (Å^3)	224.1374(5)
	U_{iso}	
Ir	(Å^2)	0.00793(5)
	x	0.37629(4)
Sn/Se	occ	0.225/0.775
	U_{iso} (Å^2)	0.00488(8)
	R_{wp}	5.534
	R_p	4.157
	R_F^2	2.964
	χ^2	1.867

$$R_{wp} = \sqrt{\frac{\sum|Y_{o,m}-Y_{c,m}|}{\sum Y_{o,m}}} \qquad R_p = \sqrt{\frac{\sum w_m(Y_{o,m}-Y_{c,m})^2}{\sum w_m Y_{o,m}^2}}$$

$$R_{exp} = \sqrt{\frac{\sum M-P}{\sum w_m Y_{o,m}^2}} \qquad \text{GoF} = \chi^2 = \sqrt{\frac{\sum w_m(Y_{o,m}-Y_{c,m})^2}{M-P}}$$

The composition of $IrSn_{0.45}Se_{1.55}$ is very close to that of Ir_2SnSe_3. Given the samples are diamagnetic (see Figure 3.2), and thus Ir is in the 3+ oxidation state, this implies a mixture of Sn-Se and Se-Se, i.e. $Ir^{3+}{}_2(SnSe)^{4-}(Se_2)^{2-}$, but with a slight

excess of Se-Se dimers. This off stoichiometry would then imply electron counting closer to $Ir^{2.9+}_2(Sn_{0.9}Se_{1.1})^{3.8-}(Se_2)^{2-}$. Further work is needed to understand how the excess electrons are accommodated. This deviation from "perfect" stoichiometry is an explanation for the lack of ordering in $IrSn_{0.45}Se_{1.55}$. Attempts to target $IrSn_{0.5}Se_{1.5}$ were unsuccessful, resulting in a ~21 wt% $Ir_2Sn_3Se_3$ impurity, while attempts to target $IrSn_{0.4}Se_{1.6}$ had a ~12 wt% $IrSe_2$. In other words, accessing stoichiometric Ir_2SnSe_3 was not possible under our conditions, implying that it is less thermodynamically stable than competing phases. However, the off stoichiometric $IrSn_{0.45}Se_{1.55}$ is accessible as the tail of a $Ir_2Sn_{1-\delta}Se_{3+\delta}$ solid solution because it lies outside the phase field of the competing, more stable products.(see Figure 3.3).

Table 3.2: Crystallographic parameters for $Ir_2Sn_3Se_3$ using rhombohedral $R\bar{3}$ (148) obtained from Rietveld refinement of synchrotron powder diffraction data at room temperature. Atoms are restricted by symmetry as 2*c* (*x*, *x*, *x*) and 6*f* (*x*, *y*, *z*). Atomic displacement parameters (U_{iso}) for Sn and Se were constrained with each other and occupancies were fixed at nominal values and errors reported are from statistical uncertainties.

λ (Å)	0.41385		R_{wp}	8.646	
$a = b = c$ (Å)	8.955798(6)		R_p	7.266	
$\alpha = \beta = \gamma$ (°)	89.92625(5)		R_{exp}	8.052	
V (Å^3)	718.3098(14)		*GoF*	1.074	
Atom	Wyck. Pos.	*x*	*y*	*z*	U_{iso} (Å^2)
Ir1	2*c*	0.24568(9)	0.24568(9)	0.24568(9)	0.0048(2)
Ir2	6*f*	0.74433(9)	0.24428(10)	0.74537(9)	0.00522(9)
Sn1	6*f*	0.16794(13)	0.5001(2)	0.34972(14)	0.007338(10)
Sn2	6*f*	0.33250(13)	0.99841(12)	0.84959(14)	0.007338(10)
Se1	6*f*	0.8527(2)	0.6531(2)	0.9990(2)	0.006421(14)
Se2	6*f*	0.6499(2)	0.1518(2)	0.5000(2)	0.006421(14)

3.3.2 Structure of $Ir_2Sn_3Se_3$

Figure 3.1b shows synchrotron PXRD data for $Ir_2Sn_3Se_3$ with a Rietveld refinement using space group $R\bar{3}$. It was previously reported as a skutterudite. The prototypical $Im\,\bar{3}$ skutterudite is $CoAs_3$ which forms square $(As_4)^{4-}$ tetramers.[62] Our data shows a clear splitting of the (204) and (40$\bar{2}$) reflections shown in the left inset of Figure 3.1b. It is well known that changing the formula of skutterudites to $M_{2/3}TCh$ can lead to anion ordering, resulting in distorted $(T\text{-}Ch)_2$ tetramers and a reduction in crystallographic symmetry to $R\bar{3}$. Using this as a starting model, we are able to obtain an excellent fit of the model to the data. The resulting structure is in excellent agreement with recent single crystal work that also found a trigonal distortion[84]. The experimental trigonal unit cell is within 0.13% and 0.06% difference with the previously reported cubic and trigonal structures for $IrSn_{1.5}Se_{1.5}$ respectively[62,84]. Furthermore, SAED (not shown) does not indicate any doubling of the unit cell, or any other ordering, hence the unit cell and space group are well justified. Crystallographic parameters are in Table 3.2. Attempts to refine occupancies led to values within 1% of unity. The right inset in Figure 3.1b demonstrates the structure consists of $(Sn\text{-}Se)_2$ tetramers. The electron count can be understood as $Ir^{3+}{}_4(Sn_2Se_2)^{4-}{}_3$, which chemically compares well to other skutterudites.[62]

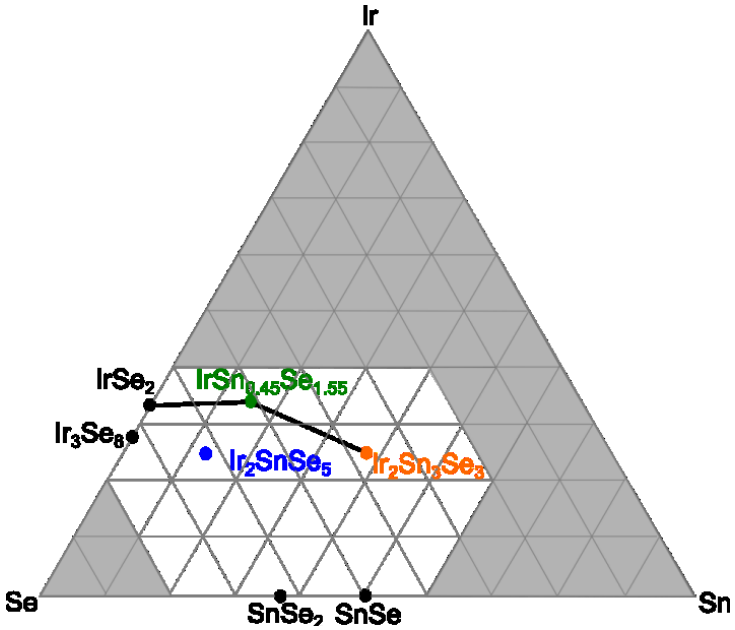

Figure 3.3: Ternary diagram for known Ir-Sn-Se compounds with a few proposed tie lines. Shaded areas are unexplored.

Table 3.3: Crystallographic parameters for Ir2SnSe5 using P21/m (11) obtained from Rietveld refinement of synchrotron powder diffraction data at room temperature. Atoms are restricted by symmetry as 2e (x, 1/4, z) and 4f (x y z). Atomic displacement parameters (Uiso) for Sn and Se were constrained with each other. Occupancies were fixed at nominal values and errors reported are from statistical uncertainties.

λ (Å)	0.41388	$\alpha = \gamma$ (°)	90	R_{wp}	12.078
a (Å)	7.65768(5)	β (°)	102.0831(6)	R_p	9.791
b (Å)	7.51027(5)	V (Å^3)	702.815(8)	R_{exp}	5.200
c (Å)	12.49737(8)			GoF	2.323
atom	Wyck. Pos.	x	y	z	U_{iso} (Å^2)
Ir1	4*f*	0.7439(20	-0.0015(5)	0.15063(10)	0.00567(14)
Ir2	2*e*	0.2475(3)	1/4	0.1395(2)	0.00567(14)
Ir3	2*e*	0.7474(3)	1/4	0.8364(2)	0.00567(14)
Se1	4*f*	0.0447(3)	-0.0038(11)	0.1091(2)	0.0106(2)
Se2	4*f*	0.5412(4)	-0.0041(10)	0.7821(2)	0.0106(2)
Se3	2*e*	0.3306(13)	1/4	0.9723(5)	0.0106(2)
Se4	2*e*	0.6677(13)	1/4	0.0222(5)	0.0106(2)
Se5	2*e*	0.8161(10)	1/4	0.3004(4)	0.0106(2)
Se6	2*e*	0.1833(10)	1/4	0.7165(5)	0.0106(2)
Se7	4*f*	0.7498(4)	-0.0023(10)	0.5202(2)	0.0106(2)
Sn1	2*e*	0.8352(8)	1/4	0.6513(3)	0.0089(4)
Sn2	2*e*	0.1651(8)	1/4	0.3360(3)	0.0089(4)

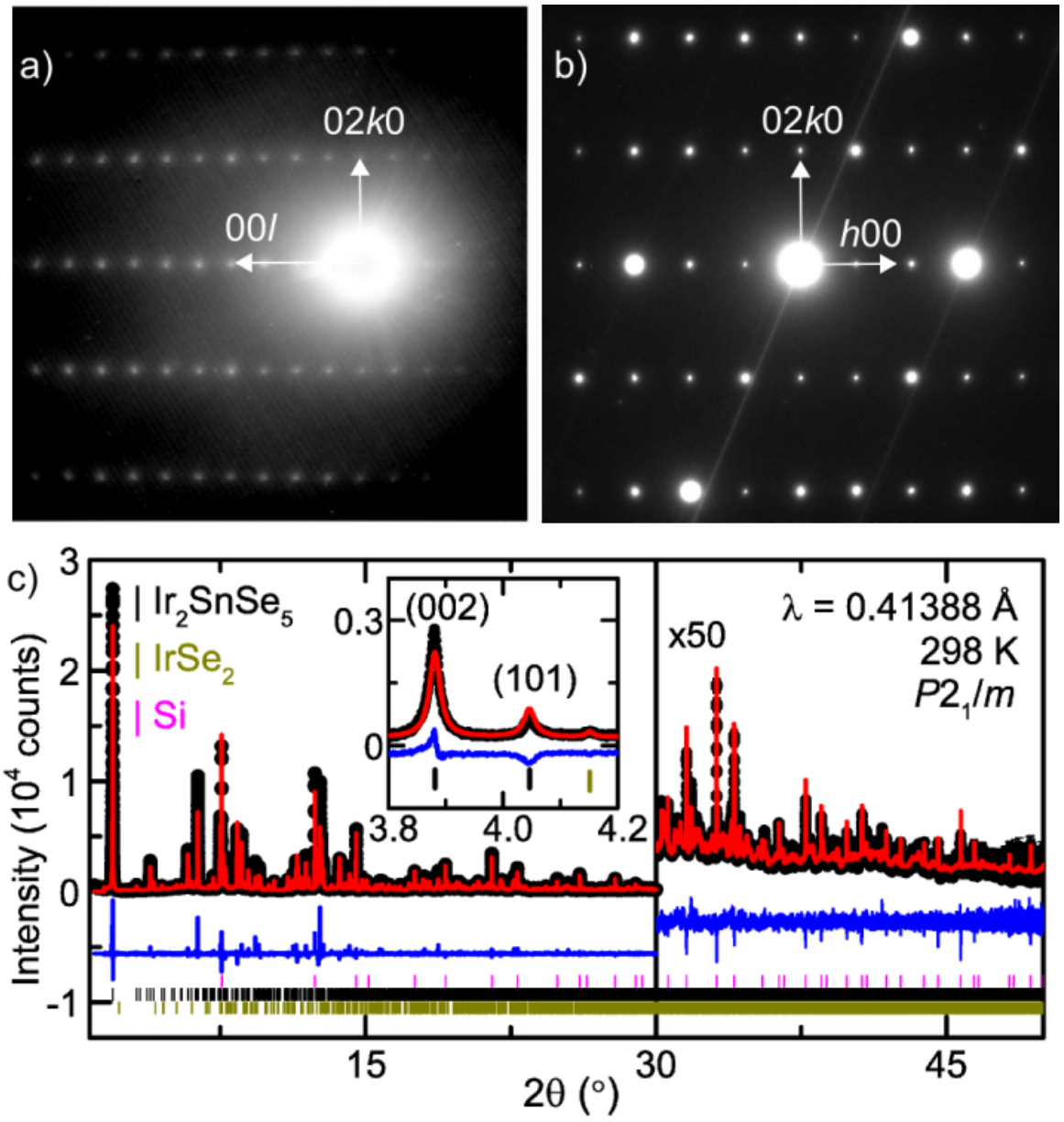

Figure 3.4: Selected area electron diffraction for Ir_2SnSe_5 of the **a)** (100) and **b)** (001) planes. **c)** Rietveld refinement of synchrotron powder X-ray data with internal Si standard. Experimental data shown as black circles, fit is in red, with the difference in blue. Inset shows that the model over-fits a 101 reflection and under-fits the 002 reflection. Contribution of ~1.75 wt% $IrSe_2$ impurity is also seen.

3.3.3 Structure of Ir_2SnSe_5

SAED patterns oriented in the [100] and [001] directions are shown in Figures 3.4a and 3.4b respectively for Ir_2SnSe_5. In the *y* direction the spacing in both

patterns is directly related to the *b* lattice parameter, while the *x* direction is directly related to the *c* and *a* lattice parameters for the (100) and (001) planes respectively. Figure 3.4c shows the room temperature synchrotron PXRD data for Ir_2SnSe_5. The corresponding Rietveld refinement, using space group $P2_1/m$, included a 1.75 wt% $IrSe_2$ impurity, as well as an internal Si standard. Crystallographic parameters are shown in Table 3.3.

The choice of space group and unit cell are justified through the SAED patterns and the synchrotron PXRD data. Hamilton R-ratio tests[12] and χ^2 ratio tests[13] against other space groups ($P1$, $P\bar{1}$, $P2$, $P2_1$, Pm, $P2/m$, $P2_1/m$:2) confirms, with 99% confidence, the choice of space group $P2_1/m$. Additionally, tests using ADDSYM in PLATON[96] did not find any additional symmetry. The lattice parameters determined from SAED are within 10% difference of those reported in Table 3.3, from Rietveld refinement, likewise the SAED patterns also do not show any evidence of additional order or doubling of the unit cell. Lastly, all observed peaks are fit by this model, and our model distinguishes between Sn and Se as Hamilton R-ratio tests[12] and χ^2 ratio tests[13] for alternative Sn positions shows 99.99% confidence of our proposed Sn position.

Nonetheless, the fit in Figure 3.4c is visibly imperfect due to lower angle peaks that are severely under-fit. This is highlighted by the inset in Figure 3.4 c where the model is seen to under-fit for the 002 reflection and over-fit for the 101 reflection. Systematically the model over-fits some reflections (e.g. 110, 103, etc.)

and under-fits other reflections (e.g. 002, 020, 100, etc.). These systematic deviations, along with the certainty in the unit cell, space group, and atomic positions then suggests a stacking fault in the *c* direction. Careful observation of the Ir_2SnSe_5 structure in Figure 3.5 demonstrates that a shift in the *b* direction could exist due to the Van der Waals gap. This shift would cause non-00l, non-0k0, and non-h00 reflections across layers to maintain total intensity but broaden and have less maximum intensity, while maintaining the sharpness other reflections (e.g. 002, 020, 100, etc.), as we observe. Thus we propose the imperfections of our model in describing the data are due to a stacking fault in the *c* direction.

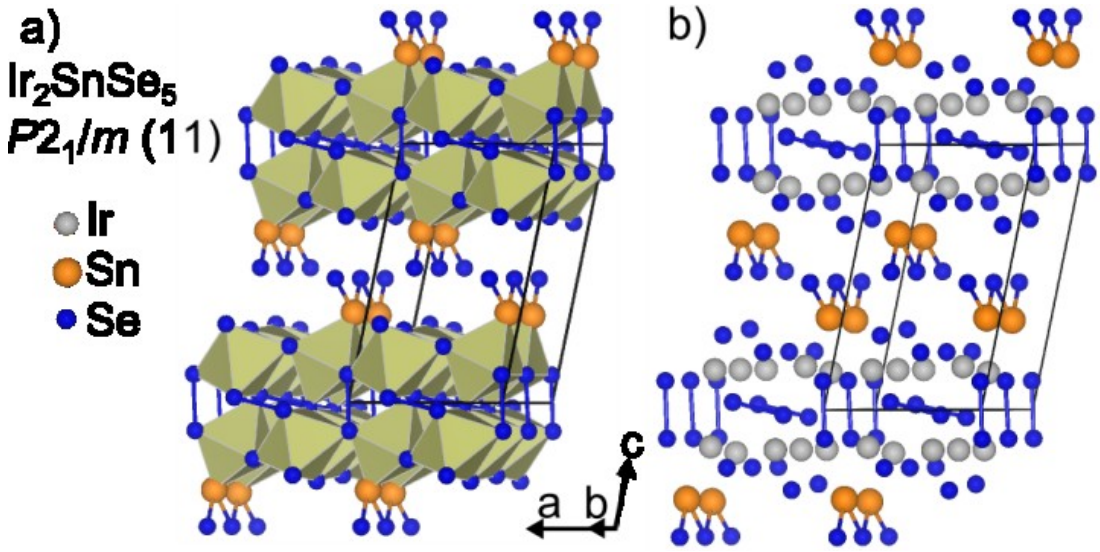

Figure 3.5: Structure of Ir_2SnSe_5 just off the *ac* plane **a)** highlighting corner-sharing in the *ac* plane, edge-sharing in the *bc* plane, and **b)** both Se-Se dimers and the $(Sn\text{-}Se)_n$ polymeric chain. Ir is shown in gray, Sn in orange, and Se in blue.

The proposed structure, shown in Figure 3.5, of the layered, distorted *β*-MnO_2 (pyrolusite)[97] type. Each layer contains a double $IrSe_6$ octahedral row,

corner-sharing in the *ac* plane and each row is edge-sharing in the *bc* plane. This structure bears similarity to the $IrSe_2$ structure, a three-dimensional structure that contains both a pyrolusite and ramsdellite building blocks.[76] Both Ir_2SnSe_5 and the pyrolusite portion of $IrSe_2$ contain $(Se_2)^{2-}$ anion dimers stabilizing the octahedra. Ir_2SnSe_5 is structurally distinct however, as it also contains a $(Sn\text{-}Se)_n$ polymeric chain "capping" each double octahedral layer. In other words, $IrSe_2$ can be structurally described as $Ir^{3+}{}_2(Se_2)^{2-}Se^{2-}{}_2$[76], Ir_2SnSe_5 is the same, but with the addition of a charge-neutral Sn-Se polymeric chain, i.e. $Ir^{3+}{}_2(Se_2)^{2-}Se^{2-}{}_2(SnSe)^0$.

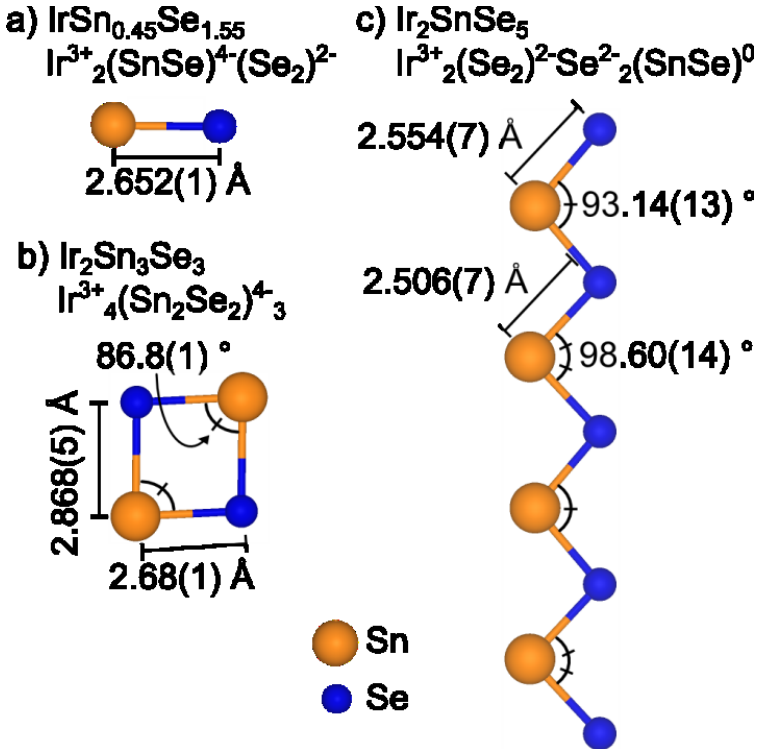

Figure 3.6: a) The Sn-Se dimer in $IrSn_{0.45}Se_{1.55}$. The distance given is an average for Se_2 and Sn Se dimers. **b)** The $(Sn\text{-}Se)_2$ tetramer in $Ir_2Sn_3Se_3$. **c)** The $(Sn\text{-}Se)_n$ polymeric chain in Ir_2SnSe_5.

3.3.4 Sn-Se bonding in the Ir-Sn-Se system

Each Ir-Sn-Se compound contains some form of anion-anion, or Zintl-like bonding. This is common for Ir compounds, as Ir*Ch*$_2$ (*Ch* = S, Se, or Te) compounds all have similar effects.[76–78] Figure 3.6 highlights the difference in Sn-Se anion-anion bonding in each Ir-Sn-Se compound. $IrSn_{0.45}Se_{1.55}$ contains both $(Se\text{-}Se)^{2-}$ and $(Sn\text{-}Se)^{4-}$ dimers, with an average distance of 2.652(1) Å. $Ir_2Sn_3Se_3$ contains $(Sn\text{-}Se)_2$ tetramers instead, with a long and short distance of 2.868(5) Å and 2.68(1) Å. This is exactly what is expected if two $(Sn\text{-}Se)^{4-}$ dimers are joined together along with the removal of four electrons.

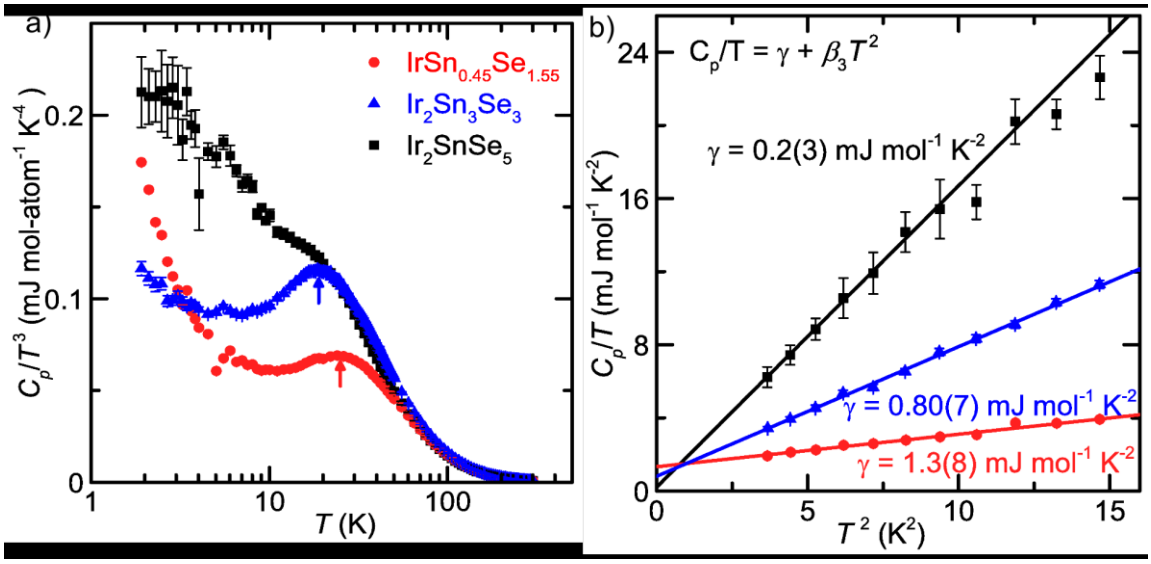

Figure 3.7: a) Heat capacity over temperature cubed versus log of temperature for Ir_2SnSe_5 (black squares), $IrSn_{0.45}Se_{1.55}$ (red circles), and $Ir_2Sn_3Se_3$ (blue triangles), scaled per atom, emphasizing an Einstein mode that shifts to lower energy (red and blue arrows). **b)** Heat capacity over temperature versus temperature squared highlighting the electronic heat capacity (γ). Solid lines are fits extrapolated to zero.

The bond distances in the Sn-Se polymeric chain are shorter than the in the dimer and tetramer, which indicates more ionic character. This is expected from an electron counting argument, as the valence for Sn is formally -2, 0, and

+2 for $(Sn\text{-}Se)^{4-}$ dimers, $(Sn\text{-}Se)_2^{4-}$ tetramers, and $(Sn\text{-}Se)_n$ respectively, following a trend of Zintl-like bonding to more ionic type bonding.

3.3.5 Physical Properties

Figure 3.7a shows the heat capacity for Ir_2SnSe_5, $IrSn_{0.45}Se_{1.55}$, and $Ir_2Sn_3Se_3$ as C_p/T^3 vs log$T$ to highlight acoustic and optic phonon modes.[98] Plotted in this way Einstein (optic) modes, appear as a peak, while Debye (acoustic) modes, increase upon cooling until becoming constant. Additionally, electronic heat capacity appears as a sharp increase at low temperatures. Scaling all three data sets by the amount of amounts indicates that all three have a similar Debye and Einstein mode. This Einstein mode appears to decrease in energy from $IrSn_{0.45}Se_{1.55}$ to $Ir_2Sn_3Se_3$ (red and blue arrows respectively), and contributes even less to Ir_2SnSe_5. Meanwhile the contribution of a Debye mode appears to increase from $IrSn_{0.45}Se_{1.55}$, to $Ir_2Sn_3Se_3$, to Ir_2SnSe_5. Both observations are consistent with the change in Sn-Se bonding, which goes from dimers, to tetramers, to polymeric chains. As the connectivity of the dimers increases, their dimensionality increases, and their associated modes broaden and appear more Debye-like, as seen for the heat capacity of Ir_2SnSe_5 which is almost purely Debye-like. The small feature at T ~ 4.5 K for all three is due to helium condensation around this temperature.

The plot of C_p/T vs T^2 in Figure 3.7b shows the relationship between the electronic (γ) and phonon (β_3) contributions to specific heat, fit to the equation

$C_p/T = \gamma + \beta_3 T^2$.[2] Ir_2SnSe_5 has an electronic specific heat which within error of zero (0.2(3) mJ K^{-2} mol^{-1}), while $Ir_2Sn_3Se_3$ is has a non-zero γ of 0.80(7) mJ K^{-2} mol^{-1}. The small, non-zero γ for $Ir_2Sn_3Se_3$ is in agreement with the low temperature ($T < 2$ K) upturn in C_p/T^3 in Figure 3.7a. Similarly, $IrSn_{0.45}Se_{1.55}$ also has a non-zero γ = 1.3(8) mJ K^{-2} mol^{-1} which is also in agreement with the sharp increase in low temperature ($T < 5$ K) C_p/T^3 in Figure 3.7a.

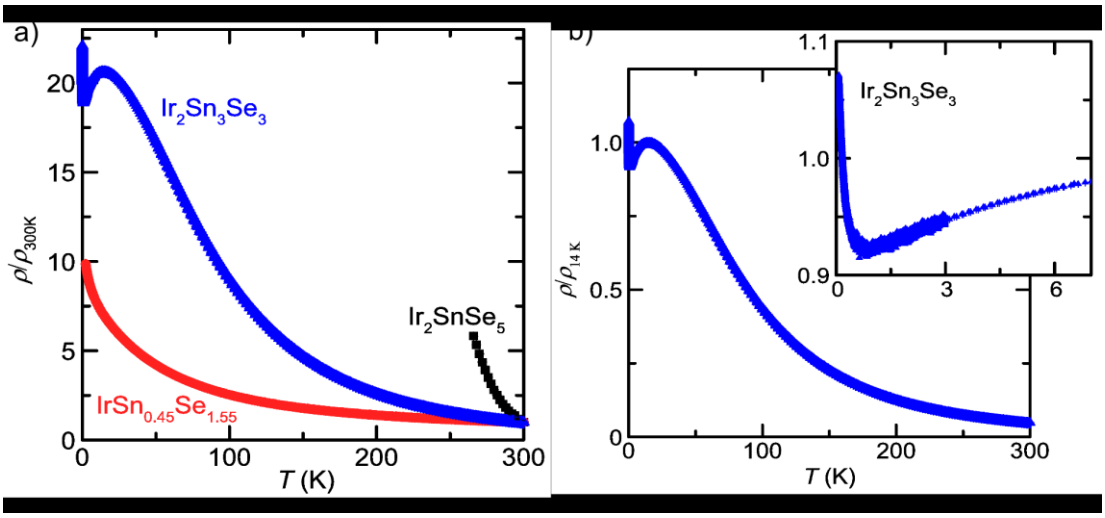

Figure 3.8: a) Normalized resistivity as a function of temperature for Ir_2SnSe_5 (black squares), $IrSn_{0.45}Se_{1.55}$ (red circles), and $Ir_2Sn_3Se_3$ (blue triangles). Errors are contained in the size of the symbols. **b)** Normalized for $Ir_2Sn_3Se_3$ shows a broad feature at T = 40 K and then an increase again at T = 0.75 K.

Normalized resistivity for Ir_2SnSe_5, $IrSn_{0.45}Se_{1.55}$, and $Ir_2Sn_3Se_3$ is shown in Figure 3.8. The rate at which the normalized resistivity increases at lower temperatures is proportional to the size of its' semiconducting gap, which increases from $IrSn_{0.45}Se_{1.55}$, to $Ir_2Sn_3Se_3$, to Ir_2SnSe_5. Ir_2SnSe_5 could not be measured below T = 266 K due to the large resistivity, which agrees with the zero electronic contribution of specific heat in Figure 3.7b. Though the insulating resistivity of $IrSn_{0.45}Se_{1.55}$ is conflicting with the heat capacity in Figure 3.8, it is

not uncommon for a semiconductor to have a non-zero γ due to a finite doping (carrier concentration). $Ir_2Sn_3Se_3$ is also semiconducting with a non-zero γ, however it is accompanied by unique low temperature (T > 40 K) behavior.

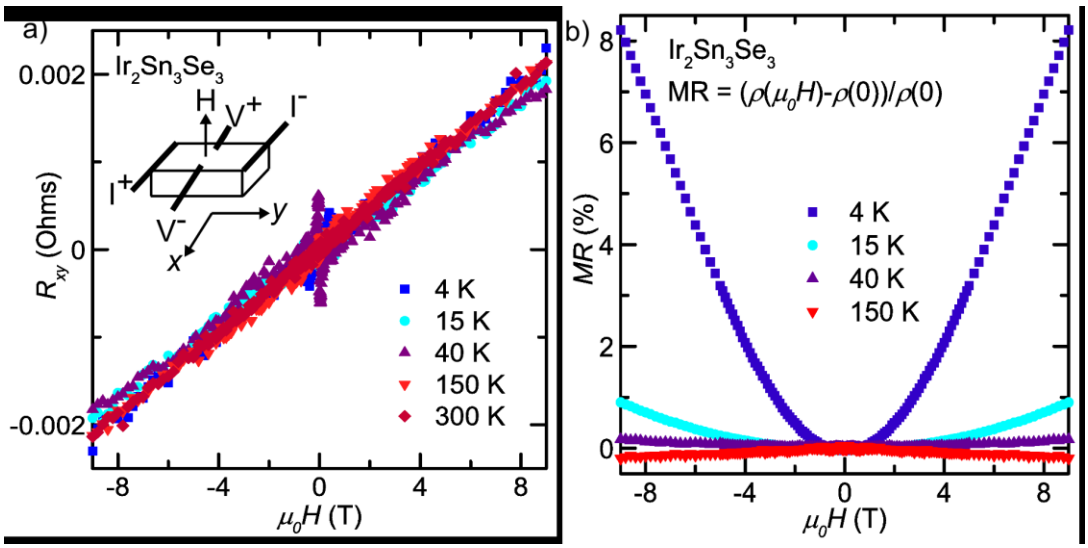

Figure 3.9: a) Hall resistance versus applied field for $Ir_2Sn_3Se_3$ at various temperatures. The inset shows the experimental setup. **b)** Magnetoresistance (MR) of $Ir_2Sn_2Se_3$ as a function of applied field. The magnitude changes sign around T = 40 K and increases as temperature decreases. Errors are contained by the size of the symbols for both.

The normalized resistivity for $Ir_2Sn_3Se_3$, shown in Figure 3.8b, follows insulating behavior until $T \sim 40$ K, where it first appears to plateau, then decreases, until finally increasing again at $T \sim 0.75$ K. Though there are many complex explanations for this phenomenon, this type of behavior is well known in heavily doped semiconductors, and has been observed in p-type Ge [99,100] and modeled in p-type Si[101] for similar carrier concentrations.

Hall resistance (R_{xy}) measurements as a function of applied field are shown in Figure 3.9a for several temperatures (T = 4, 15, 40, 150, 300 K). The

sample setup is shown in the inset in Figure 3.9a and the data was symmeterized. The slope of these lines, normalized by sample thickness (d), give the Hall coefficient (R_H), which is equal to $1/ne$ where n is the carrier concentration and e is the elementary charge.[5] All temperatures have a similarly positive slope, indicative of p-type doping and a roughly temperature-independent carrier concentration of 2.2(2)*10^{19} cm^{-3}. This carrier concentration agrees with the previously reported 2.3*10^{19} cm^{-3},[62] the resistivity in Figure 3.8, and the small, non-zero γ in Figure 3.7. Both p-type Ge and Si show similar resistivity versus temperature behavior for a carrier concentration ~10^{19} cm^{-3}, and an electronic specific heat is expected. Semiconducting behavior is also expected as the carrier concentration is still below the Mott metal to insulator transition (n < ~10^{22} cm^{-3}).[102,103]

There is a small apparent increase in the carrier concentration from Hall measurements from 2.01(2)*10^{19} cm^{-3} to 2.40(2)*10^{19} cm^{-3}, from T = 300 K to T = 15 K respectively. This is most logically explained as arising from thermally excited states across the gap at high temperature. This explanation is consistent with the normalized resistivity for $Ir_2Sn_3Se_3$, which increases until becoming constant at T = 15 K, where the intrinsic gap no longer contributes thermal n-type carriers. At T < 15 K the carrier concentration decreases to 1.91(2)*10^{19} cm^{-3} at T = 4 K as extrinsic p-type carriers begin to decrease. Attempts to fit this data with a simple multi-gap model, as done by Fritzsche,[99] have proved

unsuccessful. A successful model to this data would need to include not only impurity scattering (neutral and charged), lattice scattering, and hole-hole scattering for both intrinsic and extrinsic carriers as done by Li [101]; but this model would also need to include grain effects due to a sintered sample. The complexity of a model that could successfully describe these effects is beyond the scope of this manuscript.

Table 3.4: Mobilities extracted from Hall (μ_H) and Resistivity (μ) data.

T (K)	μ_H ($cm^2V^{-1}s^{-1}$)	μ ($cm^2V^{-1}s^{-1}$)
4	0.84(8)	0.10(1)
15	0.95(9)	0.078(7)
40	0.88(8)	0.030(3)
150	3.6(3)	0.40(4)
300	11(1)	1.9(2)

Hall mobilities were also calculated using $\mu_H = R_H/\rho_{xx}$, with the values shown in Table 3.4. These values are roughly in agreement with those calculated from resistivity alone ($\rho^{-1} = en\mu$), also shown in Table 3.4. The above relationship between resistivity and mobility also explains why the mobilities decrease as temperature decreases, as the carrier concentration is roughly temperature-independent. The mobility values are also reasonable considering the semiconducting behavior of $Ir_2Sn_3Se_3$, and the Hall mobilties are within 3% difference from those previously reported in Ref. 4. Both resistivity and Hall measurements probe the experimental mobility, with values that are an

"average" of extrinsic and intrinsic carriers. It is likely that a probe which better measures only the extrinsic carriers would yield a larger mobility.

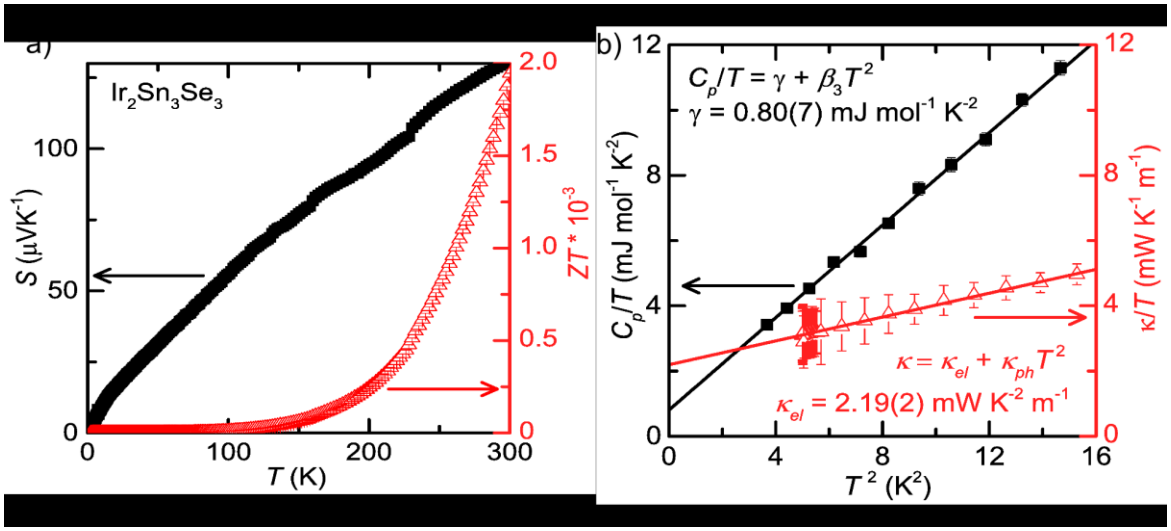

Figure 3.10: a) Seebeck coefficient (black squares) and the dimensionless *ZT* figure of merit (red triangles) as a function of temperature for $Ir_2Sn_3Se_3$. **b)** Thermal conductivity (red triangles) and heat capacity (black squares), both over temperature, as a function of T^2 to separate lattice and electronic contributions.

Magnetoresistance (*MR*) for $Ir_2Sn_3Se_3$ is shown in Figure 3.9b for various temperatures. *MR* is commonly defined as $(\rho(H)-\rho(0))/\rho(0)$ and given as a percent. This data was collected using the sample setup shown in the inset of Figure 3.9a and was symmeterized. For single-carrier semiconductors *MR* is positive and follows a $1+(\mu H)^2$ trend, where μ is the mobility and H is the applied field.[1] $Ir_2Sn_3Se_3$ appears to not follow these trends for several reasons. The *MR* for $Ir_2Sn_3Se_3$ is only positive when $T \leq 40$ K, which is where the resistivity begins to plateau (Figure 3.8b), and the intrinsic gap no longer contributes carriers. Secondly, *MR* for $T = 4$ K appears to follow Kohler's rule ($MR = 1+(\mu_{MR}H)^2$)[1] initially, with $\mu_{MR} = 366(3)$ $cm^2V^{-1}s^{-1}$, but then appears to have a linear

relationship above $\mu_0 H$ = 3 T. This deviation could arise for a myriad of reasons, such as the polycrystalline nature of the sample, different carrier types, or a function of anisotropy.[1] The magnitude of μ_{MR} is also much higher than that from resistivity and Hall measurements, however this is likely due to this mobility being from extrinsic carriers alone, which would have a higher mobility than intrinsic carriers. Single crystal studies are necessary to truly determine the origin of the linear *MR* behavior at higher fields.

Results from thermal transport measurements are shown in Figure 3.10a for the skutterudite $Ir_2Sn_3Se_3$. The left axis of Figure 3.10a shows the Seebeck coefficient (S) versus temperature, and appears positive and roughly linear. Noting that $S \propto m^* n^{-2/3} T$,[104] this suggests that the carrier concentration (n) and enhanced mass (m^*) are roughly temperature independent. The sign of the S indicates $Ir_2Sn_3Se_3$ is hole doped, in agreement with the Hall measurements in Figure 3.3a, which also indicates *p*-type doping and a roughly temperature-independent carrier concentration. The right axis of Figure 3.10b shows the dimensionless ZT figure of merit, with $ZT = S^2\sigma T/\kappa$.[104] The shape of the curve is well understood, as it follows the trends of S^2 and the inverse of the resistivity for $Ir_2Sn_3Se_3$.

3.3.6 Band Calculations

Representative calculations Ir_2SnSe_5 and $IrSn_{0.45}Se_{1.55}$ are shown in Figures 3.11a and 3.11c respectively, using a 10 x 10 x 6 and a 4 x 4 x 4 k-mesh respectively. Ir_2SnSe_5 is seen to be an indirect gap semiconductor, while $IrSn_{0.45}Se_{1.55}$ is seen to be a semimetal. Ir_2SnSe_5 converged within an absolute energy difference of 10^{-3} Ha whereas all other calculations converged with an absolute energy difference of ~10^{-4} Ha. The $IrSn_{0.45}Se_{1.55}$ calculation used an ordered, more stoichiometric, lower symmetry $P2_1$ model, which is not fully representative of the higher symmetry, off-stoichiometric, disordered structure.

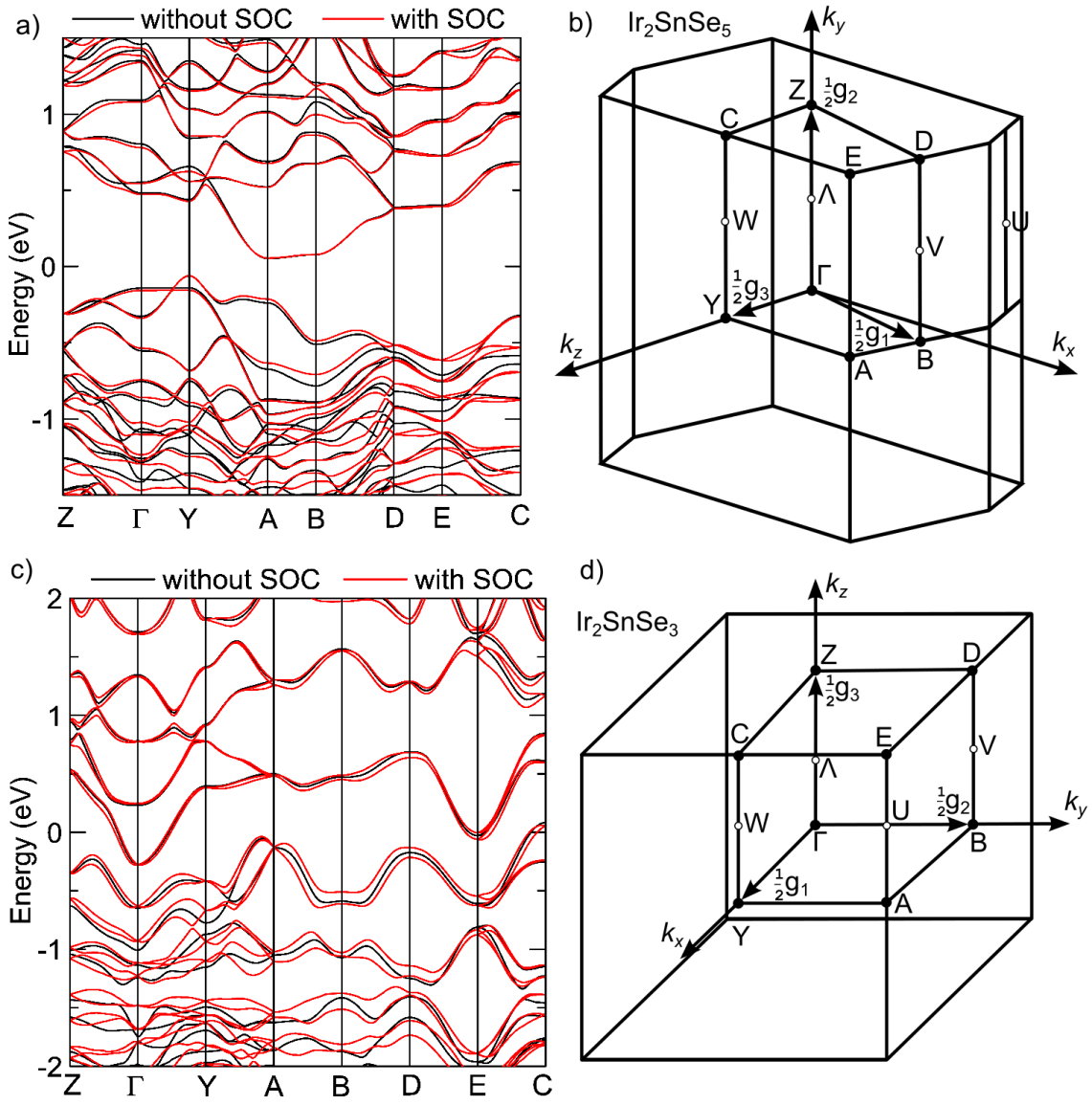

Figure 3.11: a) Electronic band structure for Ir_2SnSe_5 with (red) and without (black) spin-orbit coupling (SOC) using **b)** $P2_1/m$ Brillouin zone. **c)** Electronic band structure for Ir_2SnSe_3 with (red) and without (black) SOC using **d)** a lower symmetry $P2_1$ Brillouin zone.

Calculations on $Ir_2Sn_3Se_3$ were run to further understand the electronic and transport properties, shown in Figure 3.12. The band structure in Figure 3.12a with the associated Brillouin zone in Figure 3.12c, implies that despite the complex structure, $Ir_2Sn_3Se_3$ is a semiconductor, with a direct gap of ~0.4 eV at the Γ point and a single valence band, in excellent agreement with the 0.43 eV

gap determined by Yan et. al.[84]. Ir-*d* and Se-*p* states contribute to the bands directly above and below the Fermi level respectively. Such a simple band structure is unexpected from the structure, which warrants further investigation of the bands at the Γ point.

High pressure (compressive strain/reduced unit cell) calculations were conducted, which led to an unexpected *increase* in the band gap. This led to reduced pressure calculations (tensile strain), using lattice parameters increased by 0.6 Å (a 6.7% increase), with the band structure shown in Figure 3.12b. This shrinkage of the unit cell led to an inversion of the Ir-*d* and Se-*p* states at the Γ point. The Z_2 topological invariant was calculated at each of the TRIM points, which for $R\bar{3}$ are Γ, 3F, 3L, and Z. Multiplying the parity from the occupied states at each TRIM, then multiplying the parity of the TRIM points, reveals that $Ir_2Sn_3Se_3$ is topologically trivial (Z_2 = +1), while tensile strained $Ir_2Sn_3Se_3$ is topologically nontrivial (Z_2 = -1) due to the inversion of Ir-*d* and Se-*p* states at the Γ point. Additional calculations show that $Ir_2Sn_3Se_3$ has a topological index of 1:(0,0,0), consistent with a strong topological insulator with a band inversion at Γ.

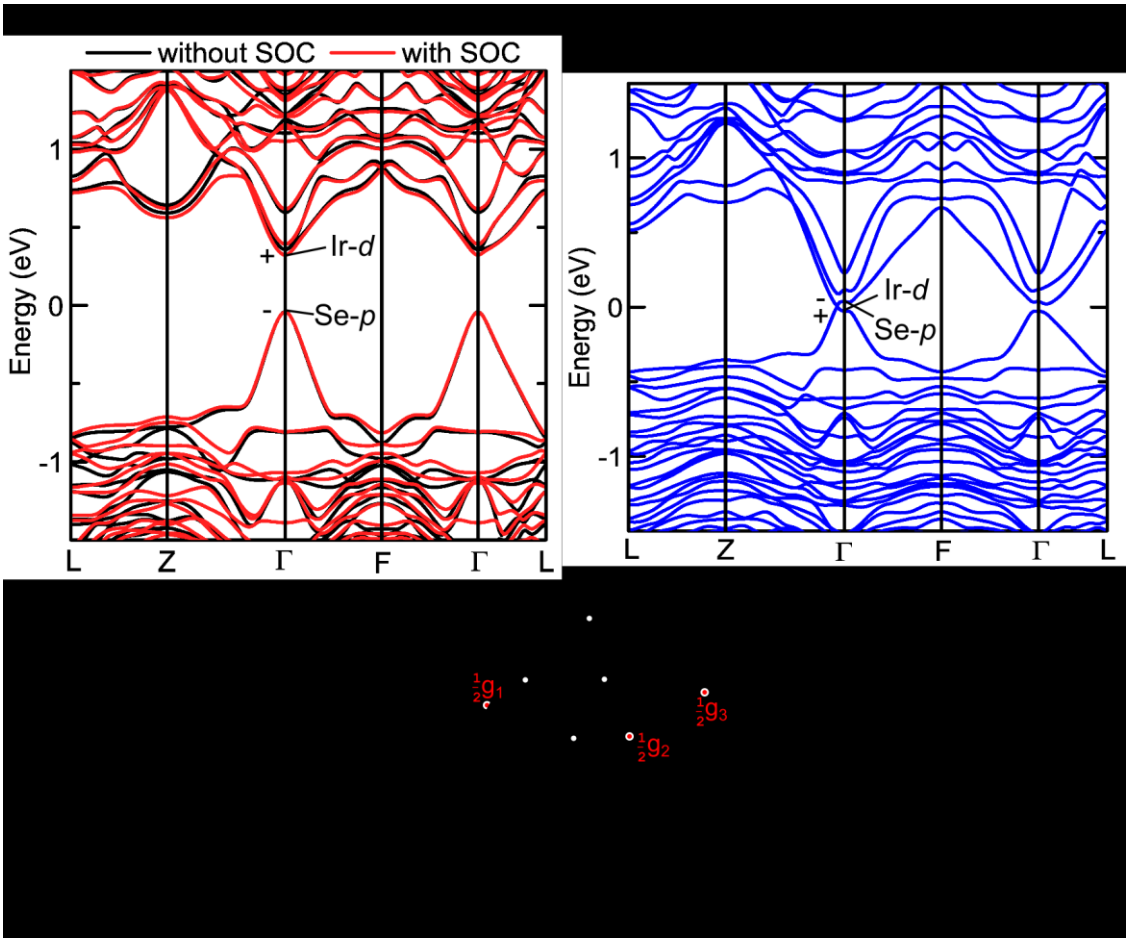

Figure 3.12: a) Band structure for $Ir_2Sn_3Se_3$ without (black) and with (red) spin-orbit coupling (SOC). Ir-d states are seen just above the Fermi level, while Se-p states are just below. **b)** Tensile strained band structure for $Ir_2Sn_3Se_3$, using a unit cell uniformly expanded unit cell by 0.6 Å. The Ir-p and Se-d states at the Γ point invert. **c)** The Brillioun zone for $R\bar{3}$ $Ir_2Sn_3Se_3$ with special points and reciprocal lattice vectors shown.

Using the determined carrier concentration of $n = 2.2(2)*10^{19}$ cm^{-3}, the electronic specific heat of $\gamma = 0.80(7)$ mJ mol^{-1} K^{-2}, along with the electronic band structure and density of states (DoS) calculations, we determine an enhanced mass (m^*/m) of 7.0(4). This then allows us to calculate a mobility from $\mu = e\tau/m^*$, and the relationship between heat capacity (C) and thermal conductivity (κ), $\kappa = \frac{1}{3}Cv^2\tau$.[5] The respective electronic heat capacity and thermal conductivity is

shown Figure 3.10b, plotted versus T^2 to separate the electronic (γ and κ_{el}) and phonon (β_3 and κ_{ph}) contributions.[2,3] This leads to a mobility of 1110(60) $cm^2V^{-1}s^{-1}$, a value much larger than the experimental mobilities calculated from resistivity and Hall measurements. This difference is due to what each experimental probe measures - resistivity and Hall measurements probe an "average" for all types of carriers, both intrinsic and extrinsic. Electronic heat capacity and electronic thermal conductivity are only from the number of carriers at the Fermi level, which are extrinsic *p*-type carriers due to defects. These extrinsic carriers would have a much larger mobility than thermal intrinsic carriers across a ~0.4 eV gap. Therefore we propose the mobilities of 366(3)-1110(60) $cm^2V^{-1}s^{-1}$ are from extrinsic carriers and the mobilities of 0.1-10 $cm^2V^{-1}s^{-1}$ are from both extrinsic and intrinsic carriers.

3.4 Conclusion

The structures of $IrSn_{0.45}Se_{1.55}$, $Ir_2Sn_3Se_3$, and Ir_2SnSe_5 are reported. $IrSn_{0.45}Se_{1.55}$ is a new $Pa\overline{3}$ pyrite phase with randomly distributed Sn-Se and Se-Se dimers. $Ir_2Sn_3Se_3$ is a trigonally-distorted $R\overline{3}$ skutterudite, and the lattice parameter is within 0.13% of that previously reported cubic structure[62]. Ir_2SnSe_5 is a new, layered, β-MnO_2-like structure, containing double octahedral $IrSe_6$ rows, corning-sharing in the *a* direction, and edge-sharing in the *b* direction, with each double octahedral layer effectively "capped" by $(Sn\text{-}Se)_n$ polymeric chains.

Electron counting suggests formulas of $Ir^{3+}_2(SnSe)^{4-}(Se_2)^{2-}$ for $IrSn_{0.45}Se_{1.55}$, $Ir^{3+}_4(Sn_2Se_2)^{4-}_3$ for $Ir_2Sn_3Se_3$, and $Ir^{3+}_2(Se_2)^{2-}Se^{2-}_2(SnSe)^0$ for Ir_2SnSe_5 with Sn-Se dimers, $(Sn\text{-}Se)_2$ tetramers, and $(Sn\text{-}Se)_n$ polymeric chains respectively. The anion anion bonding is consistent with other Ir chalcogenides.[76–78] All three compounds are insulating and diamagnetic indicative of $5d^6$ Ir^{3+}.

Hall measurements, thermal transport, heat capacity, and resistivity measurements, as well as electronic structure calculations, on $Ir_2Sn_3Se_3$ demonstrate *p*-type doping with a carrier concentration of $2.2(2)*10^{19}$ cm^{-3}, an enhanced mass (m^*/m) of 7.0(4), electronic specific heat (γ) of 0.80(7) mJ mol^{-1} K^{-2}, electronic thermal conductivity (κ_{el}) of 2.19(2) mW K^{-2} m^{-1}. Heat capacity measurements also show an Einstein mode which broadens and becomes more Debye-like as the dimensionality of anion-anion bonding increases. Mobilities of 366(3)-1120(6) $cm^2V^{-1}s^{-1}$ were determined for extrinsic *p*-type carriers, using magnetoresistance, heat capacity, and thermal conductivity. Resistivity and Hall measurements also measured mobilities of 0.1-10 $cm^2V^{-1}s^{-1}$ which represent the overall mobility of both extrinsic and intrinsic carriers.

Electronic band structure calculations also reveal that $Ir_2Sn_3Se_3$ is a direct-gap semiconductor with a gap of ~0.4 eV. Uniformly expanding the unit cell by 0.6 Å appears to turn $Ir_2Sn_3Se_3$ into a topological insulator. Though this 6.7% enlargement is moderately sizable, such an increase may be possible with strain and/or similar compounds with larger atoms.

3.5 Acknowledgements

This work was supported by NSF, Division of Materials Research (DMR), Solid State Chemistry (SSMC), CAREER grant under Award DMR-1253562, and the ICDD Ludo Frevel Crystallography Scholarship. Use of Dilution Refrigerator funded by National Science Foundation Major Research Instrumentation Program under NSF DMR-0821005. B.A.T. also acknowledges useful discussions with A.M. Fry, W.A. Phelan, and K. JT Livi.

4. Structure, Properties, and Disorder in the New Distorted-Hollandite $PbIr_4Se_8$

Under Review, *Journal of Solid State Chemistry*

Benjamin A. Trump[a,b] and Tyrel M. McQueen[a,b,c]

[a]Department of Chemistry, Johns Hopkins University, Baltimore, MD 21218, United States

[b]Department of Physics and Astronomy, Institute for Quantum Matter, Johns Hopkins University, Baltimore, MD 21218, United States

[c]Department of Material Science and Engineering, Johns Hopkins University, Baltimore, MD 21218, United States

4.1 Introduction

The Hollandite structure, prototypically α-MnO_2, is a well studied family of materials for battery,[105–107] thermoelectric,[108,109] and even magnetic applications.[110,111] The formula can be better written as $M_xT_4O_8$, where M = early lanthanides, alkali metals, or alkali earth metals, x = 0-1, and T = Mn, Mo, Ru, or Ir.[112–115] A similar compound, the pseudo-Hollandites, have an even more expansive series, $M_xT'T_4Ch_8$ where M = Tl, In, Cd, Sn, Pb, alkali metals, or alkaline earth metals, x = 0-1, T,T' = Ti, V, or Cr, and Ch = S, Se, or Te.[116,117] The structure of both series consists of double chains of edge-sharing T-O octahedra which corner-share with other double octahedral chains to form a framework structure containing large one-dimensional (1-D), with a cation M, occupying the site in the channels.

Despite the wealth of cations and transition metals which take this structure, only KIr_4O_8 and $Rb_{0.68}Ir_4O_8$ contain a 5d transition metal,[113,118] which have recently attracted significant interest due to strong spin-orbit coupling which could lead to nontrivial behavior.[65] These relativistic effects having comparable energy scales with crystal field stabilization or electron correlations is expected to lead to exotic quantum or magnetic behavior.[66–68] Iridium in particular, especially iridium chalcogenides, has been heavily studied for these reasons.

Though some non-oxide iridium chalcogenides have been studied, they are primarily derivatives of the binary compounds IrS_2, $IrSe_2$, and $IrTe_2$.[79–82] Some recent work has been done on stoichiometric ternary Ir-Sn-Se compounds,[84,119] though none have yet looked at other stoichiometric ternary Ir-Se-X compounds.

Here we report the synthesis, structure, and some physical properties of the new compound $PbIr_4Se_8$. This structure is analogous, but structurally distinct, to Hollandite, which contains similar 1-D channels. As far as the authors are aware, this is the first non-oxide 5*d* Hollandite. Due to the large size of the 1-D channels, and Pb lone-pair effects, considerable disorder is seen on the Pb site, evidenced by power X-ray diffraction (PXRD), selected area electron diffraction (SAED), X-ray pair distribution analysis (PDF), and heat capacity. $PbIr_4Se_8$ is diamagnetic, indicative of low-spin $5d^6$ Ir^{3+}, and has semiconducting character, evidenced by heat capacity and band structure calculations.

4.2 Experimental

4.2.1 Preparation

Polycrystalline $PbIr_4Se_8$ was grown by placing Ir (Alfa Aesar 99.95%), Pb (Alfa Aesar 99.999%), and Se (Alfa Aesar 99.999%) in the stoichiometric ratio of $(PbSe)_{1.1}(IrSe_2)_2$, in a fused silica tube, for a total of 300 mg. Tubes were backfilled with 1/3 atm of Ar to minimize vaporization of Se. The tube was heated quickly to 500 °C, followed by a 50 °C/h ramp to an annealing temperature of 950 °C,

and held for four days before quenching in water. The resulting boule was pulverized, and the heat sequence and quench was repeated a second time. This resulted in shiny, silver PbSe micro-rings as well as loose, gray powder. After PbSe was mechanically removed, the resulting phase pure powder was used for all physical property and characterization methods. Attempts to target a myriad of alternate stoichiometries at several lower temperatures all led to the same $PbIr_4Se_8$ material with varied amounts of PbSe/$IrSe_2$ impurities. Specifically, attempts with less Pb and Se always included non-phase separating $IrSe_2$ impurities.

Additionally intercalation/deintercalation reactions were also conducted. Deintercalation reactions were done by placing ~100 mg of $PbIr_4Se_8$ in a 0.2 M solution of Br_2 in acetonitrile overnight at room temperature. These reactions were also conducted using I_2 instead, however this led to more structural degradation and less Pb removed. Intercalation reactions were conducted using a 1:1.1 Li:Ph_2CO (benzophenone) 0.2 M solution in tetrahydrofuran (THF), with a roughly tenfold excess of Li to $PbIr_4Se_8$. The intercalation reaction also involved stirring overnight at room temperature.

4.2.2 Characterization

Laboratory powder X-ray diffraction (PXRD) patterns were collected using a Cu K_α (λ_{avg} = 1.5418 Å) on a Bruker D8 Focus diffractometer with a LynxEye detector. Peak searching and LeBail refinements were used for phase

identification and initial lattice parameter estimates in TOPAS (Bruker AXS). Simulated annealing was then used to estimate atomic positions. Finally, Rietveld refinements determined precise atomic positions and lattice parameters, using TOPAS and GSAS-II[120] respectively. To verify the choice of lattice parameters and spacegroup, transmission electron microscopy (TEM) was used with a Phillips CM300 atomic resolution transmission electron microscope equipped with a field emission gun with an accelerating voltage of 300 kV. A CCD camera (bottom mounted Orius camera) was used to collect a tilt series of selected area electron diffraction (SAED) images, tilting from the [001] direction to the [$\bar{2}\ \bar{1}$ 3] direction. Structures were visualized using VESTA.[50]

Synchrotron X-ray diffraction for pair distribution analysis (PDF) was collected at the beamline 11-ID-B at the Advanced Photon Source, Argonne National Laboratory with an X-ray wavelength of 0.2112 Å. A CeO2 standard was used to estimate the resolution of the instrument. Data was reduced using Fit2D[121] and PDFgetX2[122] and was finally analyzed using PDFgui[123].

Heat capacity and magnetization were collected on a cold-pressed pellets in a Physical Property Data Measurement system (PPMS, Quantum Design), for 1.8 K ≤ T ≤ 300 K. Heat capacity was measured using the semiadiabatic pulse technique, with three repetitions at each temperature. Magnetization was measured with $\mu_0 H$ = 1 T.

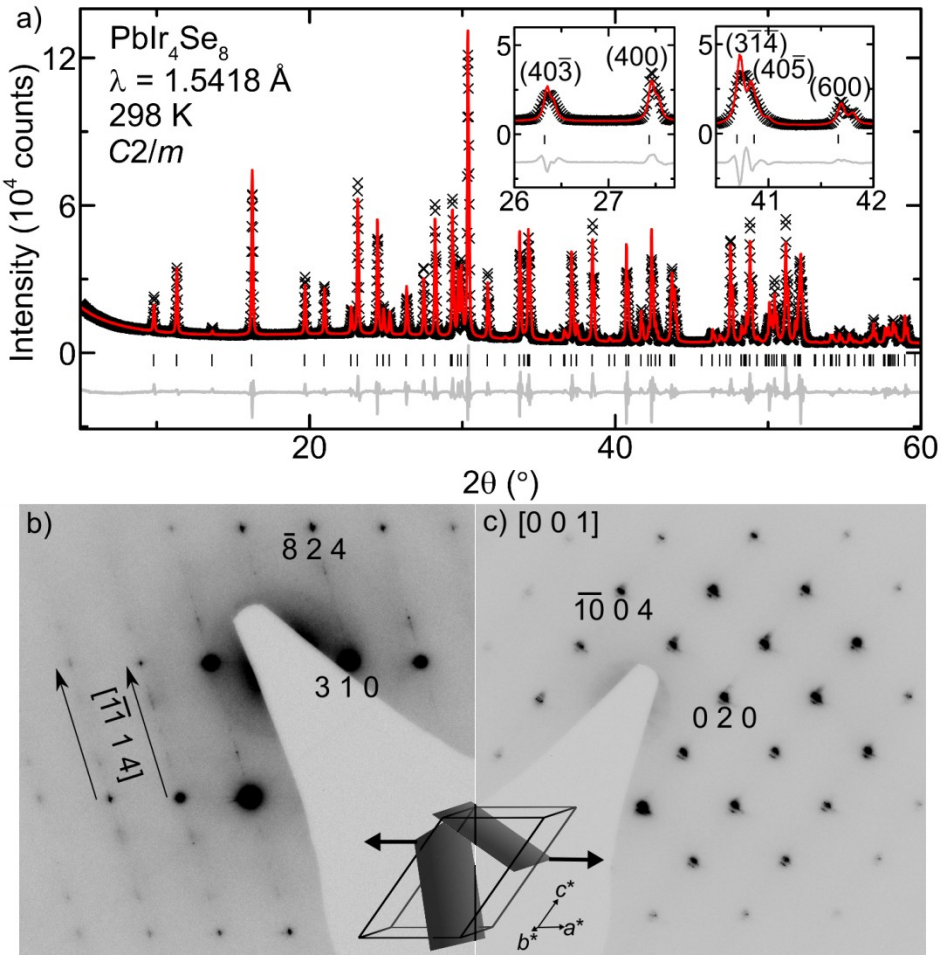

Figure 4.1: a) Laboratory powder X-ray diffraction for $PbIr_4Se_8$ shown as black X's, fit in red, and difference in gray. Insets demonstrate some peaks are appreciably broadened. **b)** Transmission electron diffraction close to the [$\overline{12}$ $\overline{5}$ 39] and **c)** along the [001] directions for $PbIr_4Se_8$. The inset displays the corresponding planes. Diffuse scattering (streaking) is seen in the [$\overline{11}$ 1 4] direction.

4.2.3 Calculations

Electronic and band structure calculations were performed on Ir_4Se_8 using density functional theory (DFT) with the local density approximation (LDA) utilizing the ELK all-electron full-potential linearized augmented plane-wave plus local orbitals (FP-LAPW+LO) code.[85] Calculations were conducted both

with and without spin-orbit coupling (SOC) using a 4 X 18 X 6 *k*-mesh, with the experimentally determined unit cell.

Table 4.1: Crystallographic fit parameters for $PbIr_4Se_8$ using spacegroup *C*2/*m*(12). All atoms are on the 4*i*:(*x* 0 *z*) site, except for Pb1 which is on the 8*j*:(*x y z*) site. Occupancies on the two Pb Wyckoff sites were fixed to a total of 2 Pb per cell, all other occupancies were fixed at unity. Errors represent statistical uncertainties.

	a (Å)	15.901(3)		*V* (Å^3)	534.90(7)		R_{wp} (%)	8.23
	b (Å)	3.7300(1)		*λ* (Å)	1.5418		R_p (%)	5.41
	c (Å)	11.035(4)		*T* (K)	296(1)		R_{F^2} (%)	5.87
	β (°)	125.190(8)					χ^2 (%)	1.97
Ir1	U_{iso} (Å^2)	0.0173(4)	Se2	U_{iso} (Å^2)	= U_{iso}(Se1)	Pb1	U_{iso} (Å^2)	0.0214(5)
	x	0.3670(2)		*x*	0.2200(5)		occ	0.16667
	z	0.0422(3)		*z*	0.5924(6)		*x*	0.498(3)
Ir2	U_{iso} (Å^2)	= U_{iso}(Ir1)	Se3	U_{iso} (Å^2)	= U_{iso}(Se1)		*y*	0.345(2)
	x	0.8454(2)		*x*	0.0956(4)		*z*	0.462(2)
	z	0.6749(3)		*z*	0.0655(7)	Pb2	U_{iso} (Å^2)	= U_{iso}(Pb1)
Se1	U_{iso} (Å^2)	0.0150(4)	Se4	U_{iso} (Å^2)	= U_{iso}(Se1)		occ	0.16667
	x	0.1756(5)		*x*	0.4638(5)		*x*	0.030(1)
	z	0.8503(6)		*z*	0.7227(7)		*z*	0.509(6)

4.3 Results and Discussion

4.3.1 Structure of $PbIr_4Se_8$

Figure 4.1a shows the room-temperature laboratory PXRD data for $PbIr_4Se_8$ with a corresponding Rietveld refinement using spacegroup *C*2/*m*(12). Crystallographic parameters are shown in Table 4.1. Additional spacegroups were tested, and though Hamilton *R* ratio tests[12] preferred a lower symmetry *C*2(5) cell with 90% confidence, χ^2 ratios[13] only had 60% confidence for the *C*2

cell, hence the higher symmetry, $C2/m$, was chosen. Additionally, tests using ADDSYM in PLATON[96] did not find any additional symmetry.

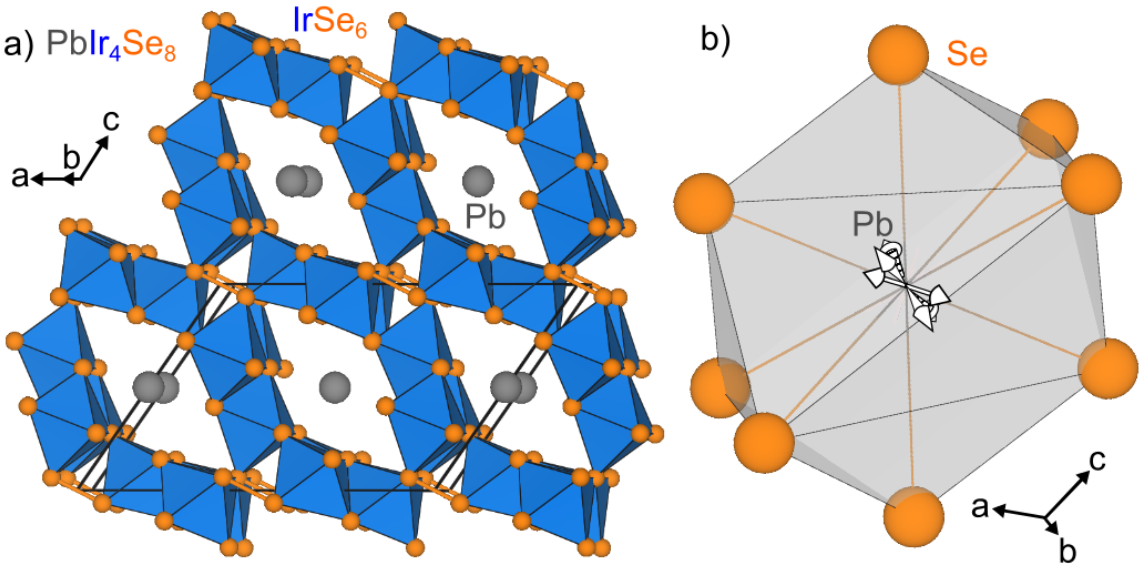

Figure 4.2: a) The $PbIr_4Se_8$ distorted-Hollandite structure. Pb positions shown are an average of sites. **b)** The $PbSe_8$ dual gyrobifastigium highlighting the direction and magnitude of the modeled Pb displacement. Pb shown in grey, Se in orange, and $IrSe_6$ octahedra in blue.

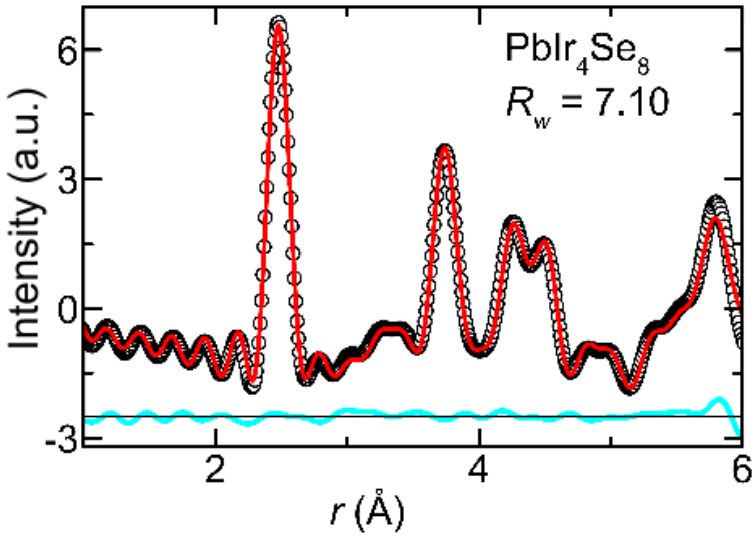

Figure 4.3. X-ray Pair Distribution analysis on $PbIr_4Se_8$ using the displaced Pb Model.

SAED patterns, oriented close to the [$\overline{12}$ $\overline{5}$ 39] direction and along the [0 0 1] direction, are shown in Figures 4.1b and 4.1c respectively for $PbIr_4Se_8$, while the inset displays the respective perpendicular planes. The [$\overline{4}$ $\overline{2}$ 15] direction, in Figure 4.1b, displays diffuse scattering, or streaking, in the [$\overline{11}$ 1 4] direction. This SAED pattern is an example of the collected tilt series, which also displays streaking in the [$\overline{3}$ 0 1] and [6 0 1] directions. The SAED pattern in Figure 4.1c contains (0 *k* 0) reflections, however the perpendicular direction does not consist of (*h* 0 0) reflections alone. This is because the plane perpendicular to the [0 0 1] direction (*c**) is not equivalent to the (0 0 1) plane, thus it is expected that the [0 0 1] direction has (0 *k* 0) reflections perpendicular to (5*h* 0 2*h*) reflections. The lattice parameters from SAED are within 10% different of those reported in Table 4.1. The streaking in some SAED patterns, however, hint at disorder within the structure.

The proposed structure of $PbIr_4Se_8$ is shown in Figure 4.2a, which is comprised of double chains of edge-sharing $IrSe_6$ octahedra which corner-share with other $IrSe_6$ double octahedral chains to form a framework structure containing 1-D channels. Pb resides in the 1-D channels in a $PbSe_8$ dual gyrobifastigium (di-rhombic prisms). The 1-D channels in $PbIr_4Se_8$ appear distorted in comparison to Hollandite, with Se-Se anion-anion bonding and a Se-Se bond distance of 2.50(2) Å in the smaller 1-D channels. This sort of anion-

anion bonding is well known to occur in Ir chalcogenides[75,76,78,119,124] and leads to a formal electron count of $Pb^{2+}(Ir^{3+})_4(Se_2)^{2-}(Se^{2-})_6$, which is in good agreement with bond valence sums for an average Pb position (1.94(2)), and the material exhibiting diamagnetic behavior (i.e. Ir is low-spin d^6).

Despite the model fitting all observed peaks, with no evidence of impurities, the fit is visibly imperfect, highlighted by the insets in Figure 4.1a. These insets demonstrate that while some peaks are sharp, others are appreciably broadened. This peak broadening is consistent with the streaking seen in the SAED patterns, and indicates some degree of disorder in the material, however even *P*1 LeBail refinements do not visibly, or statistically, improve the fit. Additionally occupancies refined within 2% of nominal values and refinements which included strain (isotropic and anisotropic), anisotropic size, and anisotropic thermal parameters did not statistically improve the fit. The structure in Figure 4.2a gives a clue for this disorder, as the Pb site is in the center of large 1-D channels. Given the large size of these channels, and that even the shortest Pb-Se distance is greater than 3 Å, it is not surprising that there would be disorder on these sites. Likewise, Pb is well known to be stereochemically active from lone-pair effects,[125,126] which leads to disorder. This disorder would give rise to not only streaking in certain SAED patterns, but also would appreciably broaden any reflections whose intensities result from mainly Pb, while reflections resulting mainly from Ir or Se would not be affected. This same type

of peak broadening was also seen in the PXRD data for the Hollandite $Rb_{0.68}Ir_4O_8$, which has disorder on the Rb site.[118]

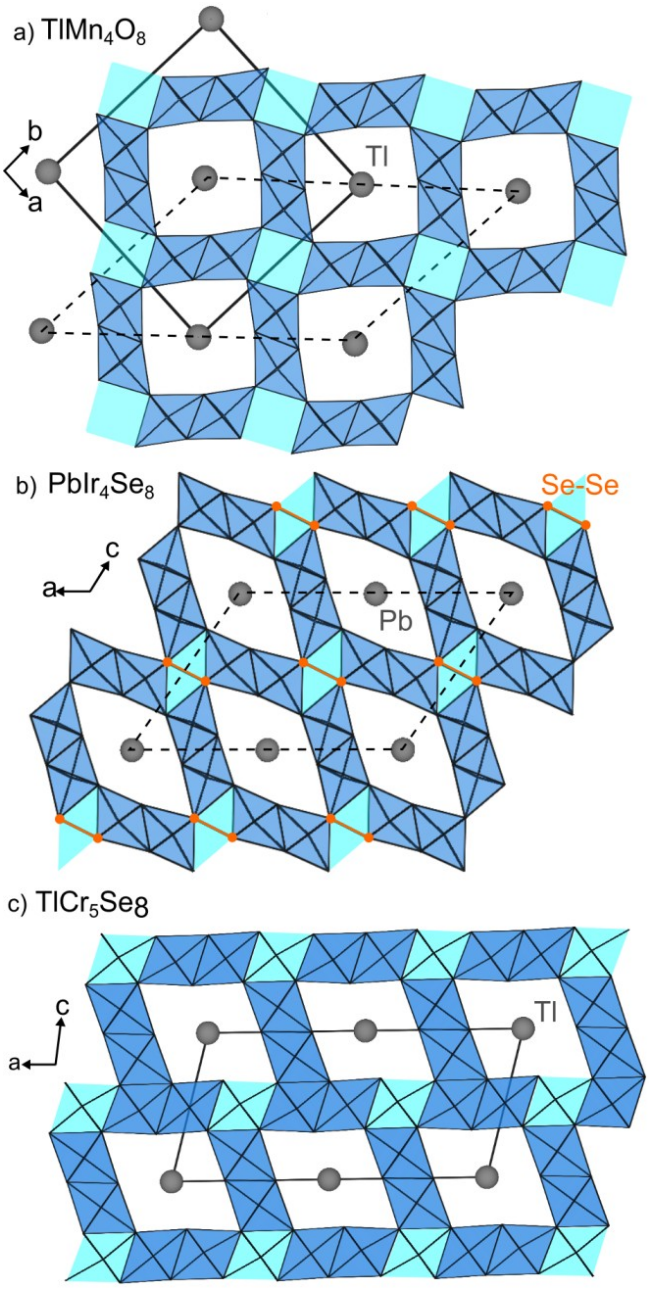

Figure 4.4: a) The MnO_2 hollandite structure ($TlMn_4O_8$), which contains both large 1-D channels occupied by cations (Tl) and smaller, empty 1-D channels. **b)** The $PbIr_4Se_8$ structure with Pb in large, distorted 1-D channels, and Se-Se anion-anion bonding in small 1-D channels. **c)** The $TlCr_5Se_8$ pseudo-Hollandite structure. Here the large 1-D channels are occupied by Tl while the small

channels are occupied by Cr. Blue shading represents TCh_6 octahedra, light blue shading highlights the small 1-D channels, and dashed lines indicate alternative, comparative unit cells.

Table 4.2: Unit cell parameters and ratios of Hollandites, pseudo-Hollandites, and the new distorted-Hollandite for comparison. Ideal ratios are derived for a closest-packing model.

	a(Å)	*b*(Å)	*c* (Å)	*β* (°)	*a/b*	*c/a*
pseudo-Hollandite						
TlV_5S_8[116]	17.465	3.301	8.519	103.94	5.29	0.488
$TlTi_5Se_8$[116]	18.773	3.583	9.1065	104.13	5.24	0.485
$Rb_{0.62}Cr_5Te_8$[127]	20.367	3.902	9.605	104.39	5.22	0.472
Ideal[116]				**103.26**	**5.10**	**0.484**
Hollandite[a]						
Mn_4O_8[112]	13.842	2.865	9.788	133.82	4.83	0.707
$Ba_{0.7}Sn_{2.6}Cr_{1.4}O_8$[116]	14.728	3.108	10.012	134.37	4.47	0.680
$Nd_{2/3}Mo_4O_8$[114]	13.999	2.940	9.899	134.68	4.76	0.707
KRu_4O_8[115]	13.953	3.131	9.866	133.63	4.46	0.707
$Rb_{0.68}Ir_4O_8$[118]	14.284	3.149	10.100	133.67	4.54	0.707
Ideal[116]				**133.31**	**5.20**	**0.680**
distorted-Hollandite						
$PbIr_4Se_8$[this work]	15.901	3.730	11.035	125.19	4.26	0.694

[a]For direct comparison Hollandite phases are reported in a monoclinic setting (instead of tetragonal).

The most reasonable refinements of the Pb site involved Pb displacing to six possible positions, in the *xz* and *y* directions, along six of the Pb-Se directions, shown in Figure 4.2b. These directions are consistent with the directions of the observed streaking in SAED patterns. The displaced Pb sites gives an average bond valence sum of 2.04(2), which is closer to the ideal value of 2.00. The resulting atomic positions are shown in Table 4.1.

Given the streaking in SAED patterns and the imperfect Rietveld refinement, X-ray pair distribution analysis (PDF) was conducted, shown in Figure 4.3. The refined model is very similar to that for the Rietveld refinement - the only notable position difference is that of Pb1 y = 0.210(5) instead of y = 0.345(2), corresponding to a small change in the direction and magnitude of the Pb off-centering. Thermal parameters were also more reasonable with $Uiso$ = 0.00508(3) Å^2, 0.00257(3) Å^2, and 0.00943(4) Å^2 for Pb, Ir, and Se respectively. The resulting Pb displacements are shown in Figure 4.2b. Though the PDF refinement fits remarkably well at short distances, at larger r the fit is not as perfect, similar to lone-pair active $Bi_2Ti_2O_7$[128]. This is indicative of short range order and long range disorder, which is expected from the diffuse scattering seen in the SAED patterns, and $K_{1-x}Ir_4O_8$ is likely similar. Future neutron PDF studies are necessary to resolve the precise nature of this short range order.

4.3.2 Structural Similarities to Other Hollandites

The canonical Hollandite structure, α-MnO_2, shown as $TlMn_4O_8$ in Figure 4.4a, contains two separate 1-D channels of different sizes. Large 1-D channels are occupied by cations (e.g. In, Tl, Pb, alkali metals, alkaline earth metals), while smaller 1-D channels (light blue in Figure 4.4a) are empty. The distorted-Hollandite, $PbIr_4Se_8$, also contains two channels (Figure 4.4b) with the large 1-D channels occupied by Pb. $PbIr_4Se_8$ is structurally distinct from α-MnO_2 however,

as the smaller 1-D channel contains Se-Se anion-anion bonding, contracting the structure. In comparison, the pseudo-Hollandite again contains large 1-D channels occupied by cations, however the smaller 1-D channels are also occupied, but with transition metals instead (Figure 4.4c). In the case of $PbIr_4Se_8$ the anion-anion bonding in the smaller 1-D channels appears to be due to charge balancing, as non-oxide Ir-chalcogenides always appear to maintain Ir^{3+}, from IrS_2, $IrSe_2$, $IrTe_2$, to Ir_2SnSe_5, and more. [75,76,78,119,124] These all have analogous portions of MnO_2 polymorphs, coupled with anion-anion bonding. The pseudo-Hollandite is also structurally distinct due to charge balancing, as $TlCr_5Se_8$ contains Tl^{1+} and Cr^{3+}. If the formula unit were that of the canonical Hollandite, $TlCr_4Se_8$, Cr would instead have to be a mixture of Cr^{3+} and Cr^{4+} in order to accommodate the Tl^{1+} cation, just as the Mn oxidation state in α-MnO_2 alters upon addition of cations.

Though charge balancing alone may explain the difference in these three structures, they are also expected to be stable based on closest-packing arguments, as previously elaborated by Klepp and Boller.[116] Using closest-packing of cations and anions in the *ac* plane, as closest-packing of *T*-*Ch* octahedra in the *b*-direction, ideal lattice parameters can be determined. Though these lattice parameters vary as a function of different sized cations and anions, the ratios of lattice parameters remain roughly constant for a range of ion sizes. In Table 4.2 we make the same comparison with an expanded range of

Hollandites and pseudo-Hollandites, including our distorted-Hollandite. For a direct comparison to the pseudo-Hollandite and distorted-Hollandite, the Hollandite phases are described in a monoclinic setting, instead of their tetragonal setting, using $a_{mono} = \sqrt{2}\, a_{tetra}$, $b_{mono} = b_{tetra}$, and $c_{mono} = a_{tetra}$ (shown as dashed line in Figure 4.4a). The pseudo-Hollandite unit cells are in excellent agreement with the ideal lattice parameter ratios, over a range of cations and anions.[116] The Hollandite unit cells have more deviation from the ideal lattice parameter ratios, but that may be due to enhanced cation mobility at room temperature.[116] Though the Hollandite unit cells deviate from the ideal lattice parameter ratios, they are in excellent agreement with each other, despite a large variety of cations and transition metals.

In comparison to the other Hollandites, the lattice parameter ratios for our distorted-Hollandite deviate even farther from the ideal Hollandite lattice parameter ratios. In particular the a/b ratio and β of $PbIr_4Se_8$ are much smaller, while the c/a ratio is still in good agreement with the ideal Hollandite lattice parameter ratios. Since the magnitude of the b-axis is defined by the closest-packing of octahedra, the significant difference is the a-axis, which is shorter than ideal. Analyzing the $PbIr_4Se_8$ structure in Figure 4.4b, the framework is compressed in the a-direction, consistent with the deviation from the ideal Hollandite case, very likely due to Se-Se anion-anion bonding. This must mean that it is energetically more favorable for iridium to maintain Ir^{3+} and introduce

anion-anion bonding, than to obey closest-packing. It is important to note that neither the KIr_4O_8 or $Rb_{0.68}Ir_4O_8$ Hollandites undergo this distortion, as it is less energetically favorable to form O-O anion-anion bonding due to the increased electronegativity of oxygen.

With this understanding, the role of the anion-anion bonding appears to be to allow iridium to be Ir^{3+}, it is just a question of whether it is energetically more favorable for the anions to share electrons, or for iridium to be in the 3+ state. In the case of sulfides, selenides, and tellurides, it appears that it is universally more favorable for Ir to be Ir^{3+} with anion-anion bonding. The low-spin $5d^6$ state is exceptionally stable, thus doping such a state might incite exotic quantum behavior due to electron mobility on the anion framework, rather than changing the oxidation state of Ir^{3+} to Ir^{4+}, such as in $Ir_{1-x}M_xTe_2$ (M = Pd or Pt),[79–82] which host superconductivity.

These models also explain why the $M_xIr_4O_8$ Hollandites are metallic and paramagnetic,[113,118] while $PbIr_4Se_8$ is insulating and diamagnetic. The difference between these compounds is the oxidation state of iridium; in MIr_4O_8 iridium is in the $Ir^{3.75+}$ state, while in $PbIr_4Se_8$ iridium is in the Ir^{3+} state. Ir^{3+} is comprised of low-spin $5d^6$, with all of the t_{2g} orbitals filled, while a low-spin $Ir^{3.75+}$ would have two filled t_{2g} orbitals, and a degenerate t_{2g} orbital with unpaired electrons, giving rise to paramagnetic and metallic behavior as observed in MIr_4O_8 compounds.

Most Rietveld refinements for Hollandite polymorphs (pseudo-Hollandites, Cryptomelane, Priderite, Psilomelane) which contains cations refines these cations to either significantly large isotropic thermal parameters, or highly anisotropic thermal parameters.[105–118,127,129,130] Some studies have analyzed these in great detail, from lone-pair displacements in $InCr_5S_8$ in purely the *b* direction,[129] to theoretical investigations demonstrating it is more energetically favorable for Li to displace in the *ac* direction in $LiMnO_2$.[131] Each compound appears to have its own degree of cation disorder, but the literature seems to show that both displacements due to smaller cations in large channels, and lone-pair effects are possible; and both in the *b* and *ac* directions. This means that our model, which displaces Pb in both the *b* and *ac* directions, is likely realistic for our system, with the displacement being caused by a combination of lone-pair effects and the size of the channels. Though it would be ideal to characterize this new material with a metal in the channel that does not displace, it is no small challenge to find a metal with no lone-pair activity, is appropriately sized, and forms the same structure.

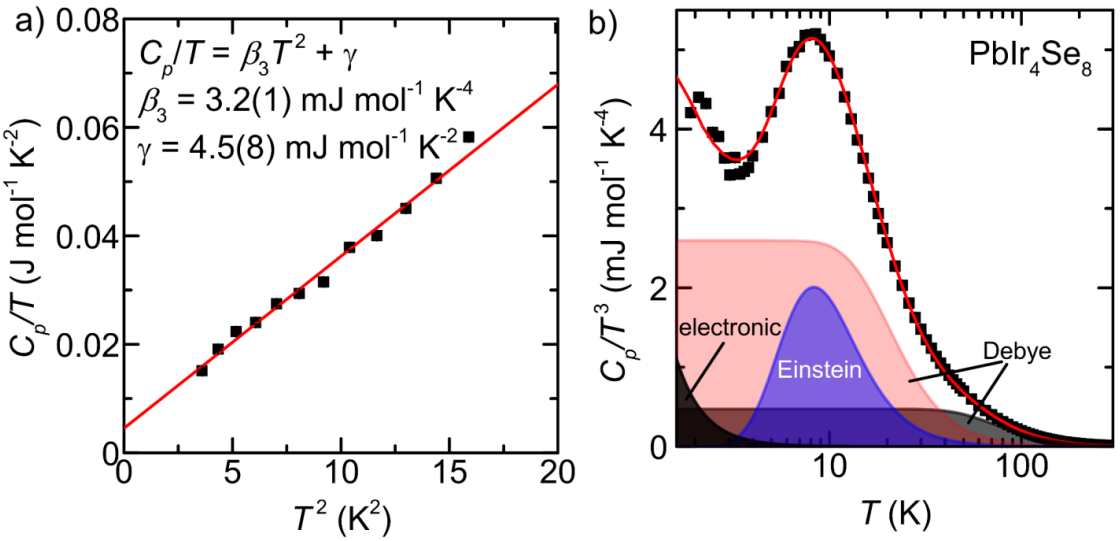

Figure 4.5: a) Heat capacity over temperature versus temperature squared. A non-zero Sommerfeld coefficient (γ) is seen. **b)** Heat capacity over temperature cubed versus temperature demonstrates an Einstein-like mode is clearly seen. Data is shown as black squares, with red lines as fits for both.

4.3.3 Heat Capacity

Resulting heat capacity data for $PbIr_4Se_8$ is shown in Figures 4.5a and 4.5b. Figure 4.5a shows a plot of C_p/T vs T^2, with a linear fit to $C_p/T = \beta_3 T^2 + \gamma$, a low-temperature approximation, where β_3 represents the phonon contribution, and γ, the Sommerfeld coefficient, represents the electronic heat capacity. The value of γ = 4.5(8) mJ mol^{-1} K^{-2} indicates a small, non-zero density of states of the Fermi level, due to some small number of states at the Fermi level. Although occupancies refined with 2% of nominal values, the structural distortion could obfuscate Se or Pb vacancies, which are common and would explain the non-zero Sommerfeld coefficient. Alternatively this could be due to the Fermi level lying on the edge of a valence band. Figure 4.5b shows the heat capacity for $PbIr_4Se_8$ as C_p/T^3 vs log T to highlight acoustic and optic phonon modes.[132] Plotted this way

Einstein (optic) modes appear to peak while Debye (acoustic) modes increase upon cooling until becoming constant. The data was fit by a model with one Einstein and two Debye modes, as well as an electronic contribution:

$$C_p/T^3 = E\ (\theta_E, T)/T^3 + D1\ (\theta_{D1}, T)/T^3 + D2\ (\theta_{D2}, T)/T^3 + \gamma/T^2$$

where θ_E is the Einstein temperature and θ_D is the Debye temperature. The Einstein model approximates an optic mode by:

$$E(\theta_E, T) = \ 3sR\left(\frac{\theta_E}{T}\right)^2 \frac{\exp(\theta_E/T)}{[\exp\ (\theta_E/T) - 1]^2}$$

While the Debye model approximates an acoustic mode by:

$$D(\theta_D, T) = \ 9sR\left(\frac{T}{\theta_D}\right)^3 \int_0^{\theta_D/T} \frac{(\theta/\mathrm{T})^4\ \exp(\theta/T)}{[\exp\ (\theta/T) - 1]^2} d\frac{\theta}{T}$$

where s is the oscillator strength and R is the molar Boltzmann constant.[2] This model appears to be in excellent agreement with the data in Figure 4.5b, and each of the separate contributions are shown. An initial fit was attempted using the Debye temperature calculated from β_3, however this severely under-fit the data and a second Debye mode was added. The final fit parameters were s_{D1} = 11.61(4), θ_{D1} = 363(2) K, s_{D2} = 1.36(4), θ_{D2} = 100.6(9) K, s_E = 0.259(4), and θ_E = 41.0(2) K, where the total number of oscillators adds up to 13.2(1), in good agreement with the total number of atoms per formula unit. The large Einstein

mode is due to the Pb disorder, as similar effects are commonly seen in the literature.[125,126]

Table 4.3: Comparison of Einstein modes and displacements (δ) for compounds with lone-pair active cations.

	s	*E* (meV)	δ (Å)
$PbTiO_3$[36]	0.4(1)	5.5(7)	0.474[43]
	1.5(5)	8(1)	
$Pb_2Ru_2O_{6.5}$[35]		6(2)	0.020(4)
$PbIr_4Se_8$[a]	0.259(4)	3.53(2)	0.55(15)
$InCr_5S_8$[37]			0.363

[a]This work.

Table 4.3 shows a comparison of both Einstein mode and physical displacement magnitude for a variety of lone-pair active compounds. The Einstein energy among the pyrochlore $Pb_2Ru_2O_{6.5}$, the perovskite $PbTiO_3$, and the distorted-Hollandite $PbIr_4Se_8$ all have the same magnitude, though the value for $PbIr_4Se_8$ is roughly half. This could be due to the large 1-D channels, which would entropically decrease the Pb order, verifying that cation displacements in Hollandite polymorphs are not due to lone-pair effects alone. The magnitude of displacements across the perovskite $PbTiO_3$, distorted-Hollandite $PbIr_4Se_8$, and pseudo-Hollandite $InCr_5Se_8$ are in rough agreement as well, as all of these structure types have "pockets" large enough to allow this displacement, unlike the pyrochlore $Pb_2Ru_2O_{6.5}$, which has a much smaller displacement due to the significantly different structure.

4.3.4 Band Structure

The disorder of the Pb site precludes direct computation of the band structure. However, a reasonable approximation can be derived by computing the band structure for the host Ir_4Se_8 framework, and then applying the rigid band approximation to shift the Fermi level consistent with the inclusion of one Pb^{2+} per formula unit. Such a band structure for Ir_4Se_8 is shown in Figure 4.6a, plotted using the Brillouin zone definition in Figure 4.6b. Introducing Pb^{2+} into the Ir_4Se_8 framework shifts the Fermi level up, donating two electrons per formula unit. The dotted line in Figure 4.6a displays the new location of the Fermi level, derived from integrating the density of states. As γ is proportional to the number of states at the Fermi level, the proposed Fermi level position is in good agreement with the small, non-zero γ, both due to the small number of states, and the curvature of the band. The 0.75(11) eV gap between the new Fermi level and the conduction band indicates semiconducting behavior which was observed experimentally as charging effects in the TEM beam.

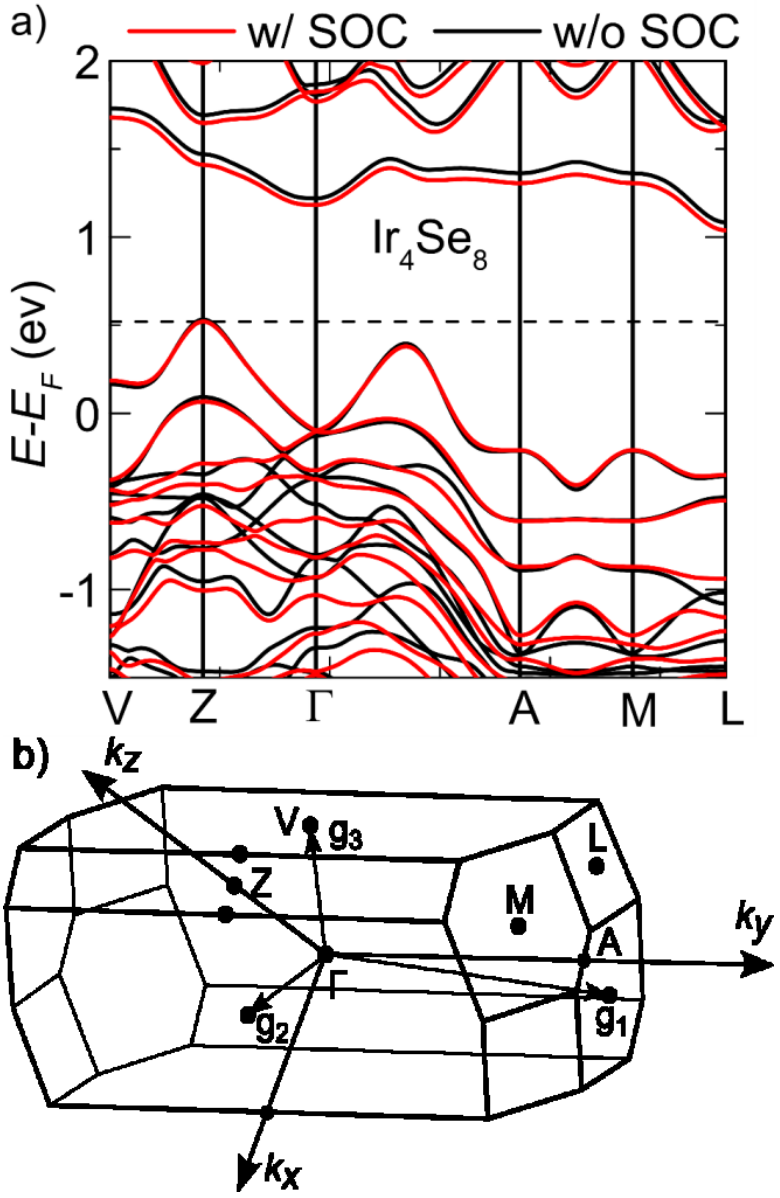

Figure 4.6. **a)** Band structure for the Ir_4Se_8 cages, without Pb, both with and without spin-orbit coupling (SOC). Dotted line shows the location of the Fermi level when Pb donates two electrons per formula unit. **b)** Brillouin zone for $PbIr_4Se_8$.

4.3.5 Deintercalation/Intercalation

Due to the large 1-D channels that Pb resides in, it was thought that it might be possible to deintercalate Pb and replace it with Li to make $PbIr_4Se_8$ a more attractive battery material. Figure 4.7 demonstrates a diffraction pattern for a

partially deintercalated $PbIr_4Se_8$. Occupancies for Pb appear to be close to 0.5, while all other occupancies remain within error of nominal. Deintercalations using iodide instead of bromide led to removal of $IrSe_2$ as well. Though the model's fit to the data in Figure 4.7 is not perfect, no secondary phases are seen and no peaks disappear, though several peaks become severely under-fit. This is either due to more Pb disorder, or anisotropic interruptions in the crystalline lattice due to the deintercalation process.

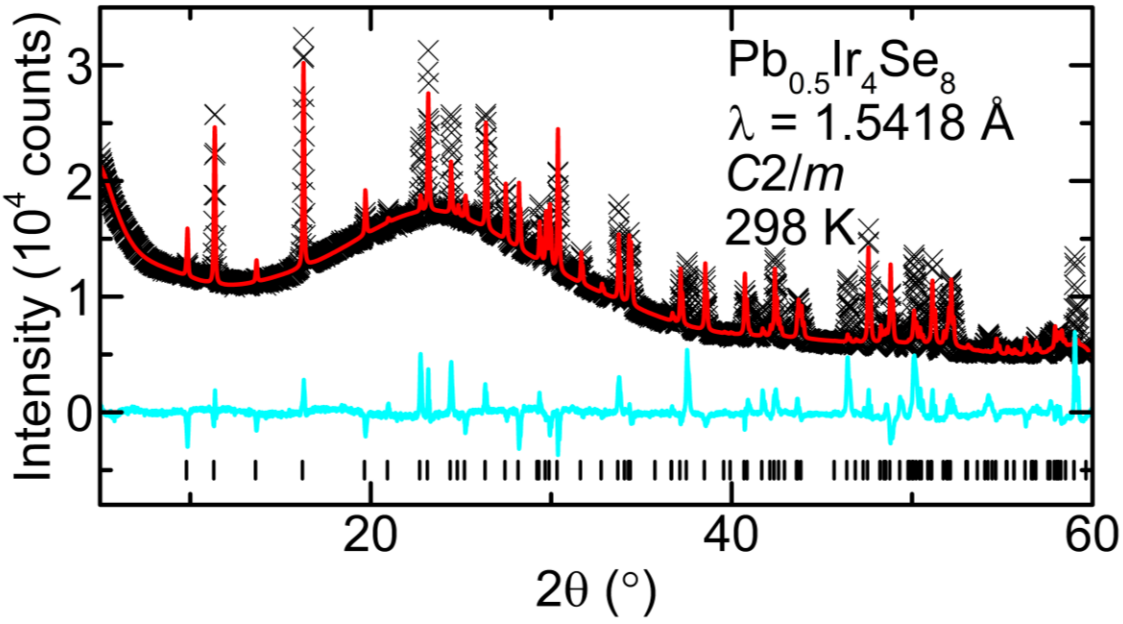

Figure 4.7: Laboratory X-ray diffraction data for deintercalated $PbIr_4Se_8$ at room temperature. Data is shown as black X's, fit in red, difference curve in cyan, and peak locations as black tick marks. Though the model fits poorly in many areas, there is no evidence for secondary phases.

In order to determine how successful the deintercalation process was, magnetization measurements were also conducted on the $Pb_{0.5}Ir_4Se_8$, shown in Figure 4.8 with the parent structure $PbIr_4Se_8$. As expected, paramagnetic behavior is observed in $Pb_{0.5}Ir_4Se_8$ due to partial Pb deintercalation, as no

secondary phases are seen. This makes sense as the removal of Pb from $PbIr_4Se_8$ would destabilize the $PbSe_8$ dual gyrobifastigium and would introduce unpaired electrons in the 1-D channels.

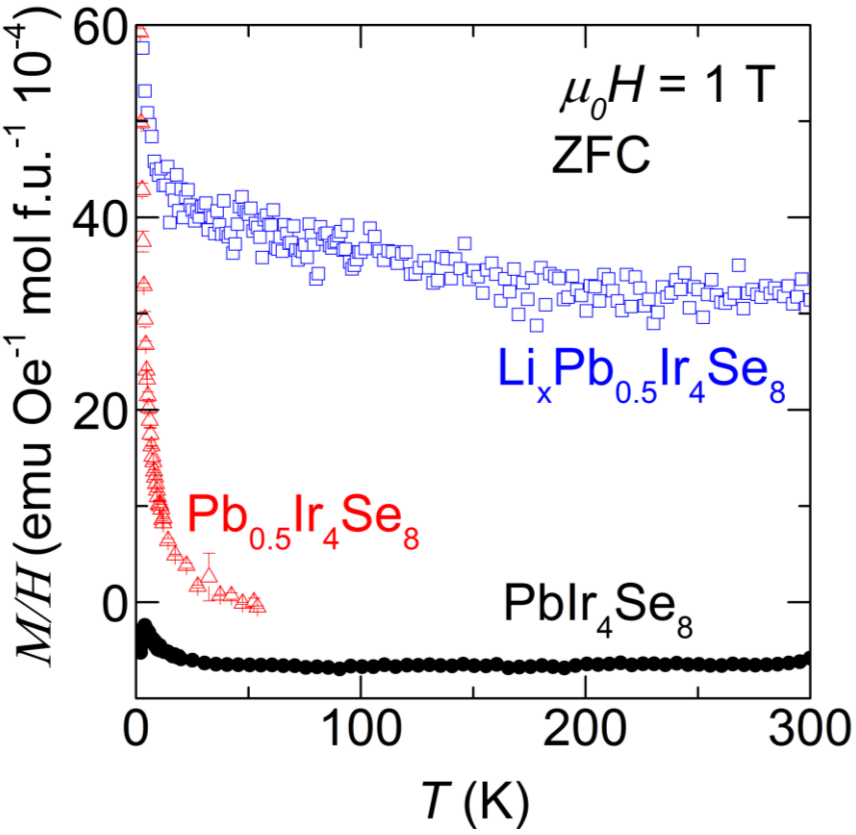

Figure 4.8: Magnetization for Li intercalated $Li_xPb_{0.5}Ir_4Se_8$ (blue squares), deintercalated $Pb_{0.5}Ir_4Se_8$ (red triangles), and parent compound $PbIr_4Se_8$ (black circles.

Intercalation reactions were also conducted with similar results. No impurity phases were seen to be present, the Pb occupancy appears close to 0.5, and all other occupancies appear nominal. The introduction of Li into $Pb_{0.5}Ir_4Se_8$ introduces more strongly paramagnetic behavior, demonstrated by Figure 4.8. The exact amount of lithium introduced into the structure is unknown, as is the

exact amount of Pb lost. Further investigations, such as Li NMR and elemental diffraction spectroscopy, will be conducted to confirm exact atomic ratios.

Both the intercalated, deintercalated, and parent phases all contain a Curie-tail at low temperatures, indicated of some small number of defects. This confirms the non-zero Sommerfeld coefficient. The defects are likely due to some small number of Se vacancies.

4.4 Conclusion

The new $PbIr_4Se_8$ distorted-Hollandite is reported. It is a network of corner- and edge-sharing $IrSe_6$ octahedra, Se-Se anion-anion bonding in small 1-D channels, and Pb in large 1-D channels. Laboratory X-ray data and selected area electron diffraction demonstrate that the material is well described by spacegroup $C/2m(12)$, however there is evidence for Pb disorder due to lone-pair effects and the large size of the 1-D channels. An Einstein mode in heat capacity measurements further confirms the Pb disorder, due to a small, non-zero Sommerfeld coefficient of $\gamma = 4.5(8)$ mJ mol^{-1} K^{-2}. Band structure calculations further confirm the small non-zero γ, and demonstrate $PbIr_4Se_8$ is a semiconductor, with a band gap of 0.76(11) eV. The distorted-Hollandite $PbIr_4Se_8$ is structurally similar to other Hollandite polymorphs, but the 1-D channels are distorted to allow for Se-Se anion-anion bonding in the smaller 1-D channels, which accommodates Ir to be Ir^{3+}, despite deviation from close-packing. This is

consistent with other non-oxide Ir chalcogenides which also exhibit anion-anion bonding, as well as diamagnetic and insulating behavior. Given the disorder of the Pb in the 1-D channels, $PbIr_4Se_8$ is a good candidate for thermoelectric materials. Similarly, as $PbIr_4Se_8$ is a Hollandite polymorph, it would also be a candidate for battery materials, especially given that the Se-Se anion-anion bonding may make the framework Ir_4Se_8 more stable. Lastly, the band gap of ~1 eV makes $PbIr_4Se_8$ a candidate material for photovoltaics if it can be prepared in thin film form, though the cost and toxicity make this unlikely.

4.5 Acknowledgements

This work was supported by NSF, Division of Materials Research, Solid State Chemistry, CAREER grant under Award DMR-1253562. BAT also acknowledges useful discussions with K. J.T. Livi. Intercalation/deintercalation reactions were conducted by Z. A. Kelly and J. Chamorro. The research also benefited from beamline 11-ID-B of the Advanced Photon Source, a U.S. Department of Energy (DOE) Office of Science by Argonne National Laboratory under Contract No. DE-AC02-06CH11357. We also acknowledge K.E. Arpino for technical assistance.

References

(1) Pippard, A. B. *Magnetoreistance in Metals*; Cambridge University Press: Cambridge, 1989.

(2) Tari, A. *The Specific Heat of Matter at Low Temperatures*; Imperial College Press: London, 2003.

(3) Tritt, T. M. *Thermal Conductivity: Theory, Properties, and Applications*; Kluwer Academic/Plenum Publishers: New York, 2004.

(4) Levine, I. N. *Quantum Chemistry*, 6th ed.; Pearson Education: London, 2009.

(5) Ashcroft, N. W.; Mermin, N. D. *Solid State Physics*; Saunders College Publishing: Philadelphia, 1976.

(6) Williams, D. B.; Carter, B. C. *Transmission Electron Microscopy*; Spring Science: New York, 2009.

(7) McQueen, T. M. Materials Lifecycle https://occamy.chemistry.jhu.edu/research/index.php (accessed Jun 1, 2016).

(8) Wiegers, G. . *Prog. Solid State Chem.* **1996**, *24* (1-2), 1–139.

(9) Anderson, P. W. *Science (80-.).* **1972**, *177* (4047), 393–396.

(10) H.K., O. *Commun. Phys. Lab. Univ. Leiden. Suppl.* **1911**, *29*.

(11) Bardeen, J.; Cooper, L. N.; Schrieffer, J. R. *Phys. Rev.* **1957**, *108* (5), 1175–1204.

(12) Hamilton, W. C. *Acta Cryst.* **1965**, *18*, 502–510.

(13) Giacovazzo, C.; Monaco, H. L.; Artioli, G.; Viterbo, D.; Milanesio, M.; Ferraris, G.; Gilli, G.; Gilli, P.; Zanotti, G.; Catti, M. *Fundamentals of Crystallography Third Edition*; 2011.

(14) Toby, B. H. 2015, p Private Communication.

(15) Kohler, M. *Ann. Phys.* **1938**, *26* (38), 630.

(16) Morosan, E.; Zandbergen, H. W.; Dennis, B. S.; Bos, J. W. G.; Onose, Y.; Klimczuk, T.; Ramirez, a. P.; Ong, N. P.; Cava, R. J. *Nat. Phys.* **2006**, *2* (8), 544–550.

(17) Kanatzidis, M. G. *Acc. Chem. Res.* **2005**, *38* (4), 361–370.

(18) Lin, Q.; Smeller, M.; Heideman, C. L.; Zschack, P.; Koyano, M.; Anderson, M. D.; Kykyneshi, R.; Keszler, D. a.; Anderson, I. M.; Johnson, D. C. *Chem. Mater.* **2010**, *22* (3), 1002–1009.

(19) Kim, J. H.; Song, Y. J.; Rhyee, J. S.; Kim, B. S.; Park, S. D.; Lee, H. J.; Shin, J. W. *Phys. Rev. B - Condens. Matter Mater. Phys.* **2013**, *87* (22), 1–6.

(20) Wilson, J. A.; Yoffe, A. D. *Advances in Physics*. 1969, pp 193–335.

(21) Wilson, J. A.; Di Salvo, F. J.; Mahajan, S. *Adv. Phys.* **1975**, *24* (2), 117–201.

(22) Williams, P. M. *Crystallography and Crystal Chemistry of Materials with Layered Structures, Physics and Chemistry of Materials with Layered Structures Vol. 2*; Levy, F. A., Ed.; D. Riedel: Boston, 1976.

(23) Lieth, R. M. .; Terhell, J. C. J. M. *Preparation and Crystal Growth of Materials with Layered Structures, Physics and Chemistry of Materials with Layered Structures Vol. 1*; Lieth, R. M. ., Ed.; D. Reidel: Boston, 1977.

(24) Oosawa, Y.; Gotoh, Y.; Akimoto, J.; Tsunoda, T.; Sohma, M.; Onoda, M. *Jpn. J. Appl. Phys.* **1992**, *31* (2-8A), L1096–L1099.

(25) Roesky, R.; Meerschaut, A.; Rouxel, J.; Chen, J. *Zeitschrift f Anorg. und Allg. Chemie* **1993**, *619* (1), 117–122.

(26) Wiegers, G. a.; Meerschaut, A. *Mater. Sci. Forum* **1992**, *100-101*, 101–172.

(27) Ren, Y., Meetsma, A., Spijkerman, A., Weigers, G. A. *Zeitschrift für Krist.* **1997**, *212*, 586–592.

(28) Giang, N.; Xu, Q.; Hor, Y. S.; Williams, a. J.; Dutton, S. E.; Zandbergen, H. W.; Cava, R. J. *Phys. Rev. B - Condens. Matter Mater. Phys.* **2010**, *82* (2), 1–5.

(29) Di Salvo, F. J.; Moncton, D. E.; Waszczak, J. V. *Phys. Rev. B* **1976**, *14* (10), 4321–4328.

(30) Bachrach, R.; Skibowski, M.; Brown, F. *Phys. Rev. Lett.* **1976**, *37* (1), 40–42.

(31) Woo, K. C.; Brown, F. C.; McMillan, W. L.; Miller, R. J.; Schaffman, M. J.; Sears, M. P. *Phys. Rev. B* **1976**, *14* (8), 3242–3247.

(32) Li, G.; Hu, W. Z.; Qian, D.; Hsieh, D.; Hasan, M. Z.; Morosan, E.; Cava, R. J.; Wang, N. L. *Phys. Rev. Lett.* **2007**, *99* (2), 2–5.

(33) Ishioka, J.; Liu, Y. H.; Shimatake, K.; Kurosawa, T.; Ichimura, K.; Toda, Y.; Oda, M.; Tanda, S. *Phys. Rev. Lett.* **2010**, *105* (17), 1–4.

(34) Castellan, J.-P.; Rosenkranz, S.; Osborn, R.; Li, Q.; Gray, K. E.; Luo, X.; Welp, U.; Karapetrov, G.; Ruff, J. P. C.; van Wezel, J. *Phys. Rev. Lett.* **2013**, *110* (19), 196404.

(35) Wilson, J. A. *Solid State Commun.* **1977**, *22* (9), 551–553.

(36) Zunger, A.; Freeman, a. J. *Phys. Rev. B* **1978**, *17* (4), 1839–1842.

(37) Cercellier, H.; Monney, C.; Clerc, F.; Battaglia, C.; Despont, L.; Garnier, M. G.; Beck, H.; Aebi, P.; Patthey, L.; Berger, H.; Forró, L. *Phys. Rev. Lett.* **2007**, *99* (14), 1–4.

(38) Whangbo, M. H.; Canadell, E. *J. Am. Chem. Soc.* **1992**, *114* (24), 9587–9600.

(39) Suzuki, N.; Yamamoto, A.; Motizuki, K. *J. Phys. Soc. Japan* **1985**, *54* (12), 4668–4679.

(40) Motizuki, K.; Suzuki, N.; Yoshida, Y.; Takaoka, Y. *Solid State Commun.* **1981**, *40* (11), 995–998.

(41) Hughes, H. P. *J. Phys. C Solid State Phys.* **2001**, *10* (11), L319–L323.

(42) Morosan, E.; Wagner, K. E.; Zhao, L. L.; Hor, Y.; Williams, a. J.; Tao, J.; Zhu, Y.; Cava, R. J. *Phys. Rev. B* **2010**, *81* (9), 1–5.

(43) Heideman, C.; Nyugen, N.; Hanni, J.; Lin, Q.; Duncombe, S.; Johnson, D. C.; Zschack, P. *J. Solid State Chem.* **2008**, *181* (7), 1701–1706.

(44) Lin, Q.; Heideman, C. L.; Nguyen, N.; Zschack, P.; Chiritescu, C.; Cahill, D. G.; Johnson, D. C. *Eur. J. Inorg. Chem.* **2008**, *1* (15), 2382–2385.

(45) Moore, D. B.; Beekman, M.; Disch, S.; Zschack, P.; Häusler, I.; Neumann, W.; Johnson, D. C. *Chem. Mater.* **2013**, *25* (12), 2404–2409.

(46) Atkins, R.; Moore, D. B.; Johnson, D. C. *Chem. Mater.* **2013**, *25* (9), 1744–1750.

(47) Oosawa, Y.; Gotoh, Y.; Onoda, M. *Adv. Supercond. II Proc. 2nd Int. Symp. Supercond.* **1989**, 193–196.

(48) Gotoh, Y.; Onoda, M.; Uchida, K.; Tanaka, Y.; Iida, T.; Hayakawa, H.; Oosawa, Y. *Chem. Lett.* **1989**, No. 9, 1559–1562.

(49) Massa, E.; Mana, G.; Kuetgens, U.; Ferroglio, L. *New J. Phys.* **2009**, *11*.

(50) Momma, K.; Izumi, F. *J. Appl. Crystallogr.* **2008**, *41* (3), 653–658.

(51) van Smaalen, S.; Meetsma, A.; Wiegers, G. A.; de Boer, J. L. *Acta Crystallogr. Sect. B Struct. Sci.* **1991**, *47* (3), 314–325.

(52) Onoda, M.; Kato, K.; Gotoh, Y.; Oosawa, Y. *Acta Crystallogr. Sect. B Struct. Sci.* **1990**, *46* (4), 487–492.

(53) Goldschmidt, G. M. *Skr. Utg. av det Nor. Videnskaps-Akademi i Oslo 1 Mat.* **1927**, *8*, 1–159.

(54) Goldschmidt, V. M. *Skr. Utg. av det Nor. Videnskaps-Akademi i Oslo 1 Mat. Klasse* **1927**, *8*, 1–156.

(55) Rouxel, J.; Meerschaut, a.; Wiegers, G. a. *J. Alloys Compd.* **1995**, *229* (1), 144–157.

(56) Fang, C. M.; de Groot, R. A.; Haas, C. *Phys. Rev. B* **1997**, *56* (8), 4455–4463.

(57) Weber, F.; Rosenkranz, S.; Castellan, J. P.; Osborn, R.; Karapetrov, G.; Hott, R.; Heid, R.; Bohnen, K. P.; Alatas, a. *Phys. Rev. Lett.* **2011**, *107* (26), 1–5.

(58) Holt, M.; Zschack, P.; Hong, H.; Chou, M. Y.; Chiang, T. C. *Phys. Rev. Lett.* **2001**, *86* (17), 3799–3802.

(59) Collan, H.K., Krusius, M., Pickett, G.R. *Phys. Rev. B* **1970**, *1* (7), 2888–2895.

(60) Bachhuber, F.; Krach, A.; Furtner, A.; Söhnel, T.; Peter, P.; Rothballer, J.; Weihrich, R. *J. Solid State Chem.* **2015**, *226*, 29–35.

(61) Bachhuber, F.; Rothballer, J.; Söhnel, T.; Weihrich, R. *Comput. Mater. Sci.* **2014**, *89*, 114–121.

(62) Fleurial, J.-P.; Caillat, T.; Borshchevsky, A. *XVI ICT "97. Proc. ICT"97. 16th Int. Conf. Thermoelectr. (Cat. No.97TH8291)* **1997**, 1–11.

(63) Uher, C. In *Chemistry, physics, and materials science of thermoelectric materials; beyond bismuth telluride*; 2003; pp 121–146.

(64) Zabel, M.; Wandinger, S.; Range, K. *Zeitschrift für Naturforsch. B* **1979**, *34b*, 238–241.

(65) Jackeli, G.; Khaliullin, G. *Phys. Rev. Lett.* **2009**, *102* (1), 017205.

(66) Shitade, A.; Katsura, H.; Kuneš, J.; Qi, X.-L.; Zhang, S.-C.; Nagaosa, N. *Phys. Rev. Lett.* **2009**, *102* (25), 256403.

(67) Gretarsson, H.; Clancy, J. P.; Liu, X.; Hill, J. P.; Bozin, E.; Singh, Y.; Manni, S.; Gegenwart, P.; Kim, J.; Said, A. H.; Casa, D.; Gog, T.; Upton, M. H.; Kim, H.-S.; Yu, J.; Katukuri, V. M.; Hozoi, L.; van den Brink, J.; Kim, Y.-J. *Phys. Rev. Lett.* **2013**, *110* (7), 076402.

(68) Chaloupka, J.; Jackeli, G.; Khaliullin, G. *Phys. Rev. Lett.* **2010**, *105* (2), 027204.

(69) Wallace, D. C.; Brown, C. M.; McQueen, T. M. *J. Solid State Chem.* **2015**, *224*, 28–

35.

(70) Katukuri, V. M.; Nishimoto, S.; Yushankhai, V.; Stoyanova, A.; Kandpal, H.; Choi, S.; Coldea, R.; Rousochatzakis, I.; Hozoi, L.; Brink, J. van den. *New J. Phys.* **2014**, *16* (1), 013056.

(71) Lei, H.; Yin, W.-G.; Zhong, Z.; Hosono, H. *Phys. Rev. B* **2014**, *89* (2), 020409.

(72) Rau, J. G.; Lee, E. K.-H.; Kee, H.-Y. *Phys. Rev. Lett.* **2014**, *112* (7), 077204.

(73) Andrade, E. C.; Vojta, M. *Phys. Rev. B* **2014**, *90* (20), 205112.

(74) Kimchi, I.; Analytis, J. G.; Vishwanath, A. *Phys. Rev. B* **2014**, *90* (20), 205126.

(75) Munson, R. A. *Inorg. Chem.* **1968**, *7* (2), 389–390.

(76) Jobic, S.; Deniard, P.; Brec, R.; Rouxel, J.; Drew, M. G. B.; David, W. I. F. *J. Solid State Chem.* **1990**, *89* (2), 315–327.

(77) Jobic, S.; Deniard, P.; Brec, R.; Rouxel, J.; Jouanneaux, A.; Fitch, A. N. *Zeitschrift fuer Anorg. und Allg. Chemie* **1991**, *598/599* (1), 199–215.

(78) Jobic, S.; Brec, R.; Chateau, C.; Haines, J.; Léger, J. M.; Koo, H. J.; Whangbo, M. H. *Inorg. Chem.* **2000**, *39* (19), 4370–4373.

(79) Li, L.; Qi, T. F.; Lin, L. S.; Wu, X. X.; Zhang, X. T.; Butrouna, K.; Cao, V. S.; Zhang, Y. H.; Hu, J.; Yuan, S. J.; Schlottmann, P.; De Long, L. E.; Cao, G. *Phys. Rev. B* **2013**, *87* (17), 174510.

(80) Yang, J. J.; Choi, Y. J.; Oh, Y. S.; Hogan, A.; Horibe, Y.; Kim, K.; Min, B. I.; Cheong, S.-W. *Phys. Rev. Lett.* **2012**, *108* (11), 116402.

(81) Zhou, S. Y.; Li, X. L.; Pan, B. Y.; Qiu, X.; Pan, J.; Hong, X. C.; Zhang, Z.; Fang, A. F.; Wang, N. L.; Li, S. Y. *EPL* **2013**, *104* (2), 27010.

(82) Fang, A. F.; Xu, G.; Dong, T.; Zheng, P.; Wang, N. L. *Sci. Rep.* **2013**, *3*, 1153.

(83) Ootsuki, D.; Pyon, S.; Kudo, K.; Nohara, M.; Horio, M.; Yoshida, T.; Fujimori, A.; Arita, M.; Anzai, H.; Namatame, H.; Taniguchi, M.; Saini, Naurang, L.; Mizokawa, T. *J. Phys. Soc. Japan* **2013**, *82*, 093704.

(84) Yan, W.; Pielnhofer, F.; Tragl, S. A.; Weihrich, R. *Zeitschrift für Anorg. und Allg. Chemie* **2015**, *641* (3-4), 543–548.

(85) *The ELK FP-LAPW Code, (available at http://elk.sourceforge.net)*.

(86) Fu, L.; Kane, C. L. *Phys. Rev. B - Condens. Matter Mater. Phys.* **2007**, *76* (4), 1–17.

(87) Mostofi, A. A.; Yates, J. R.; Lee, Y.-S.; Souza, I.; Vanderbilt, D.; Marzari, N. *Comput. Phys. Commun.* **2008**, *178* (9), 685–699.

(88) Kresse, G.; Furthmüller, J. *Comput. Mater. Sci.* **1996**, *6* (1), 15–50.

(89) Kresse, G. *Phys. Rev. B* **1996**, *54* (16), 11169–11186.

(90) Kresse, G.; Hafner, J. *Phys. Rev. B* **1993**, *47* (1), 558–561.

(91) Gresch, D., Soluyanov, A. A., Vanderbilt, D., Autes, G., Yazyev, O., Ceresoli, D., Troyer, M. *Prep.*

(92) Soluyanov, A. A.; Vanderbilt, D. *Phys. Rev. B* **2011**, *83* (23), 235401.

(93) Brostigen, G.; Kjekshus, A.; Astrup, E. E.; Nordal, V.; Lindberg, A. a.; Craig, J. C.

Acta Chem. Scand. **1969**, *23*, 2186–2188.

(94) Bayliss, P. *Am. Mineral.* **1982**, *67*, 1048–1057.

(95) Ramsdell, L. S. *J. Mineral. Soc. Am.* **1925**, *10* (9), 281–304.

(96) Spek, A. L. *Acta Crystallogr. Sect. D Biol. Crystallogr.* **2009**, *65* (2), 148–155.

(97) Baur, W. H. *Acta Crystallogr. Sect. B Struct. Crystallogr. Cryst. Chem.* **1976**, *32* (7), 2200–2204.

(98) Ramirez, A. P.; Kowach, G. R. *Phys. Rev. Lett.* **1998**, 4903–4906.

(99) Fritzsche, H. *Phys. Rev.* **1955**, *99* (2), 406–419.

(100) Fritzsche, H.; Lark-Horovitz, K. *Physica* **1954**, *20* (7-12), 834–844.

(101) Li, S. S. *Natl. Bur. Stand. Spec. Publ.* **1979**, *400-47*, 1–42.

(102) Mott, N. F. *Rev. Mod. Phys.* **1968**, *40* (4), 677–683.

(103) Cottingham, P.; Miller, D. C.; Sheckelton, J. P.; Neilson, J. R.; Feygenson, M.; Huq, A.; McQueen, T. M. *J. Mater. Chem. C* **2014**, *2* (17), 3238.

(104) Snyder, G. J.; Toberer, E. S. *Nat. Mater.* **2008**, *7* (2), 105–114.

(105) Rossouw, M. H.; Thackeray, M. M. *Mat. Res. Bull* **1991**, *26* (c), 463–473.

(106) Devaraj, S.; Munichandraiah, N. *J. Phys. Chem. C* **2008**, *112* (11), 4406–4417.

(107) Rossouw, M H, Liles, D C, Thackeray, M M, David, W I F, Hull, S. *Mater. Res. Bull.* **1992**, *27*, 221–230.

(108) Takahashi, H.; Raghavendra, N.; Gascoin, F.; Pelloquin, D.; Hébert, S.; Guilmeau, E. *Chem. Mater.* **2013**, *25* (9), 1809–1815.

(109) Maier, S.; Lefèvre, R.; Lin, X.; Nunna, R.; Berthebaud, D.; Hèbert, S.; Mar, A.; Gascoin, F. *J. Mater. Chem. C* **2015**, *3* (40), 10509–10517.

(110) Larson, A. M.; Moetakef, P.; Gaskell, K.; Brown, C. M.; King, G.; Rodriguez, E. E. *Chem. Mater.* **2015**, *27* (2), 515–525.

(111) Bensch, W.; Nather, C.; Helmer, O.; Ritter, C. *J. Alloys Compd.* **1999**, *290*, 41–51.

(112) Byström, A.; Byström, A. M. *Acta Cryst.* **1950**, *3*, 146–154.

(113) Bestaoui, N.; Deniard, P.; Brec, R. *J. Solid State Chem.* **1995**, *118* (2), 372–377.

(114) Tortelier, J.; Mccarroll, W. H.; Gougeon, P. *J. Solid State Chem.* **1998**, *136*, 87–92.

(115) Foo, M. L.; Lee, W. L.; Siegrist, T.; Lawes, G.; Ramirez, A. P.; Ong, N. P.; Cava, R. J. *Mater. Res. Bull.* **2004**, *39* (11), 1663–1670.

(116) Klepp, K.; Boller, H. *J. Solid State Chem.* **1983**, *48*, 388–395.

(117) Novet, T.; Wagner, M.; Jiang, M.; Johnson, D. C. *Mater. Res. Bull.* **1994**, *30* (1), 65–73.

(118) Schoop, L. M.; Krizan, J. W.; Gibson, Q. D.; Cava, R. J. *J. Solid State Chem.* **2014**, *209*, 37–41.

(119) Trump, B. A.; Tutmaher, J. A.; McQueen, T. M. *Inorg. Chem.* **2015**, *54* (24), 11993–12001.

(120) Toby, B. H.; Von Dreele, R. B. *J. Appl. Crystallogr.* **2013**, *46* (2), 544–549.

(121) Hammersley, A. P.; Svensson, S. O.; Handfland, M.; Fitch, A. N.; Hausermann, D. *High Press. Res.* **1996**, *14*, 235–248.

(122) Qiu, X.; Thompson, J. W.; Billinge, S. J. L. *J. Appl. Crystallogr.* **2004**, *37*, 678.

(123) Farrow, C. L.; Juhas, P.; Liu, J. W.; Bryndin, D.; Bozin, E. S.; Bloch, J.; Proffen, T.; Billinge, S. J. L. *J. Phyics Condens. Matter* **2007**, *19*, 335219.

(124) Jobic, S.; Evain, M.; Brec, R.; Deniard, P.; Jouanneaux, A.; Rouxel, J. *J. Solid State Chem.* **1991**, *95* (2), 319–326.

(125) Shoemaker, D. P.; Llobet, A.; Tachibana, M.; Seshadri, R. *J. Phys. Condens. Matter* **2011**, *23* (31), 315404.

(126) Melot, B. C.; Tackett, R.; O'Brien, J.; Hector, A. L.; Lawes, G.; Seshadri, R.; Ramirez, A. P. *Phys. Rev. B* **2009**, *79*, 224111.

(127) Boucher, F.; Gareh, J.; Gourdon, O.; Evain, M.; O'Connor, C. J. *J. Solid State Chem.* **1997**, *131* (2), 326–334.

(128) Shoemaker, D. P.; Seshadri, R.; Tachibana, M.; Hector, A. L. *Phys. Rev. B* **2011**, *84* (6), 064117.

(129) Petricek, S.; Boller, H.; Klepp, K. O. *Solid State Ionics* **1995**, *81*, 183–188.

(130) Post, J. E.; Von Dreele, R. B.; Buseck, P. R. *Acta Crystallogr. Sect. B Struct. Crystallogr. Cryst. Chem.* **1982**, *38* (4), 1056–1065.

(131) Tompsett, D. A.; Islam, M. S. *Chem. Mater.* **2013**, *25* (12), 2515–2526.

(132) Zeller, R. C.; Pohl, R. O. *Phys. Rev. B* **1971**, *4* (6), 2029–2041.

Biography

Benjamin Allen Trump was born to Sally and Jack Trump in Reading, Pennsylvania on February 5th 1984. Raised in Womelsdorf, Pennsylvania, Ben graduated from Conrad Weiser High School in May of 2002. In September 2002 he attended Bucknell University as a chemical engineer. In 2006 he took a health withdrawal and attended Reading Area Community College part-time in September 2007, then later attending Kuztown University of Pennsylvania full-time in May 2009. Ben graduated from Kutztown University with a degree in Secondary Education Chemistry in May 2011. While at Kutztown University, Ben studied air-free Schlenk chemistry for CO_2 activation reactions under the guidance of Professor Douglas Swartz. In August 2001 Ben started his graduate studies under the tutelage of Professor Tyrel M. McQueen Ben's dissertation research focused on the design and discovery of new materials with strong electron-electron correlations. Ben earned his Master of Arts degree in June 2013 and his Doctor of Philosophy degree in June 2016 in solid state chemistry.